2012

Characterization of Damage Zones Associated with Laboratory Produced Natural Hydraulic Fractures

Erin Bradley
University of Massachusetts Amherst

CHARACTERISTICS OF DAMAGE ZONES ASSOCIATED WITH LABORATORY PRODUCED NATURAL HYDRAULIC FRACTURES

A Thesis Presented

by

ERIN ELIZABETH BRADLEY

Submitted to the Graduate School of the
University of Massachusetts Amherst in partial fulfillment
of the requirements for the degree of

MASTER OF SCIENCE

September 2012

Geosciences

CHARACTERISTICS OF DAMAGE ZONES ASSOCIATED WITH LABORATORY PRODUCED NATURAL HYDRAULIC FRACTURES

A Thesis Presented

by

ERIN ELIZABETH BRADLEY

Approved as to style and content by:

David F. Boutt, Chair

Michele L. Cooke, Member

Michael Williams, Member

Mark Leckie, Department Head
Department of Geosciences

AWKNOWLEDGMENTS

I would like to thank my advisor, David Boutt for teaching me hydrogeology and introducing me to natural hydraulic fractures. I would also like to thank Laurel Goodwin for her long-distance guidance, expertise on fracture processes and universal stage instruction. I am grateful to Michele Cooke for teaching me the basics on fracture processes and introducing me to the large world of brittle fractures. I'd like to thank my research group and office mates for their support and insight. I would also like to thank my family for their never ending love and support and Adam for always sticking by me and never letting me give up on myself.

ABSTRACT

CHARACTERISTICS OF DAMAGE ZONES ASSOCIATED WITH LABORATORY PRODUCED NATURAL HYDRAULIC FRACTURES

SEPTEMBER 2012

ERIN ELIZABETH BRADLEY, B.A., FRANKLIN & MARSHALL COLLEGE

M.S., UNIVERSITY OF MASSACHUSETTES AMHERST

Directed by: Professor David F. Boutt

Both joint sets and fault-related fractures serve as important conduits for fluid flow. In the former case, they can strongly influence both permeability and permeability anisotropy, with implications for production of water, hydrocarbons and contaminant transport. The latter can affect issues of fluid flow, such as whether a given fault seals or leaks, as well as fault mechanics. These fractures are commonly interpreted as Natural Hydraulic Fractures (NHFs), i.e., mode 1 fractures produced when pore fluid pressure exceeds the tensile strength of the rock. Various mathematical models have been a rich source of hypotheses to explain the formation and propagation of these fractures, but have provided only limited information about fracture spacing and nothing about processes of fracture initiation in originally intact rock. Recent laboratory experiments of French et al. (2012) have advanced our understanding of mechanical controls on fracture initiation and spacing. Here, detailed analysis of both through-going fracture surfaces, non-through-going fractures and microcrack distributions in experimentally deformed samples provide a deeper understanding of NHF processes and resulting geometric features in porous siliciclastic sedimentary rocks.

Fractures are studied from a homogeneous, isotropic, fine to medium-grained quartz arenite (SPss-1), a homogeneous, anisotropic, coarse-grained quartz-rich siltstone (Abo Fm.), and a heterogeneous, isotropic, medium-grained quartz arenite (SPss-2). Both homogeneous samples developed a single, through-going fracture surrounded by a halo, or damage zone, of microcracks. In contrast, the heterogeneous sample developed a single through-going and multiple (at least 6) non-through-going fractures, which appear to have nucleated on small, irregular, iron oxide concretions. Microcracks are rare in this sample, it's associated damage zone is the narrowest and microcracks surround non-through going fractures give insight on process zone development.

Observations indicate that both fracture planarity and microcrack damage (which has not previously been reported for opening mode fractures) vary significantly depending on the degree of mechanical heterogeneity and anisotropy of the host rock. Variations reflect mechanical controls on fracture initiation and propagation, suggesting that fracture spacing may in part reflect the distribution of mechanical heterogeneities. These data indicate that the more homogeneous the rock, the greater the microcrack damage surrounding a given NHF, increasing expected fracture-associated permeability for a given fracture aperture.

TABLE OF CONTENTS

LIST OF TABLES

Table Page

LIST OF FIGURES

Figure Page

CHAPTER 1

INTRODUCTION

There are two divisions of fractures within the Earth that occur under various circumstances, joints and faults. This study will focus on a specific type of joint called a Natural Hydraulic Fracture (NHF). An NHF is formed when a fluid induces joint growth. This is a natural process, unlike induced hydraulic fractures where fracture formation is a function of the rate of fluid injected through a borehole (Berchenko, 1997). NHFs are formed when fluids drawn from the host rock create an internal fluid pressure inside the fracture (Berchenko, 1997, Engelder and Lacazette, 1990). A natural hydraulic fracture will form where the pore fluid pressure exceeds the least compressive stress by an amount equal to the intrinsic tensile strength of the rock (Secor 1965, Boutt et al., 2009, French, 2010). NHFs are important because they explain how fractures form in overpressure, with increasing depth in the Earth's crust, in sedimentary basins (Secor, 1965, L'Heureux and Fowler, 2000,Boutt et al., 2009) and associated with fault zones (French et al., 2012). In these locations NHFs are important in groundwater, hydrocarbon and ore fluid migration (Secor, 1965).

The natural state of the crust is hydrostatic, an isotropic stress where the ratio of fluid pressure to overburden weight equals an effective stress that is less than the lithostatic gradient (25 MPa/km). In this state a mechanism creating overpressure is required to cause the effective stress to overcome the lithostatic gradient. Overpressure is this mechanism. Occurrences of overpressure are documented in sedimentary basins, oil reservoirs, around propagating dike tips, in accretionary prisms and in fault zones. There are two basic mechanisms that cause overpressure in these situations, either the space the

fluid occupies is restricted or more fluid is generated. Sedimentary basins, accretionary prisms and fault zones fall under the first mechanism, while dike tips and oil reservoirs fall under the second.

Within oil reservoirs and dike tips it is the production of more fluid that causes overpressures to occurs. In these geologic situations something is generating more fluid. In oil reservoirs the generation of oil from kerogen produced more fluid, and in dike tips the build up of magma produces more fluid.

In sedimentary basins overpressure builds up when high sedimentation rates restrict the escape of pore pressure fluids. As burial continues overpressure increases with depth. A similar mechanism occurs in accretionary prisms, where fluid pressure gets trapped and builds at a rate faster than the accretion. Within fault zones the restriction of fluid is caused by the seismic cycle. In locations were pore fluids are unable to communicate with the surface, a pre-seismic increase in both differential stress and pore fluid pressure at very low strain rates occurs (Sibson, 1992). As seismic rupture occurs the differential stress in the primary slip zone is suddenly reduced and has been proposed to produce tensile fractures (Dalguer et al., 2003). This build up of differential stress and pore pressure coupled with the fast drop in stress during seismic rupture, might be the best natural example of the experiments discussed in this thesis (French et al., 2012).

Conditions of NHF formation and the associated mechanics have been better understood through NHF experiments (Boutt et al., 2009, French et al., 2012). Experiments suggest that the magnitude of permeability and fluid overpressure have a significant effect on the formation and occurrence of NHFs (Boutt et al., 2009). Mechanics of NHF are dependent on strain rate, differential stress and hydrologic

properties of the rock (French et al., 2012). Even though NHF formation conditions and mechanics are known their specific fracture characteristics are still unknown. By investigating the microcracks formed by NHF it will be possible to discover if commonly interpreted extension fractures identified in sedimentary basins as NHFs (Engelder and Lacazette, 1990, Capuano, 1993, L'Heureux and Fowler, 2000) are indeed NHFs. The evolution of sedimentary basins will be better understood if the formation of their associated fractures is known.

This study focuses on NHFs produced under laboratory conditions. Boutt et al., (2009) conducted experiments and numerical modeling that combine rock extension with elevated pore fluid pressure to induce natural hydraulic fractures in rocks. French (2010) continued this experimental work at Sandia National Laboratories in New Mexico, expanding the samples to a suite of sandstones and a siltstone. Mechanical properties of samples were varied to investigate differences in NHF initiation and formation. Two sandstones were used, one homogenous – isotropic and the other heterogeneous – isotropic and one homogenous – anisotropic siltstone was also used. Concentration of this study will be on microcrack distributions and orientations associated with NHF and how they are influenced by sample characteristics.

Microfractures are the first step in joint propagation (Engelder and Lacazette, 1990). They form in rock pore spaces, along grain boundaries and at flaws. Most microfractures are extensional and their crack density increases when the stress is above the threshold level for fracture (Kranz, 1983). Therefore the extensional stress during NHF forms microfractures. Analysis of microfactures associated with NHFs produced through laboratory experiments will be done through surface analysis, optical microscopy

and image analysis. Results of these methods will provide a clear characterization of microfractures associated with NHFs. With these characteristics extensional fractures in sedimentary basins can be identified as NHFs or not.

CHAPTER 2

BACKGROUND

Fractures, including NHFs initiate at mechanical flaws (Tapponnier & Brace, 1976; Pollard & Aydin, 1988; Engelder & Lacazette, 1990). Boundaries of inclusions, microcracks and pores are mechanical flaws where elevated stresses concentrate (French et al., 2012). Tensile stresses localize here and cause through-going fractures to initiate. A crack tip develops where microcracks accumulate, forming process zones (Atkinson, 1987). As microcracks link a macroscopic fracture forms. The macrofracture then propagates leaving behind any unlinked microfractures from the process zone to become the damage zone. There are different types of microfractures and in this study those associated with the formation of a NHF under laboratory conditions are investigated.

2.1 Microfracture Characteristics

Microfractures have previously been separated into different groups (Kranz, 1983): grain boundary cracks, intragranular/intracrystalline cracks, intergranular/intercrystalline and transgranular cracks. Grain boundary cracks are those associated with grain boundaries. Intragranular cracks are smaller than the grains and are located entirely within a grain. Intergranular cracks cross grain boundaries and can enter another grain or multiple grains. Transgranular cracks are cracks that traverse a grain from grain boundary to grain boundary. They can stay within one grain or cross multiple grains. The terms microcracks and microfractures will be used synonymously and are defined as openings in rocks that have one or two dimensions smaller than the third, with one dimension much less than the other two and the width to length ratio (crack aspect

ratio) must be less than 10^{-2} and are typically 10^{-3} to 10^{-5}; microcrack lengths are on the order of 100μm or less (Simmons & Richter, 1976; Kranz, 1983).

Propagation of microcracks occurs when the local stress exceeds the characteristic tensile strength of the rock, *T,* causing brittle fracture. This can happen under a variety of natural circumstances: faulting, presence of a deviatoric stress field, hydrostatic pressure, over pressure conditions, spatial and temporal changes and compressive boundary loads. This study focuses on microfractures produced by fluid overpressure i.e. NHFs, in a tension.

2.2 Natural Hydraulic Fracture Experiments

NHFs are mode I fractures, formed when the Terzaghi effective stress, σ'_{ij} overcomes the tensile strength of the rock, T (Terzaghi, 1943; Biot, 1940; Wang, 2000). Effective stresses are given by

$$\sigma'_{ij} = \sigma_{ij} - p\delta_{ij} \qquad [2.1]$$

in which tensile stresses are negative, σ_3 is the least compressive stress ($\sigma_3 < \sigma_3 < \sigma_3$), i and j = 1, 2 and 3, δ_{ij} is the Kronecker delta function and p is pore pressure. Failure criterions is

$$\sigma'_3 = \sigma_3 - p \leq T \qquad [2.2]$$

using the convention that the principal normal stress is identified with a single subscript (e.g. $\sigma_{33} = \sigma_3$). To form NHFs French (2010) refined experiments by Boutt et al. (2009) to satisfy equation 2.2. In core samples, French (2010) achieved this by producing a fluid pressure gradient parallel to the core axis while maintaining a pore fluid pressure greater

than axial stress. Notation for the experimental protocol is that *a* is the direction parallel to the core axis, *r* is the radial direction and imposed stresses are σ_a and σ_r.

Initial conditions were set with $\sigma_r > \sigma_a$ (Figure 2.1-A). First, confining pressure was increased to σ_r while axial load was simultaneously increased to σ_a, so $\sigma_r = \sigma_a +$ 2MPa (Figure 2.1-B). Then a spatially uniform pore pressure was raised to p, now $\sigma_r > \sigma_a > p$. Next, p was reduced by manually opening the top and bottom fluid ports to the atmosphere and then σ_a was reduced to 2 MPa as p simultaneously reduced to 0 MPa. This causes $p > \sigma_a$ everywhere except at the end caps. A pore fluid pressure gradient Δp and an effective stress σ'_3 parallel to the core axis is produced (Figure 2.1-C). Tensile failure criterion [2.2] was met, producing one primary through going NHF in each sample (Figure 2.2), with several observable non-through going fractures in one sample (Figure 2.2-B).

French et al. (2012) determined that the fractures formed by this protocol are NHFs. When cores only experienced confining pressure (drained conditions) they did not fail, suggesting that confining pressure alone was not enough for fracture formation. Fluid pressure (undrained conditions) were needed to cause failure. During undrained tests, through going fractures (NHFs) were not produced when each sample experienced the greatest pore pressure (French et al., 2012). They are presumed to have formed after the effective stresses were no longer tensile, at 2-250 seconds after maximum pore pressure, experiencing axial strains between 2×10^{-3} and 2×10^{-2} (French et al., 2012). Propagation occurred at negligible pore pressure after significant sample dilation occurred in each sample. Figure 2.3 shows the axial stress vs. axial elongation of NHF experiments. Unloading paths in Figure 2.3 show initial axial shortening as a result of

pore fluid draining from the system when the fluid ports were opened, followed by axial extension as the axial load is reduced (French et al., 2012). The amount of time it took from the reduction of the axial stress to NHF formation is indicated, documenting differences in elongation. Dilation, a mechanism of elongation, occurred in all samples and has been hypothesized to open pores and microfractures (French, 2010) leading to the formation of NHFs. Samples also experienced minor permanent volume change, suggesting that core experienced inelastic deformation.

French's (2010) experiments demonstrated that sample-scale mechanical heterogeneity and anisotropy affect the location of fracture initiation but are not required for fractures to nucleate and grow. Without mechanical heterogeneity and anisotropy, a fracture will form where pore pressure, stress and strain reach a maximum (French, 2010).

CHAPTER 3

SAMPLE CHARACTERISTICS

Three experimentally produced NHFs were macrostructurally and microstructurally investigated. Two were sampled from the mid-Ordovician St. Peter Sandstone, and one from Permian Abo Formation siltstone. St. Peter Sandstone was chosen for investigation because of its realatively simple composition and Abo siltstone was chosen to investigate anisotropic bedding influences on NHF initiation.

St. Peter Sandstone is a laterally continuous quartz arenite. It was buried less than 1000m (Cook, 2011) and extends over ~ 600,000 km^2 of the midwestern USA (Dott, 1985). The samples were collected in Wisconsin. Here, the St. Peter Sandstone ranges from absent to 400ft thick (Dott, 1985). Grain composition has been reported at ~ 97% quartz for this moderately well sorted mature sandstone (Pitman et al., 1997; Kelly et al. 2007). Samples used in this study have a detrital framework of 100% quartz with decreasing abundances of authigenic quartz overgrowths, minor authigenic potassium feldspar, and iron oxide cements (French et al., 2012).

The most homogeneous and isotropic St. Peter Sandstone sample is referred to as SPss-1 (Figure 2.2-A). It has a relatively uniform cement distribution, low oxide cement, no potassium feldspar overgrowths and an average grain diameter of 0.195mm (Table 3.1) (French, 2010). The heterogeneous isotropic St. Peter Sandstone will be referred to as SPss-2. It has cm-scale ellipsoidal to irregularly shaped concretions where pores are filled with iron oxide (Figure 2.2-B). Concretions have lower porosity and less quartz cement than the rest of the rock. Concretion boundaries are diffuse with porosity generally increasing away from the center of the concretion (French, 2010). Average

grain diameter for the SPss-2 matrix is 0.192mm and 0.16mm for concretions (Table 3.1). Back-scattered electron (BSE) and cathode luminescence (CL) images were previously used to characterize these samples at the grain and pore scale (French, 2010). Some anisotropy, defined by a shape preferred orientation of grains plus overgrowths, was found (French, 2010). Sample SPss-1 showed the least shape preferred orientation, and concretions in SPss-2 have the strongest shape preferred orientation with their long axes parallel to bedding (French, 2010). Sample SPss-1 was chosen for testing because it is the most homogenous end member of the St. Peter Sandstone; SPss-2 was chosen to investigate the influence of distributed heterogeneity (iron oxide concretions) without anisotropy.

The Abo formation is a homogeneous anisotropic siltstone from New Mexico (Figure 2.2-C). Previous experiments by Bout et al. (2009) and a study by Bensing et al. (2005) describe mechanical and hydrological characteristics of the Abo Fm. This sample is a homogeneous anisotropic coarse-grained siltstone to fine-grained sandstone deposited in a fluvial environment. It is quartz-rich with low permeability and mm-scale bedding defined by small variations in iron oxide abundance and grain size (French, 2010). Bensing et al. (2005) described the clay present as detrital. French (2010) identified the clay mineralogy with an x-ray diffractometer, finding that clays present are mainly kaolinte with some smectite, while cements are a combination of quartz overgrowth and carbonates (French, 2010). French (2010) also did back scatter electron and cathodoluminesence imaging showing that there is a local grain-shape preferred orientation with a spatially variable relationship to bedding ranging from subparallel to about 30°. During NHF experiments (French, 2010), the Abo sample was tested with

bedding both perpendicular and parallel to the core axis. Bedding parallel samples did not fail; therefore the tested Abo sample with bedding perpendicular to the core axis will be examined in this study.

The Average grain diameter for the Abo sample, has not previously been reported, and was determined using Johnson's (1994) method, which finds the mean true nominal diameter of ellipsoidal grains by applying a correction factor to the mean long axis lengths measured from thin sections. A correction is needed because random grain diameters measured in thin sections underestimate true grain diameters (Burger & Skala, 1976; Johnson, 1994). Mean long axis lengths were measured on a 1 by 1mm grid resulting in a point count of 285 quartz grains with a mean long axis length of 0.056 mm. Johnson's (1994) correction factor was applied by multiplying the mean long axis length by 1.1318 to get a true grain diameter of 0.064 mm for Abo.

CHAPTER 4

MICROFRACTURE CHARACTERIZATION METHODS

4.1 Surface Analysis

Fracture surfaces of the NHFs produced through previous experiments (French, 2010) were scanned with a 3D Next Engine scanner, located in the Rock Mechanics lab at the University of Massachusetts, with a spatial resolution of 63μm and a vertical accuracy of 12.7μm (NextEngine Inc.). Scans produced XYZ elevation data, which were visualized with the program 3DMove (Midland Valley Exploration Ltd.) to produce topographic images and obtain surface elevation profiles. Data were also processed through MATLAB to obtain elevation statistics.

4.2 Thin Section Creation and Orientations

Following surface characterization, cores are cut into thin sections for microstructural characterization. First each core had to be remediated to extract any pore fluid left from experiments. Remediation was done at the University of Wisconsin Madison under the instruction of Professor Laurel Goodwin. After remediation thin sections were cut both perpendicular and parallel to each through-going NHF. Sections cut perpendicular to the NHF were determined based on significant surface patterns and were located in different locations for each rock. Sections cut parallel to the NHF were then cut from the same pieces as perpendicular sections, creating mutually perpendicular sets. Because NHFs are not planar, sections that are intended to represent the fracture plane can be difficult to obtain. Areas with the least amount of surface elevation change

were used for this purpose. There isn't a mechanism to ensure that all cuts are parallel, which means sections may vary in orientations by a few degrees from one another.

Geographic north is not known for these samples so 0° (N) is chosen based on surface patterns (Abo & SPss-2) or arbitrarily (SPss-1). Abo has the only NHF with a consistent surface pattern. Mutually perpendicular thin sections were cut parallel and perpendicular to this surface pattern. Figure 4.1 shows the orientation, location and name designation of thin sections for Abo. A total of ten sections were cut and used from the Abo Formation: eight perpendicular thin sections and two parallel thin sections.

Like the Abo sample, St. Peter Sandstone SPss-2 had a surface pattern in the form of a ridge. Thin sections, mutually perpendicular, were cut parallel and perpendicular to the ridge (Figure 4.2). As the only rock that formed non-through-going NHFs along with the primary NHF, thin sections for SPss-2 were cut to obtain non-through-going fractures and their tips (Figure 4.3). Eight thin sections were cut and used for SPss-2: four perpendicular thin sections, two parallel thin sections and two non-through going thin sections that are perpendicular to the NHF.

Because there isn't anything distinctive about SPss-1 surface, mutually perpendicular thin sections and parallel sections were cut arbitrarily (Figure 4.4). A total of twelve thin sections were cut and used from SPss-1: eight perpendicular thin sections and four parallel thin sections. All thin sections were used for all optical microscope and image analysis.

4.3 Optical Microscopy

An optical microscope was used in two capacities for microfracture characterization. First, a petrographic microscope (Nikon) was used to find the linear crack density and distribution of microfractures in both undeformed and post experimental thin sections. Second, a petrographic microscope equipped with a universal stage **(**Carl Zeiss) was used to find orientations of microfractures, and aid in determining the extent of non-through going fractures.

4.3.1 Linear Crack Density

Microfracture density was determined by following the procedure of Wilson et al., (2003). The number of microfracture traces that intersect a line the length of 1.5 times the average grain diameter of each sample was recorded. The number of microfracture intersections were summed and divided by the length of the counting line to calculate a linear crack density of microfractures with units of fractures/mm (Anders & Wiltschko, 1994). These values quantify the measure of damage that the rock experienced at a given place. Figure 4.5 shows a schematic of how linear crack density was calculated.

By using a thin section from an undeformed sample, it was determined that a transect of 20 grains is long enough to calculate linear crack density (Figure 4.6). To determine linear crack density five transects of 20 grains were averaged, representing a transect through 100 grains. This method was used in both undeformed samples, finding a background value (include pre-existing microfractures but mostly consisting of fluid inclusion planes), and post-experimental samples, determining the extent of damage. Damage extent is found by measuring linear crack density parallel to the NHF at a given

distance and is assumed to extend away from the NHF until the linear crack density returned to the background level, defining each NHF's damage zone.

4.3.2 Microfracture Orientations

Microfracture orientations were collected with a universal stage from three mutually perpendicular thin sections and analyzed using Richard Allmendingers program Stereonet v. 6.3.3.X (Personal Communication). For perpendicular thin sections, distances for orientation collection correspond to distances where linear crack density was collected, allowing the entire damage zone to be represented and investigating change in orientation with distance from the NHF. In parallel sections orientations were collected as close to the core axis as possible and as far away from the core axis as possible. This is to investigate if orientations changed throughout the plane of the NHF. Care was taken to measure orientations away from the edge of the thin section where coring and sawing may have induced damage. An operator bias of measuring microfractures within 0-20° of the view plan arises when using a universal stage (Borg et al., 1960). Microfractures that are oriented less than 20° from the vertical are more easily measured. Reducing this bias was accomplished by making maximum angular sweeps in order to view cracks with high angles to the viewing direction (Anders & Wiltschko, 1994; Vermilye & Scholz, 1998; Wilson et al., 2003).

Microfracture orientations consist of strikes and dips. Each thin section has an arrow indicating the up core direction; collection of orientations was done with the arrow aligned with North on the universal stage. This ensures that all orientations can be compared to one another. Because thin sections have different orientations within the

core, all data were rotated so each steronet is looking down the plunge of the core. With a universal stage, an orientation is found by identifying an open microfracture, rotating it so it's striking horizontal across the view plane and finding the dip using the second axis of rotation. Before corrections are applied the strike is recorded where the rotating stage lines up with zero and dip is recorded where the second axis of rotation is at zero. Microfracture traces are not always striking straight across the view plane. If undulating, a microfracture trace is considered a single crack if it's orientation does not change by more than 20° (Hadley, 1976, Janssen et al., 2001). If there was a change of more than 20° along a microfracture trace than two orientations were collected. Appendex B summarizes corrections applied to orientations collected from the Universal stage.

When determining how many measurements to collect per distance from the NHF considerations were made, because significant populations of microfractures vary as a function of rock type and the relative contribution of pre-existing microfractures (Anders & Wiltschko, 1994). First, reproducibility was considered. The number of open microfractures decreases moving away from the NHF and sample size has to be the same at each distance from the NHF; the amount of open orientations collected per distance away from the NHF had to be selected so that orientations could be compared throughout the rock and between all samples. Second, comparibility between 50 orientations and 100 orientations per thin section were investigated. For mutually perpendicular thin sections, 100 open orientations were measured at the same depth. Orientations are then randomly ordered using a random number generator and plotted on separate equal area nets with 50, 60, 70, 80, 90 and 100 orientations. Contours constructed using the Kamb method, showing the departure from a random distribution. All equal area plots used for analysis

use the Kamb contour with a confidence interval of 3.0. Figures 4.7, 4.8 and 4.9 show comparison plots for SPss-1. The main difference between plotting 50 poles and plotting 100 poles is the concentration of orientations. The distribution of those poles remains the same. Figure 4.10 shows equal area nets of all three mutually perpendicular thin sections plotted together at 50 and 100 orientations per thin section. These show the same conclusion as the separated plots. With more poles plotted, concentration increases but the same general distribution remains. In the parallel thin sections, the concentration is even more similar between 50 plotted poles and 100 plotted poles than it is in perpendicular thin sections.

Sets of 50 open microfractures per thin section were determined to be statistically significant, resulting in total sets of 100 or 150 open microfractures for specific distances away from the NHF. This number is based on reproducibility with distance from the NHF and because overall the number of microfractures measured will be sizeable enough to overcome operator bias. Healed microfracture orientations were not included in this count of 50 and are measured when they shared a grain with any collected open microfractures.

4.3.2.1 Weighting of Orientations/Measurable Areas

In order to analyze orientations, it is imperative to understand how collection of orientations influences equal area net plots. When all three sets of mutually perpendicular orientations are rotated to be in the same plane (see Appendix A), there are zones where orientations may be preferentially measured because thin sections are perpendicular to each other. However, there are no locations where orientations are not measured providing maximum coverage of each sample (Engelder, 1974; Friedman,

1995). All areas on the equal area net are sampled at least twice with a zone of triple measured area (Figure 4.11). For the most part the zone of triple sampling lies where the largest dip inclination possible is for each thin section. Even though these areas are triple sampled, they may be under sampled due to operator bias when measuring microfractures at higher angles to the viewing plane. A weighting scheme was investigated using dip inclinations from raw Universal-Stage measurements and a comparison of pole counting in zones. Appendix B summarizes this investigation. Based on the results of the weighting investigation, it was determined that a weighting scheme could not be developed with confidence. This leads to a limitation of equal area nets in this study. Most of the equal area plots presented will only have orientations collected from two mutually perpendicular thin sections. With only two thin sections all areas on the equal area net are sampled (Figure 4.12), but when viewing these microfractures that are perpendicular to the NHF will not be represented, as those are the ones collected in parallel thin sections. These limitations must be kept in mind when viewing equal area net plots.

4.4 Image Analysis

4.4.1 Mapping/Tracing Non-Through Going Fractures

Photomicrographs and a microscope outfitted with a universal stage were used to map/trace non-through-going fractures found only in SPss-2. Fist, multiple images were taken with a Olympus Q-Color-5, under crossed polars, to capture the entire extent of each non-through going fracture. Images were then stitched together in Adobe Illustrator to form a single image of each fracture. These images were printed out and with the aid

of a Universal stage each non-through going fracture and associated microfractures were traced by hand then digitized in Illustrator. Aperture, the distance between an open fracture's walls, and connectivity, when fractures intersect one another, were used to distinguish between segments making up the non-through going fracture and adjacent microfractures.

Images were also taken to perform shape preferred orientation analysis on the grain structure in SPss-2 and the Abo formation. The methods and results are discussed in Appendix C.

CHAPTER 5

NHF CHARACTERIZATION RESULTS

5.1 Surface Analysis

The first step in characterizing NHFs is investigating their surfaces. Before thin sections were cut elevation statistics were collected from both sides of each NHF (Table 5.1). NHF elevation is on the mm scale and provides a measure of planarity, fracture roughness, for each fracture surface. Data is dealt with in three ways. First, observing highest elevations and mean elevations between samples. Second, plotting elevation histograms to investigate distribution trends, and lastly, visualizing elevation distribution with 3D surface maps.

The Abo Fm has the highest elevation of all NHFs with top and bottom surfaces reaching 0.61cm and 0.55cm and mean elevations of 0.35cm and 0.23cm respectively. The St. Peter sandstone samples have half or less than half of the Abo Fm's maximum and mean elevations. SPss-1 is has the smallest maximum elevation with top and bottom surfaces reaching 0.26cm and 0.23cm and mean elevations of 0.14cm and 0.13cm respectively. Elevations are less than 0.1cm higher in SPss-2 than SPss-1 with top and bottom total elevations of 0.32cm and 0.31 and mean elevations of 0.14cm and 0.19cm respectively. Even though SPss-1 has lower maximum elevation than SPss-2, both St. Peter sandstones have similar mean elevations.

To better understand elevation statistics, histograms show distribution in elevation for top and bottom surfaces. The Abo Fm's top surface shows highest frequencies ranging from around 0.4cm to 0.5cm (Figure 5.1-A), while the bottom surface shows highest frequencies ranging on the lower end around 0.08cm to 0.2cm (Figure 5.1-B).

Both the Abo Fm surfaces show skewed distributions suggesting an asymmetric surface pattern. SPss-2 elevation histograms also have a skewed distribution; with highest elevation frequencies ranging from 0.1cm to 0.15cm and 0.23cm to 0.28cm for top and bottom surfaces respectively (Figure 5.1-C&D). A sharper skewed distribution is seen in SPss-2 than in the Abo Fm. Unlike the Abo Fm and Spss-2, elevation frequencies for SPss-1 follow a normal distribution, implying that the fracture surface is planar when compared to those of the Abo Fm and Spss-2. SPss-1's elevation frequencies are highest around the mean elevations for each surface. The top surface, with a mean elevation of 0.14cm, has highest elevation frequencies ranging from 0.13cm to 0.15cm (Figure 5.1-E), and the bottom surface, with a mean elevation of 0.132cm, has highest elevation frequencies ranging from 0.13cm to 0.155cm (Figure 5.1-F).

Elevation distribution was also visualized with 3D maps of each surface (Figure 5.2). Each map shows highest elevation in red for that specific surface and lowest elevation in blue. Green shows average elevations. High elevations on one surface of a NHF correspond to low elevations on the other surface. More deviation from average elevation is found in the Abo Fm and the least deviation, where the map is mostly green is seen in SPss-1. Fracture surfaces, like elevation statistics, are most similar between the two St. Peter Sandstones. Both SPss-1 and SPss-2 have average elevations surrounding a high or low area in the center of the NHF, with SPss-2 having a broader high or low center (Figure 5.2-C, D, E&F). The Abo Fm's NHF surface is the most different showing abrupt changes in elevation across its surface (Figure 5.2-A&B). Abrupt elevation changes stand out as shaded or highlighted bands depending on which surface is being observed. One other abrupt elevation change is seen in SPss-2 bottom surface (Figure

5.2-D). A highlighted band transitioning up to average surface elevations borders lowest elevations on SPss-2 bottom. The top surface of SPss-2 does not show an abrupt change in elevation at the corresponding high, this may be due to material loss. There are no abrupt elevation changes on either SPss-1 surfaces showing gradual change in elevation across the NHF (Figure 5.2-E&F).

Surface data show, that the most homogeneous isotropic sample (Spss-1) has the lowest elevation, a normal distribution and a surface free of abrupt elevation changes. While the samples exhibiting heterogeneity and anisotropy have higher elevations, skewed distributions and abrupt changes across their surfaces.

5.2 Optical Analysis

5.2.1 Microfracture Descriptions

Fluid inclusion planes are present in all three rocks (Figure 5.3). Fluid inclusion planes form when former open microfractures heal forming fossilized fluid pathways (Lespinasse, 1999; Faulkner et al., 2006) and can be remnants of primary inclusions from the host rock. These are mode I cracks (Lespinasse, 1999); they do not show evidence of shear displacement and thus, don't disrupt the mechanical continuity of the mineral grains (Lespinasse, 1999). Therefore, under stress, a grain with fluid inclusions planes will act similarly as a grain without fluid inclusion planes. Multiple generations of fluid inclusions planes can be present, frequently cross cutting each other and each having distinct orientations.

5.2.1.1 Homogeneous – Isotropic Sandstone (SPss-1)

Open microfractures, formed during NHF experiments, in SPss-1 can be seen in Figure 5.4. Larger microfractures are sub-parallel or shallowly dipping with respect to the NHF; smaller microfractures are typically perpendicular to larger ones, and there can commonly be sets of two or more parallel microfractures. These open microfractures are not straight planer traces. In 2D, most have some curvature to them. Most microfractures are intragranular (confined within a grain) and almost always contact a grain boundary, commonly where two grains contact one another. There are some grain boundary cracks and transgranular (multiple grain boundaries), while intergranular (crossing grain boundaries) cracks are seldom observed. Cross cutting of fluid inclusion planes is common. Occasionally it can be determined that an open microfracture formed along a healed microfracture. Areas with high amounts of microfractures present are around pore spaces (Figure 5.5).

5.2.1.2 Heterogeneous – Isotropic Sandstone (SPss-2)

Microfractures within SPss-2 are all opening mode. All four types of microfractures developed in this sample: grain boundary, intragranular, intergranular and transgranular (Figure 5.6). Visible aperture, measurable space between fracture walls, is noted in transgranular and intergranular cracks that are close to the NHF surface or to a non-through-going fracture. Microfractures cross cut fluid inclusion planes and can intersect one another. As with microfactures in SPss-1, those in SPss-2 are not always straight planar features; most have curvature.

Unlike the homogeneous St. Peter Sandstone (SPss-1), the heterogeneous sample (SPss-2) has more than one NHF. There are 6 non-through-going fractures that were seen on the cores exterior after the experiment (Figure 2.2). Three non-through-going fractures were captured in thin sections (Figure 4.3), two which span the width or length of the thin section and one that terminates within the thin section plane. All non-through-going fractures have visible aperture (measurable space between fracture walls) and can be viewed with the eye in hand sample and thin section. Figure 5.7 shows a non-through-going fracture in both plain and polarized light. These mesoscopic fractures are made up of transgranular, intergranular and grain boundary segments. Fracture segments are distinguished from microfractures by: 1) visible aperture, where both fracture walls can be seen, not just a discrete line and 2) connectivity, linkage of multiple microfractures to one another.

Non-through-going fractures have different characteristics from each other. Some have more microfractures surrounding the non-through-going fracture and more microfractures continuously connected than others. Figure 5.8 shows a fracture that terminates within the thin section plane. There aren't many microfractures surrounding this mesoscopic fracture and fracture segments aren't continuously connected. Figure 5.9 shows non-through-going fracture spanning a thin section. This non-through-going fracture is made up of disconnected fracture segments, exhibiting an en echelon nature with variable microfracture development surrounding the fracture. Figure 5.10 shows another fracture spanning a thin section, this one is continuous. Connected fracture segments show local fracture-bound lenses and well developed microfractures surrounding the mesoscopic fracture. A histogram for each non-through-going fracture,

shows microfractures binned per 1mm and separated into microfractures and fracture segments.

5.2.1.3 Homogeneous – Anisotropic Siltstone (Abo Fm.)

The majority of open microfractures formed in Abo are found in Quartz grains. Just like both St. Peter Sandstone samples, not all grains have microfractures, even those adjacent to the NHF. Intergranular microfractures are the most common but there are some grain boundary cracks, a few transgranular and very few intragranular cracks. Larger microfractures adjacent to the NHF surface dip sub-parallel and shallowly with respect to the NHF surface. Abo's NHF surface is more variable than the St. Peter Sandstones. Its microfractures vary with respect to the fracture surface. Microfractures formed in Abo are not perfectly straight; they most always have some curvature to them. Sets of two or more parallel microfractures within one grain are common. Intersecting the NHF is a crossbed (Figure 5.11).

5.2.2 Linear Crack Density

Background linear crack density was determined from protolith samples. Figure 5.12 shows background densities vs. average grain size, and Table 5.2 shows background linear crack density with other grain characteristics. There are two background linear crack density values for SPss-2, one was found inside the iron oxide concretions and the other was found outside concretions. Smallest linear crack densities were found in the St. Peter samples, which have larger grain sizes than Abo. The most homogenous sample, SPss-1 had the smallest values at 5.4 frac/mm. Both background linear crack densities for SPss-2 were also small with fewer fractures per millimeter outside the concretions at 5.9

frac/mm and more fractures per millimeter inside the concretions at 7.3 frac/mm. Highest background linear crack density values, 20.5 frac/mm, were found in Abo, the sample with the smallest grain size. These background linear crack densities are plotted along with linear crack density analyses of post experiment thin sections showing when microfractures return to pre-experiment values.

5.2.2.1 Homogeneous – Isotropic Sandstone (SPss-1)

The highest linear crack density values for SPss-1 are found at the NHF surface, above the NHF is 19.21 frac/mm and below the NHF is 14.07 frac/mm (Figure 5.13). Lowest linear crack density values are found about 2 - 2.5cm away from the NHF. Above the NHF, linear crack density values enter the background region at 2 cm with an average of 5.68 frac/mm. Below the NHF, the range of linear crack density at 2cm is in the background region but average linear crack density does not enter the background region until 2.5 cm at an average of 5.82 frac/mm. Decreases in linear crack density are exponential when moving away from either side of the fracture (Figure 5.14). Linear crack densities at each distance away from the NHF, above the NHF fall within the error bars of linear crack densities below the NHF and vice versa. Therefore, based on linear crack density, SPss-1 has a symmetrical microcrack damage zone that extends almost 2 cm to either side of the NHF.

5.2.2.2 Heterogeneous – Isotropic Sandstone (SPss-2)

Unlike linear crack densities in SPss-1, linear crack densities in SPss-2 do not display the same symmetry (Figure 5.15). Linear crack densities are not highest at the NHF surface in this sample. About 2-2.5mm above the NHF linear crack density values are the highest at 12.29 frac/mm. Along the surface, were the next highest values at 9.34

frac/mm and 10.59 frac/mm for the top and bottom respectively. The damage zone extends only 5mm on either side of SPss-2's NHF. Above the NHF, linear crack density enters the background region with an average of 6.15 frac/mm 5mm from the NHF. Below the NHF, linear crack density enters background level with a range of 5.55 frac/mm to 7.63 frac/mm at 5mm. Figure 5.16 shows an exponential fit to linear crack density both above and below the NHF.

Linear crack density values were obtained from non-through going fractures located in SPss-2 but only along either side of the fracture, as damage dissipates between 1-2 mm from the fracture. The shortest non-through going fracture was not long enough to take 5 transects and only one value was possible to obtain. Above the shortest non-through going fracture (Figure 5.8) linear crack density is 9.55 frac/mm and below the fracture it's 9.2 frac/mm. There are less microfractures present as the fracture becomes more segmented. Microfractures diminish in abundance toward possible fracture termination as seen in the en echelon non-through going fracture (Figure 5.9). Above the en echelon fracture linear crack density, is 8.82 frac/mm and below its 8.92 frac/mm. These values are similar to the connected non-through going fracture whose linear crack density above the fracture is 8.51 frac/mm and 8.54 frac/mm.

5.2.2.3 Homogeneous – Anisotropic Siltstone (Abo Fm.)

Figure 5.17 shows linear crack density values for the Abo Fm. The highest linear crack density values are found at the NHF surface. Above and below the NHF, linear crack density values are 27.78 frac/mm and 29.87 frac/mm respectively. Linear crack density values enter the background regions at 1cm above with an average of 21.41 frac/mm, and below the NHF at 1cm a range of 19.84 – 23.5 frac/mm enters the

background regon. Only at 1.5cm below does linear crack density is a return to all background values at 18.28 frac/mm. The Abo Fm's damage zone is asymmetric extending farther above the NHF (1.5cm) then it does below the NHF (1cm). Figure 5.18 shows exponential fits to the asymmetric linear crack density values. Because the Abo Fm had the only consistent surface pattern, linear crack density values were found both parallel and perpendicular to this pattern and compared (Figure 5.19). Linear crack density values for mutually perpendicular thin sections at the same depths are consistently similar. Ranges for each depth are always overlapping as are standard deviations expect at 1.5 cm from the NHF. Decrease in linear crack density is more exponential for Abo C1 and more linear for Abo F1; highest values are 27.78 frac/mm and 19.35 frac/mm respectively; lowest values are 20.78 frac/mm and 18.9 frac/mm respectively.

5.2.3 Microfracture Orientations

5.2.3.1 Homogeneous – Isotropic Sandstone (SPss-1)

Microfracture orientations were measured at each distance away from the NHF that linear crack densities were measured. Orientations collected on mutually perpendicular thin sections for SPss-1 are shown in Figure 5.20. Poles to microfractures are plotted and contoured with Kamb contour at a confidence interval of 3.0. Steronets show that microfractures are shallowly dipping throughout the core and maintain a bull's-eye distribution, decreasing in abundance away from the core. The center contour, the area where orientations are the most concentrated, maintains a diameter of 30-35 degrees throughout the core. At all depths excluding +1-1.5 mm, -15mm and at the NHF below

the NHF, there is a cluster of microfractures dipping north. Another prominent feature is a band striking east-west, present at distances of 5, 10, 15 and slightly at 20 mm above the NHF surface as well as 10 and 15 mm below the NHF. Above the NHF, about 30% of microfractures fall outside the kamb contour along the NHF, 1-1.5 mm, 5 mm and 10 mm. Orientations that fall outside the kamb contour do not belong to a defined set. At distances farther away, 10 and 20 mm, microfractures outside the kamb contour decrease to 18 and 13 % respectively. Below the NHF, about 20% of microfractures fall outside the kamb contour at 5, 10 and 20 mm. Along the NHF, only 8.9% fall outside the contour. When all open microfracture orientations are plotted together, 34.2 % fall outside the kamb contour above the NHF and 40.9% below the NHF.

Figure 5.21 shows accompanying rose diagrams to each equal area steronet in Figure 5.20. Above the NHF, the majority of microfractures strike west (Figure 5.21-G). Moving away from the NHF, microfractures move from a cluster striking southwest to a more concentrated group striking west. Below the NHF, the highest percentage of microfracture also strike west but there are two large clusters striking east and north observed above the NHF (Figure 5.21-M).

Orientations for parallel thin sections from SPss-1 are shown in Figure 5.22, with accompanying rose diagrams in Figure 5.23. Microfractures in parallel thin sections are sub-perpendicular to the NHF varying about 10-20° from vertical. Along the NHF, above the fracture, away from the core axis microfractures strike north – south (Figure 5.23-E), and close to the core axis they strike northeast – southwest (Figure 5.23-F). Along the NHF, below the fracture, they do the opposite: away from the core strikes northeast – southwest, while close to the core strikes north – south (Figure 5.23-I & J respectively).

Plotted together, microfractures that are as close to the NHF as possible strike north – south both above and below the NHF (Figure 5.23-G & K respectively). Further away from the NHF, 8mm above and 6mm below show the opposite trend from each other. Microfractures above the NHF strike northwest – southeast (Figure 5.23-A, B & C), those below strike northeast – southwest (Figure 5.23-M, N & O). There is not as much variation in orientation farther away from the fracture surface.

5.2.3.2 Heterogeneous – Isotropic Sandstone (SPss-2)

Microfracture orientations associated with NHF propagation in SPss-2 are shown in Figure 5.24. Orientations collected around non-through going fractures in this sample are discussed below and located in (Figures 5.8, 5.9 and 5.10). Orientations above the NHF have a tight bulls eye pattern at the fracture surface and 2mm from the fracture surface. At 5mm away from the NHF there is a girdle striking east – west with a cluster dipping north. Close to the NHF 13-15% of microfractures fall outside the kamb contour and farther away (5mm) 26% fall outside. All open microfractures above plotted together form a bulls eye distribution with 21% of microfractures falling outside the contour. (Figure 5.24-D). Microfractures below the NHF are not as clustered as those above. A bulls eye distribution is present at each depth but each depth has a cluster of microfractures that shifts the center away from shallowly dipping. Along the NHF a cluster is in the southwest, 2 mm below the NHF the cluster is in the north and 5 mm below it's in the north and the west. When all depths below the NHF are plotted together the distribution suggests shallowly dipping microfractures with a large cluster in the southwest and another in the north (Figure 5.24-I). Percentages of microfractures outside

the kamb contour remain the same below the NHF: 14-16% close to the NHF, 22% 5mm away and 21% when all microfractures are plotted together.

Rose diagrams corresponding to each equal area steronet in Figure 5.24 are in Figure 5.25. Microfracture strikes are variable throughout the core but when plotted together the majority of microfractures strike east both above and below the NHF (Figure 5.25-D&I). Above the NHF there is a strong group of microfractures striking north south (Figure 5.25D).

Non-through-going fracture orientations were only collected from one thin section orientation (N-S). Therefore, these plots do not represent a three dimensional view of microfractures associated with a non-through going fracture. Nevertheless, information can be obtained from them. Figure 5.8-B, Figure 5.9-B through D and Figure 5.10 B through D shows equal area steronets for each non-through going fracture examined. The highest concentration of microfractures is parallel to the average orientation of the non-though-going fractures (great circle on plot) for each location. Average orientations were determined from fracture segment plots and plotted on each steronet associated with a non-through going fracture. These indicate that all three non-through going fractures dip shallowly with respect to the main NHF (15°, 17° and 11°) and strike east west.

5.2.3.3 Homogeneous – Anisotropic Siltstone (Abo FM.)

Abo microfracture orientations and rose diagrams for thin sections perpendicular to the NHF are shown in Figure 5.26 and Figure 5.27 respectively. Above the NHF a prominent bull's-eye distribution centered on the core axis is seen at each distance from the NHF. The center contour of each distances ranges from 15-25 degrees in diameter. Microfractures dip shallowly with respect to the NHF. Above the NHF, about 24% of

microfractures fall outside the kamb contour at the NHF, 5mm and 15 mm from the NHF. At 10 mm from the NHF 34% fall outside the kamb contour. With all open microfractures from each distance plotted together 25.8% fall outside the kamb contour. Figure 5.26-E shows all open microfractures (above) contoured in tight bullseye on the core axis. The center contour is 20 degrees wide and 35 degrees tall. Healed microfractures, Figure 5.26-F, contour in a loose bullseye around the core axis with a center contour about 35 degrees in diameter. Below the NHF microfractures don't cluster in as prominent a bull's-eye distribution as above and percentages of microfractures located outside the kamb contour are much lower. Moving away from the fracture surface, 14%, 11%, 19% and 7.9% of microfractures fall outside the kamb contour with 14% outside the contour when they are all plotted together.

Rose diagrams for Abo show that orientations striking northeast – southwest above the NHF and more north – south below the NHF, except on the fracture surface where fractures strike east – west. Above the NHF microfractures are more randomly oriented (Figure 5.27-E) than below (Figure 5.27-K).

CHAPTER 6

DISCUSSION

The Discussion is separated into three parts. First, will be a discussion of pertinent background material. Second, documented microfracture characteristics from the NHFs in this study will be compared with background material. Finally, a hypothesis for NHF fracture failure will be proposed

6.1 Background

Microfractures produced in known natural hydraulic conditions have never been characterized before, but microfractures produced by natural faults (Friedman, 1969; Brook & Engelder, 1977; Anders & Wiltschko, 1994; McGrath & Davison, 1995; Vermilye & Scholz, 1998; Wilson et al., 2003; Faulkner et al., 2006), shear fractures (small scale faults) (Takemura & Oda, 2004), faults and shear fractures under laboratory conditions (Menendez et al., 1995; Moore & Lockner, 1995; Janssen et al., 2001; Hoxha et al., 2004; Katz & Reeches, 2004; Takemura & Oda, 2004; Ganne & Vervoort, 2007) and fractures associated with dike tips (Delaney et al., 1986; Basson & Viola, 2004; Motokoi & Sichel, 2008) have been characterized. Studies characterize damage zones and process zones. What follows will be a discussion of their findings focusing on microfracture characteristics.

6.1.1 Damage Zones

6.1.1.1 Natural Fault Damage Zones

Each study (Friedman, 1969; Brook & Engelder, 1977; Anders & Wiltschko, 1994; McGrath & Davison, 1995; Vermilye & Scholz, 1998; Wilson et al., 2003; Takemura & Oda, 2004; Faulkner et al., 2006) characterizing microfractures produced by faults (normal, thrust and strike-slip) include tensile and shear fractures. Many studies investigating natural microfractures, characterize only healed dilatational microfractures or fluid inclusion planes (Anders & Wiltschko, 1994; Vermilye & Scholz, 1998; Faulkner et al., 2006), while others focus on open microfractures and consider healed microfractures (Wilson et al., 2003). Characterization includes microfracture appearance, microfracture density, damage zone shapes and microfracture orientation.

Anders & Wiltschko (1994) observed straight microfractures that cross multiple grain boundaries and curvilinear microfractures confined to single grains associated with faults in Southwestern United States. Curvilinear fractures were thought to emanate from, or radiate, to locations where individual grains contact each other. Vermilye & Scholz (1998) also described intragranular cracks, which are confined to single grains, associated with multiple faults in the Shawangunk Mountains. They also observed intragranular cracks parallel to adjoining grain contacts. The majority of microfractures observed in their fault study were transgranular. Similarly, within 5m of the ultracataclasite zone of the Punch Bowl fault in California, Wilson et al. (2003) found that transgranular fractures were most common, yet throughout the entire damage zone intragranular and grain boundary cracks were more common.

Observed microfractures were quantified by fracture densities, which define a damage zone around faults. Studies considered fault damage zones to end when some form of background level was reached, signifying the end of deformation associated with a fault or shear fracture. Anders & Wiltschko (1994) saw densities drop to background between 3 and 18m from the Arches National Park Fault, a normal fault located in Navajo and Entrada Sandstones. Similarly, Brock & Engelder (1977) observed drops in densities between 4 and 20m from the Muddy Mountain Overthrust in Aztec sandstone with initial rapid decrease within 1 – 2 m from the fault plane.

Because of widespread sampling locations for other large faults, Wilson et al. (2003) along with others (Vermilye & Scholtz, 1998) display microfracture density data on a log scale. Wilson et al. (2003) observed a damage zone width associated with the Punchbowl fault extending 30m. Locally, near subsidiary faults, Wilson et al. (2003) found that fracture density would increase.

On another comparably large fault, Caleta Coloso fault in Chile, Faulker et al. (2006) documented a damage zone width of 150 m. Unlike all preceding damage zone quantifications, Friedman (1969) used an index value determined by the number of microfractures in 200 random grains that were separated into categories and turned into percentages. Even though this is a different method, it still demonstrated that microfracture density decreases with distance from faults.

Several small-scale faults in the Shawangunk Mountains of New York, also demonstrate decreasing microfracture density away from a fault plane (Vermilye & Scholz, 1998). Five faults, four strike-slip and one reverse fault, all had damage zones less than 1 m, ranging from 2.5 cm around Gertrude's Nose reverse fault to 65 cm around

the strike-slip Mossy Maple fault. The damage zones are asymmetric in microfracture distribution. One side of each fault has a higher microfracture density than the other. Not only do strike-slip faults have asymmetric microfracture densities due to asymmetric stress regions, they also have asymmetric microfracture orientations associated with their fault planes. Vermilye & Scholz (1988) documented low angle microfractures (~20°) on the compressive side, and high angle microfractures (~50°) on the dilatational side of three strike-slip faults. One of these, the Alliegerville fault, has low angle microfractures that become shallower with distance from the fault and high angle microfractures that remain constant but only extend 50mm away from the fault. Orientations of microfractures in the Shawangunk outcrops, associated with fault tips do not exhibit the same asymmetry. Microfractures form at low angles to the fault and are symmetric about the fault tip. They hypothesized that mode I propagation occurred at the tip leading to symmetric orientations.

Orientations of microfractures associated with a normal fault (Arches National Park fault) are most commonly subparallel to the fault plane, ranging from 5° to 20°, with another subset normal to the fault plane (Anders & Wiltschko, 1994). There was no significant variation in orientation with distance from the normal fault.

Field studies investigating microfractures associated with faults identified three types of microfractures: intragranular, transgranular and grain boundary. Microfractures were found to be both straight and curvilinear. All studies, that quantified microfracture density, documented decreasing microfracture density with distance from the fault. Damage zones, defined by microfracture density, were asymmetric in both density and microfracture orientation around shear faults and symmetric in density and orientation

around fault tips and normal faults. These will later be compared to NHF microfracture characteristics.

6.1.1.2 Experimentally Induced Damage Zones

Like natural faults, shear, compression, and tension experiments have all been observed to form microfractures (Menendez et al., 1995; Moore & Lockner, 1995; Janssen et al., 2001; Hoxha et al., 2004; Katz & Reeches, 2004; Takemura & Oda, 2004; Gannen & Vervoort, 2007). Experimental studies characterize microfractures associated with laboratory-produced shear and tension fractures, using similar methods as previously discussed field studies. They discuss microfracture appearance, microfracture density, damage zone shapes and microfracture orientation.

Microfractures formed in granite (Hoxha et al., 2004; Katz & Reeches, 2004; Takemura & Oda, 2004) include intraganular, intergranular and grain boundary cracks. During compression, as peak stress is approached, tensile intragranular fractures are formed first and grow toward grain boundaries (Katz & Reeches, 2004). After peak stress Takemura & Oda (2004) found that cracks grow across grain boundaries forming intergranular microfractures. Finally, if a sample is loaded to failure, grain boundary cracks are formed primarily in post-failure (Takemura & Oda, 2004). Grain boundary cracks that propagate before failure are perpendicular to the compression direction. After failure crack tensors show that microfractures don't grow preferentially (Takemura & Oda, 2004). Grain boundary cracks were attributed to cause the majority of dilatancy. These fractures formed in compression have sharp straight traces but some undulated. This characteristic is similar to microfractures associated with with natural faults and fractures (previously discussed).

In contrast, Menendez et al. (1995) found, in sandstones, that most dilatancy before sample failure was due to intergranular cracking, proposed to be shear rupture of lithified and cemented grains. Intragranular cracks initiate at grain contacts only very near peak stress, causing a significant increase in microfracture density.

Uniaxial tests form microfractures under compression and tension. Ganne & Vervoort (2007) did a series of compression and tension tests on limestone. They observed microfractures in just compression or tension and then subjugated samples to compression followed by tension or vice versa. Moore & Lockner (1995) and Janssen et al. (2001) both formed a shear fractures in granite through compression and observed associated microfractures. Rigopoulous et al. (2011) analyzed and compared microfractures formed under compression in a hazburgite and a serpentinized dunite. All four studies observed grain boundary cracks, intra and intergranular cracks; only the last studied observed transgranular cracks. On average the majority of microfractures were intraganular and cited as shorter than the average grain size. Intragranular cracks associated with a shear fracture were commonly aligned with the edge of a single crystal and intergranular cracks usually had markedly different orientations on either side of a grain boundary (Moore &Lockner, 1995).

Microfractures associated with the series of compression and tension tests executed by Ganne & Vervoort (2007) suggest that numerous long intragranular cracks propagate to become part of an intergranular crack. They showed this by documenting intraganular cracks in a sample that had solely undergone compression, then documenting an intergranular fracture with associated intragranular cracks from a sample that had undergone compression followed by tension.

Some of the experimental work (discussed above) quantified microfracture density. Most found an area crack density (# of fractures/mm^2) (Moore & Lockner, 1995; Janssen et al. 2001; Katz & Reeches, 2004; Takemura & Oda, 2004) while others used a linear approach (# of fractures/mm) similar to this study (Menendez et al., 1995). Moore & Lockner (1995) was the only study to define a damage zone, stating that cracking intensity became visibly greater at 18mm on either side of the shear fracture and at 10mm in front of the fracture. They found a 25-35% increase in crack density over background levels at these distances attributing this increase as the threshold level for visually perceptible change. Remaining studies that quantified crack density, used it to compare different stress parameters. Takemura & Oda (2004) determined that, in granite, failure starts when area crack density reaches three to four times that of the intact rock.

Experimental studies identified all four types of microfractures associated with shear fractures or in post failure samples. Intragranular, intergranular and grain boundary cracks were abundant while transgranular cracks were only observed in Rigopoulous et al. (2011) experiment. Microfractures were used to find a microfracture density but only one study reported a damage zone (18mm on either side of the shear fracture, 10 mm in front). Unfortunatly, none of these studies collected microfracture orientations, which has been a large part of this study. Observed microfracutres from laboratory tests will later be compared to those found in NHF experiments.

6.1.2 Process Zones

The process zone precedes the damage zone. Here, the development of crack tip microcracking takes place in a non-linear behavior leading to macrocrack extension through linkage of microfractures (Atkinson, 1987). Unlike the damage zone,

microfractures are in the process of active linkage and propagation. Studies investigate process zones in natural and experimentally produced faults and shear fractures, and dikes.

6.1.2.1 Natural Fault and Experimental Process Zones

Some studies, investigated process zones and tip behavior as well as damage zones associated with natural faults (McGrath & Davison, 1995; Vermilye & Scholz, 1998), experimentally produced fractures (Moore & Lockner, 1995; Janssen et al., 2001) and experiments paired with models (Reeches & Lockner 1994). None of these studies involve pure tension. Microfracture densities and orientations are the focus of these studies.

In filed studies, strike-slip faults were found to have mode I and mode II microfractures associated with their tips (McGrath & Davison, 1995; Vermilye & Scholz, 1998), with corresponding asymmetric crack densities and orientations dependent on the sense of slip. Vermilye & Scholz (1998) noted that crack density was highest at the center of faults and decreases towards the tips.

Under uniaxial compression Janssen et al. (2001) produced shear fractures with tips and process zones. They found that crack densities decrease toward the fracture tip and noted a scatter in crack orientation moving toward the fracture tip. In contrast, Moore & Lockner (1995) found the highest crack densities in front of shear fracture tips, yet the process zone did not extend out in front (10mm) of the fracture as far as the damage zone extended (18mm). Three experiments (Hadley, 1974; Reches & Lockner, 1994; Moore & Lockner, 1995) utilized acoustic emissions to investigate process zones. They found

that before failure, microfractures are generated throughout a sample and after failure microfractures are localized in a process zone.

Studies involving process zones are rare, because it can be hard to capture a fault or fracture tip. Those studies that did, found that crack density decreased toward fault or fracture tips in both field studies and experiments. Except in More & Lockner's (1995) laboratory produced shear fracture where crack density was highest at the fracture tip but its process zone was not as large as its damage zone. These observations will be compared to process zones found in SPss-2.

6.1.2.2 Dike Process Zones

Studies concerning joint process zones are not yet abundant, therefore an alternative form of extension will be used in order to understand and compare process zones in a completely tensional environment. Dike tips are recognizable in the field and form tensional stress regions. They form easily observed process zones.

There are two models of dike formation 1) fracture – fill model based on the idea that magma intrusion is easier along pre-existing fracture systems or weaknesses (Billings, 1972) and 2) hydraulic tensile fracturing model involving magma pressure that overcomes the tensile strength of the host rock and propagates a new fracture (Motoki & Sichel 2008). Motoki and Sichel's (2008) field observations support magma pressure forming hydraulic fractures in a dike swarm located in Arraila de Cabo, Brazil. Kimberlite intrusion in South Africa (Basson & Viola, 2004) also follows hydraulic fracture as a model of emplacement. Delaney et al. (1986) predominantly attributed dykes in the southwestern U.S. to the fracture – fill model but found one dike that deviated from

the model, which was proposed to form by hydraulic fracture. Both Basson & Viola (2004) and Delaney et al. (1986) document dike tips and their associated structures.

Delaney et al. (1986) investigated three substantial dike complexes within the Colorado Plateau Province: Ship Rock in New Mexico, Alhambra Rock in Utah and Willow Wash Dike in Utah. All three complexes had associated dike parallel joints that were found to be pre-existing and invaded by dikes (model 1). In only one situation was a dike proposed to have formed by hydraulic fracture (model 2). The northern section of the Western Willow Wash dike includes adjacent parallel fractures but not local fractures, which all other sections of the dike had. Here the dike also had more dense adjacent fractures then the rest of the dike. Based on field observations Delaney et al. (1986) concluded that this part of the dike was emplaced by producing its own fractures. As seen in fault and fracture damage zones, joint frequency decreases with distance from the dike, are symmetrical on both sides of the dike and in this case are restricted to 15m from the dike.

Basson and Viola (2004) studied fractures associated with kimberlite dikes. They found dike parallel joints extending symmetrically 2-4 m away from dikes defining a pure dilatational region. Within this zone “feathered” dike terminations were identified. Meaning that narrow planar kimberlite stringers (small dikes) occupied dilated fractures ahead of the main body of the dike. Orientation of stringers or viens parallel with the dike further suggests pure dilation with no shear present (Basson and Viola, 2004).

Dike process zones show similar characteristics as process zones formed in field and experimental studies. Fracture density decreased away from the dike tip and like normal faults, exhibits symmetry. Both studies indicated that fractures are present ahead

of the main structure. These process zones will be compared to the process zones found in SPss-2

6.2 Comparison of NHF to Previous Studies

6.2.1 Damage Zones

6.2.1.1 Natural Fault Damage Zones

Comparison of microfractures formed by natural processes with our laboratory-produced microfractures shows more similarities than dissimilarities. Both processes form curvilinear fractures that are intragranular, transgranular and follow grain boundaries. Even though NHF microfractures don't form the same shape damage zones as natural fractures and faults, they both exhibit exponential decrease of microfracture density away from a fault or fracture surface. The characteristic orientation does not change when moving away from some natural surfaces or our laboratory-produced surfaces. With these similarities in mind, we can say that microfractures produced under laboratory conditions have similar characteristics as those formed through geologic process.

Unlike most field studies, this study focuses on open microfractures, formed during NHF experiments, and considers fluid inclusion planes as pre-existing background microfractures. Characteristics of microfractures between natural fault and shear fractures include microfracture appearance, microfracture density, damage zone shapes and microfracture orientation.

Like Anders & Wiltschko (1994), straight and curved microfractures were also observed in our investigation as well as intragranular cracks, which initiate or propagate

towards grain-to-grain contacts. This may be due to higher stress concentrations found at grain-to-grain contacts. Intragranular cracks parallel to adjoining grain contacts were observed in our study, similar to the ones found in the Shawangunk Mountains by Vermilye & Scholz (1998). In that study the majority of microfractures were transgranular. In our study transgranular cracks are most prevalent in heterogeneous isotropic SPss-2 around non-through-going fractures and closest to the main NHF for all samples. Mode I microcracks observed in natural faults and our laboratory-produced fractures are similar in type and placement within grains.

Natural damage zones, defined as a zone of microfractures around a fault do not have similar characteristics as damage zones produced by NHFs in laboratory conditions, but they do exhibit comparable mechanical properties. While the scale of fault damage zones is much larger than those adjacent to NHFs, comparisons can still be drawn. In all field studies, microfracture density decreases with distance from a fault or shear fracture (e.g. Friedman, 1969; Brock & Engelder, 1977; Anders & Wiltschko, 1994; Vermilye & Scholz, 1998; Wilson et al., 2003; Faulkner et al. 2006) just as seen for each NHF produced under experimental conditions (Figure 6.1) (See Table 6.1 for a compilation of all discussed damage zones).

Wilson et al.'s (2003) field study was the only case where there are areas of higher microfracture density away from the fault surface. The increase in microfracture density was associated with subsidiary faults of the Punchbowl fault, and is comparable to the behavior in SPss-2. Linear crack density increases locally 2-2.5 mm above the main NHF and is attributed to a non-through-going fracture that propagated parallel to the main NHF. The crack density at this location is 2.1 times that of the intact rock and

1.3 times that experienced along the NHF. This suggests that the crack density along the fracture may underestimate that needed for failure.

Damage zone shapes can also be compared between natural faults and fractures and experimentally produced NHFs. To best compare damage zones, smaller scale faults and shear fracture that are closer in size to NHF damage zones are used. Damage zones surrounding the Shawangunk Mountain faults (Vermilye & Scholz, 1998) have very different shapes than those observed around NHFs even though they have similar damage zone widths (Figure 6.2). The asymmetry observed in the Shawangunks is expected across strike slip faults but not seen in damage zones associated with NHFs. However, asymmetry is observed in two locations where standard deviations across the fracture surface overlap each other, suggesting that microfracturing is not preferential on either side of the NHF. The asymmetric locations are 1) SPss-2 at 2-2.5mm where an intense microfracture zone, possibly a non-through going fracture has increased damage and 2) adjacent to the NHF surface on the top of SPss-1, where this side of the fracture could have incurred more damage than the bottom side.

Microfracture orientations are used to compare between natural structures and laboratory produced Microfractures associated with the NHFs. Figures 6.3, 6.4 and 6.5 show all microfracture orientations collected for each sample. Microfractures that formed in this study have similar orientations to those that formed in the Arches normal fault. Anders & Wiltschko (1994) found no significant variation in orientations with distance from the fault, justifying conclusions drawn from composite plots of all locations. Significant variations in microfracture orientation with distance from the NHF are not apparent in cores. Composite plots for each sample above and below the NHF (Figures

6.6, 6.7 and 6.8), and composite plots showing microfracture orientations with distance from NHFs (Figures 5.20, 5.24 and 5.26), demonstrate that there is no significant variation in orientation moving away from the NHF. This suggests all microfractures formed in tension as they are parallel to the maximum compression direction.

Microfractures formed by a laboratory produced NHF, form similar types of microfractues as natural faults. They both have associated intragranular, transgraunular and grain boundary microfractures that can be straight or curvilinear. These microfractures form in similar areas of grains: parallel to grain boundaries and radiating from grain-to-grain contacts. Damage zones defined by these microfractures also show similarities. Decreasing density with distance from faults and NHFs is observed. However, the shapes of fault damage zones are not similar to those found around NHFs. Damage zones around NHFs are symmetric, while asymmetry is often observed in nature. Asymmetry arises from strike-slip or thurst faults. Thus, the symmetric damage zones observed around NHFs supports a pure opening mode fracture. Orientations of microfractures that make up damage zones are similar to microfracture orientations associated with the Arches normal fault and also support a pure opening mode fracture.

6.2.1.2 Experimentally Induced Damage Zones

Microfractures produced in triaxial vessels (Menendez et al., 1995; Hoxha et al., 2004; Katz & Reeches, 2004; Takemura & Oda, 2004;) and uniaxial vessels (Moore & Lockner, 1995; Janssen et al., 2001; Ganne & Vervoort, 2007) are compared to those produced in our own triaxial experiments. Triaxial tests form microfractures under different stress states and in different rocks. They also undergo different deformation than seen in our hydraulically influenced deformation, such as grain crushing and pore

collapse (Menendez et al., 1995), rolling and sliding of disintegrated blocks (Takemura & Oda, 2004), and shear bands (Menendez et al., 1995). When comparing microfractures formed without hydraulically influence to NHF microfractures, focus will be on tensile fractures formed in low porosity rocks under various experimental conditions, not on grain crushing, pore collapse, sliding of disintegrated blocks or shear bands.

Microfractures produced in triaxial tests can have sharp straight traces and can undulate. This characteristic is similar to microfractures associated with our NHFs, as well as those associated with natural faults and fractures (previously discussed). In uniaxial tests, the majority of microfractures were intraganular and cited as shorter than the average grain size, like most of ours. Alignment of intragrnular cracks with the edge of a grain or crystal and changing orientation of intergranular cracks when crossing a grain boundary was seen in Moore & Lockner's (1995) experiments as well as in our samples and can be seen in the non-through going fractures from SPss-2 (Figures 5.8, 5.9 and 5.10).

Ganne and Vervoort (2007) documented an intergranular fracture with associated intragranular cracks from a sample that had undergone compression followed by tension. Non-though-going fractures from sample SPss-2 show similar characteristics, suggesting that during NHF propagation, numerous intragranular and grain boundary cracks propagate to become part of a transgranular-intergranular fracture, forming a non-though-going NHF. Figure 6.8 shows fracture traces from Ganne & Vervoort's (2007) experiments and fracture traces from NHF experiments. Non-though-going fractures from NHF experiments most closely resemble fractures formed in tension (Figure 6.9-A-1) or fractures formed in compression followed by tension (Figure 6.9-A-2). They all have

similar branching patterns and local fracture lenses. The fracture formed solely in tension has en échelon fractures like Figure 6.9- C. Fractures formed in compression and then tension resemble those from NHF experiments because the sample fractured while in tension. Intragranular microfractures grew while the sample was under compression but an intergranular fracture was not formed until the sample underwent tension. NHF fractures do not resemble fractures that formed in tension and then compression. This suggests that our samples did not form microfractures as the samples relaxed after dilation.

Microfracture density can be compared with NHF quantifications. A major difference in microfracture density in laboratory-induced fractures is that densities are symmetrical with tensile failure and asymetrical with shear failure (Moore and Lockner, 1995). As previously discussed, densities in natural rock faults also show symmetrical microfracture densities associated with tensile failure. Symmetrical microfracture densities found in both NHF laboratory tests and natural faults support the conclusion that microfractures investigated in this study were formed under tensile failure.

As in damage zones of other laboratory-produced fractures, damage zones in this study extend to where the crack density reaches zero when the background crack density is subtracted from it. Average liner crack density – background crack density, with distance from each NHF are shown in Table 6.2 and on either side of non-through-going fractures in Table 6.3. Homogeneous – isotropic, SPss-1, has the largest amount of damage, while homogeneous – anisotropic, Abo formation, had the smallest increase in damage. This suggests that under the same conditions SPss-1 required more damage to fail than the Abo formation. SPss-1 required more damage to fail than the Abo formation

but it failed much faster (figure 2.3). Therefore, initiation and propagation occurs much faster and causes more damage in a homogenous-isotropic rock than it does in a homogeneous-anisotropic rock.

In NHFs failure occurred when linear crack density reached 13.81 frac/mm higher than intact rock for SPss-1, 4.65 frac/mm higher than intact rock for SPss-2 and 8.88 frac/mm higher than intact rock of Abo. These failure criterions may be underestimating the true linear crack density for failure, because linear crack density has been quantified on both surfaces of the NHF. A true value should be established with a transect running through the NHF. This was not possible because the samples separated completely and could not be put back together. A highly microfractured zone about 2mm above the main NHF, of SPss-2 could be an area that came close to failure. The crack density at this location is 6.35 frac/mm higher than the intact rock, which is nearly two times higher than the 4.65 frac/mm experienced along the NHF in SPss-2. Linear crack density at known non-through-going fractures, above the main NHF, range from 2.57 frac/mm to 3.61 frac/mm higher than the intact rock. These values are a little bit lower than those found along the NHF. At all three of these locations, failure did not occur. Therefore, the amount of damage has to be higher than that recorded at the NHF and should be close to the highest recorded linear crack density. Based on linear crack density at the NHF, it can be concluded that more damage was required for SPss-1 to fail than SPss-2 and more damage for SPss-2 to fail than Abo.

Microfracture characteristics are similar between NHFs and other laboratory produced fractures. They show similar characteristics in shape and behavior as a fracture failed in tension from Ganne and Vervorrt's (2007) experiments, but are dissimilar when

compared to a fracture failed under compression. Microfracture density shows similarities and differences as well. As in field studies, asymmetric microfracture densties are documented around laboratory produced shear fractures, and a decrease in microfracture density with distance from a fracture is observed. Where the percent increase in crack density becomes zero defines damage zones for NHFs from this study and other laboratory produced fractures. The percent increase in crack density at a fracture provides a failure criterion. NHF percent increase in crack density challenges that failure criterion suggesting that it takes more than the microfracture density at the fracture surface to truly cause failure.

6.2.2 Process Zones

Damage zones exist in all three cores, but process zones may only be found in the heterogeneous-isotropic sandstone, SPss-2, because it is the only sample to form non-through-going fractures. The other two samples, the Abo formation and SPss-1, don't have process zones because the NHF fully propagated leaving behind a fully formed damage zone. Non-through-going fractures found only in Spss-2 provide possible fracture tips for analysis. Only two of the non-through-going fractures terminated in the thin section, figure 5.8 and figure 5.9 and can be compared to know tip characteristics. Both possible tips in this study show decreasing density towards the tip but no clear scatter in orientation.

Delaney et al. (1986) suggested that both extension fractures and dikes experience a local loss of cohesion at their tips due to the formation of microcracks or adjacent joints. This area of loss of cohesion forms a process zone of weakened rock, which is cut

symmetrically by the parent structure (Delaney et al., 1986). For extension fractures microcrack characteristics are controlled by grain scale heterogeneities. Dike joint characteristics are controlled by outcrop scale heterogeneities. For both, the process zone extends out in front of the propagating dike or extension fracture. In both non-through-going fractures that terminate within the thin section plane microfractures extend beyond the connected fracture segments.

Unlike some experiments (Hadley, 1974; Reches & Lockner, 1994; Moore & Lockner, 1995), acoustic emissions data were unavailable for NHF experiments, so thin section methods were relied on for process zone and microfracture extent analysis. All studies previously discussed involve mode III, mode II and mode I failure. None of them have been pure mode I propagation. Comparisons between NHFs and faults or shear fractures can be made, but to truly uncover the characteristics of process zones and joint fracture tips, a move must be made toward pure extension studies.

6.3 Conceptual Model/ Fracture Formation

Experimental data from the formation of NHFs discussed in this study, suggests that dilation of cores was accomplished by propping open pores, initiating and propping open microcracks sub-perpendicular to the core axis as well as closing pores and microcracks sub-parallel to the core axis (French et al., 2012). Open microfractures support this theory because the majority of open microfractures observed are sub-perpendicular to the core axis. Microfractures opening sub-perpendicular to the core axis will cause the core to dilate forming more space in the rock, providing an explanation for minor permanent volume change in SPss-2 and SPss-1. Various sized damage zones associated with each NHF also supports French et al.'s (2012) hypothesis that fluid

driven dilatancy and grain scale-damage, not differential stresses caused fracture formation.

Because NHFs are completely formed, any non-through-going fractures give insight on a newly propagating fracture, as they have not fully pulled apart. These show that NHFs developed as grain boundary cracks, inter- and intragranular microcracks linked and locally propagated across grains, accompanied by development of a microfracture damage zone, in which the majority of cracks are similarly oriented to the fracture segments. If the termination seen in Figure 5.8 and the ending of echelon segments in Figure 5.9 are fracture tips, a conceptual model of natural hydraulic fracture propagation can be made. Figure 6.10 shows the process of a natural hydraulic fracture.

First formation of microfractures, intragranular and grain boundary, occurs on a mechanical heterogeneity or where pore pressure, stress and strain reach a maximum (Figure 6.10-A). These microfractures will then start to link or another microfracture will propagate off the end of an opened microfracture, forming small intergranular and transgranular microfractures (Figure 6.10-B&C). Formation and linkage will occur perpendicular to maximum tension, with the majority of microfractures oriented within 30° (as observed in this study) to the main fracture. Formation of fracture bound lenses begins as microfractures link forming a connected network (Figure 6.10-D&E). More microfractures form away from the connected network and some link up.

As this zone of connected microfractures moves through a rock, forming a fracture, microfractureing does not cease. For a fracture to build up enough aperture to break a rock, microfractures continue to form until a large enough, uncohesive enough zone is built that is continuous from one side of the rock to the other. Once this zone

reaches a maximum, above 2 times the crack density of intact rock, the fracture is able to break the rock (Figure 6.10-F). As fracture bound lenses grow microfractures continue to propagate symmetrically on either side of the NHF. This is how damage zones around NHFs get so much larger than the damage zones around non-through-going fractures.

As suggested earlier, the linear crack density at the NHFs may not represent the true value for a NHF because it only represents one sides of the fracture wall, not a measurement through a fracture. The fully connected non-through-going fracture (5.10) is connected all the way through and its aperture is not great enough to separate the rock. Along its surface, fracture lenses or bands are noted. I propose for a NHF to fully separate, rock fracture bound lenses have to propagate its entire length. The area 2mm above the NHF formed in Spss-2 demonstrates this hypothesis. Here there is a zone, highly microfractured, with fracture bound lenses. This zone had the highest linear crack density found in the entire study and could be were final fracture failure was about to occur.

This conceptualization of fracture formation does not match the traditional definition of a process zone. It's different than the dike tips discussed earlier (Delaney et al., 1986; Basson & Viola, 2004). Instead of continuous propagation forward, there is first a build up of a connected microfractures, referred to as fracture bound lenses. At the same time, microfractures continue to initiate away from the main connected structure and sometimes link up. In the traditional sense of a process zone, microfractures stop forming as the propagating tip moves away. The hypothesis that a connected band of microfractures develops and propagates through a rock while the damage zone continues to grow everywhere throughout the sample, suggests that fracture initiation and

propagation in NHF is different than what has been observed and documented in other types of fractures.

CHAPTER 7

CONCLUSION

Microfractures formed during NHF propagation are all tensile cracks. Grain boundary, transgranular, inter- and intragranular cracks were all observed adjacent to each NHF. Characterization shows that:

1. Grain boundary and intragranular cracks are the most common throughout the whole samples and transgraunlur are more common close to non-through going fractures (in SPss-2) and NHFs. Creation and dilation of these microfractures resulted in observed permanent volume change.

2. Microstructure investigation of three different rocks shows that anisotropy and heterogeneity both affect how NHFs initiate and propagate. The homogeneous isotropic sample (SPss-1) has the broadest microcrack damage zone while the heterogeneous isotropic sample (SPss-2) has the narrowest damage zone, and the homogenous anisotropic sample (Abo) has an intermediate microcrack damage zone. Multiple fractures with damage zones narrower than the NHF are only found within SPss-2 and are a function of heterogeneity. Damage zones surrounding these non-through-going fractures suggest that as microfractures link to form NHFs, associated microcrack damage zones are developing.

3. Fracture roughness also varies with rock characteristics. The most planar fracture formed in the homogenous isotropic sample, SPss-1; less planar fractures are associated with samples that exhibit heterogeneity and anisotropy.

4. Damage zones formed by faults and shear fractures do not have similar shapes as those formed by NHFs but they exhibit comparable behaviors to those formed by NHFs. Similar behaviors between NHFs and faults or shear fractures include, a decrease in crack density with distance from a structure, and sharp increases when encountering a secondary structure. Fracture orientations in faults and shear fractures are also similar to microfracture orientations found in NHFs. Microfractures are shallowly dipping with respect to the NHF, also observed around normal faults and on the compressive side of strike-slip faults.

5. Non-through going fractures closely resemble fractures formed during uniaxial tension experiments and compression followed by tension experiments. They do not resemble fractures formed in tension followed by compression experiments.

6. More crack damage is needed for an NHF to propagate than extensile fractures or shear fractures.

7. Formation of NHFs starts where pore pressure, stress and strain reach a maximum (3)_2) or on a mechanical heterogeneity (SPss-2 and Abo). Propagation occurs as microfractures oriented 30° or less from perpendicular to maximum tension accumulate symmetrically around the fracture initiation point, forming a connected network. This connected network builds up while microfractures simultaneously grow away from the main structure. The connected network grows

this way until it reaches a stopping point, ie the end of the sample. Once the connected network spans the entire rock a critical loss of cohesion causes the fracture to break the rock. This critical value has to be greater than the highest linear crack density values experienced by each rock.

By understanding damage zones surrounding NHFs hydrologic implications can be made, leading to a better comprehension of fluid flow through exhumed NHFs.

8. Broader damage zones surrounding NHFs in homogeneous rocks are expected to be zones of higher matrix porosity and permeability.

9. Heterogeneous rocks have the potential of increased fracture permeability throughout the rock volume. As they have more mechanical heterogeneities providing more opportunities for fracture formation.

10. Microfracture damage zones add storage capacity and opportunities for increased matrix diffusion influencing contaminant transport.

Microfracture characteristics observed in this study are a base for future microfracture work. Joints on the surface of the Earth today, proposed to form by high fluid pressure, can be verified by comparing their healed microfractures with those in this study and fluid behavior through NHF conduits can be better characterized.

FIGURES

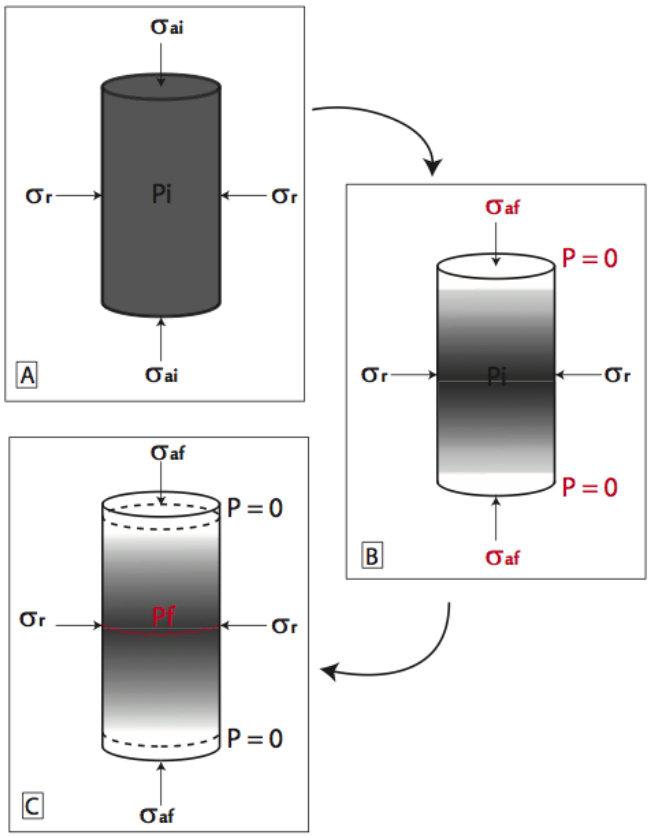

Figure 2.1. Experimental procedure for producing NHF's in the laboratory. A) Initial conditions were $\sigma_r > \sigma_a$ with a uniform internal pore pressure, Pi. B) First confining pressure was increased to σ_r while axial load was simultaneously increased to σ_a, so $\sigma_r = \sigma_a + 2$MPa. Next a uniform pore pressure was raised to p, now $\sigma_r > \sigma_a > p$. C) p is reduced manually while σ_a was reduced to 2 MPa as p reduced to 0 MPa. This causes $p > \sigma_a$ everywhere except at the end caps. A Pore fluid pressure gradient Δp and an effective stress σ'_3 parallel to the core axis is produced (French, 2012).

A.

B.

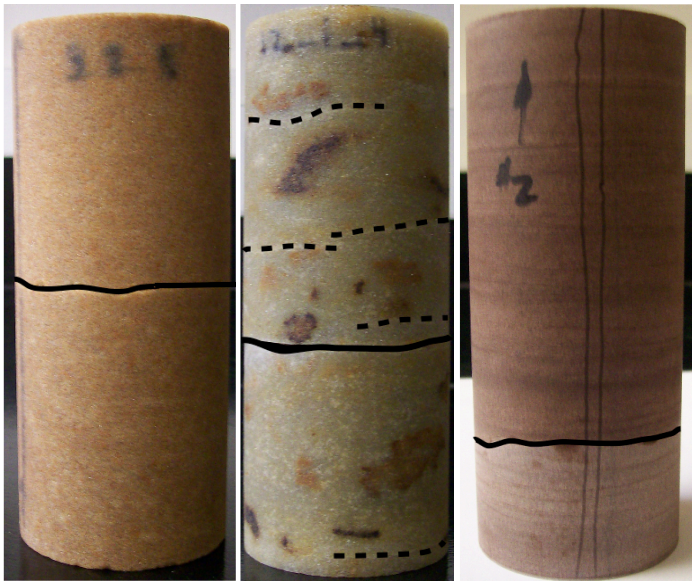

Figure 2.2. Core images after NHF experiments. A) Each core with one primary through going fracture. B) Cores with NHFs outlined in black and non-through going fractures outlined in dashed black lines (French, 2010).

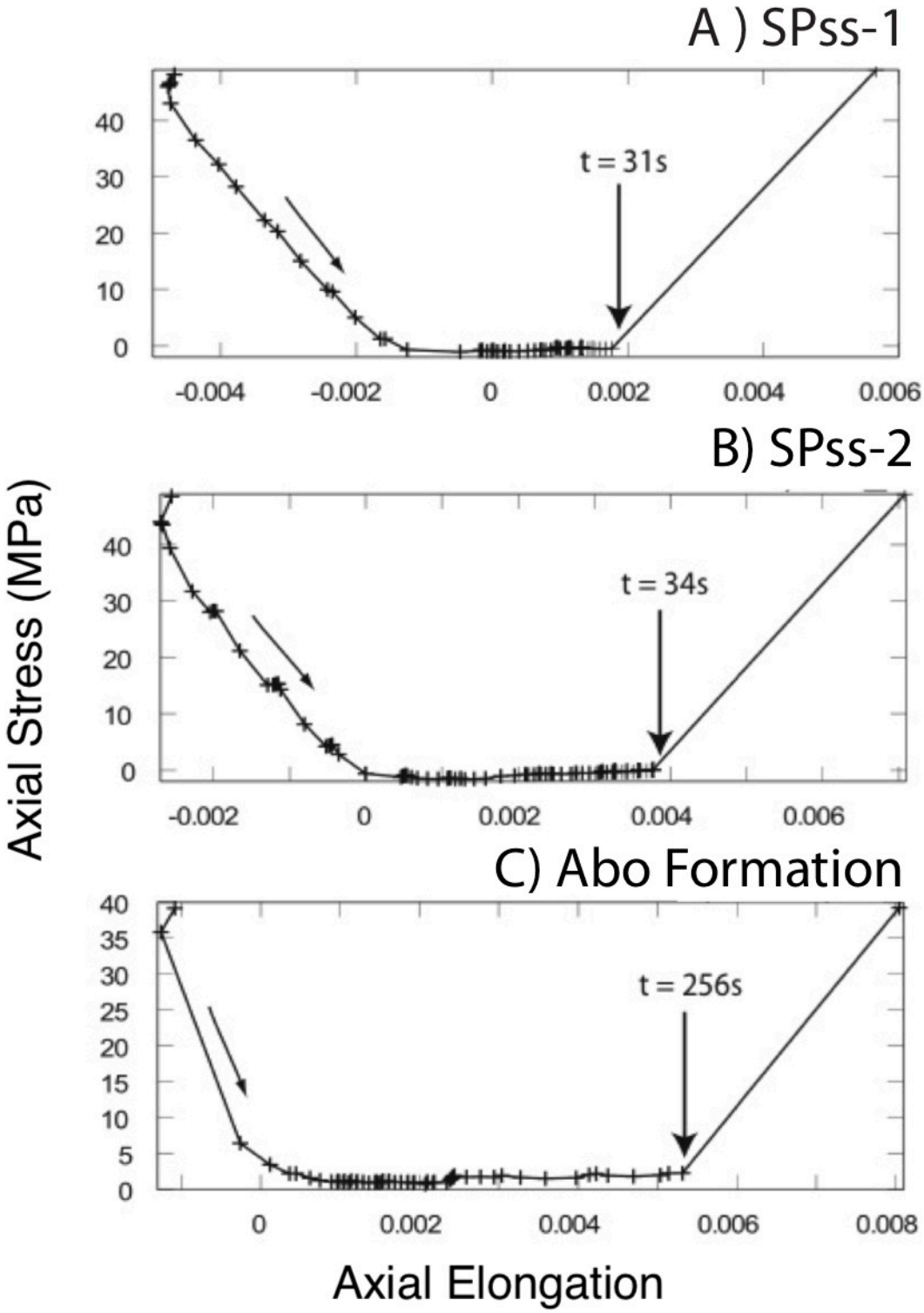

Figure 2.3. Cores, axial stress vs. axial elongation during NHF experiments. The down arrow shows the unloading path, followed by a time of significant axial elongation and ultimately failure at the next down arrow. The time until failure is indicated for each sample. A) SPss-1. B) SPss-2. C) Abo (French, 2011).

Sample	Mean Grain Diameter (mm)	Max Pore Diameter (mm)	Porosity %	Tensile Stregth (MPa)	Bulk Modulus (GPa)
SPss-1	0.195	0.48	8.6	1.7 ± 0.2	5.2
SPss-2 bulk	0.192	0.78	8.8	3.8 ± 0.2	6.14
Spss-2 conc.	0.16	0.49	5	n/a	n/a
Abo Fm.	0.0638	n/a	6	6.8 ± 0.7	10.99

Table 3.1. Sample characteristics. The mean grain diameter (mm), max pore diameter (mm), porosity, tensile strength and bulk modulus for each sample in this study.

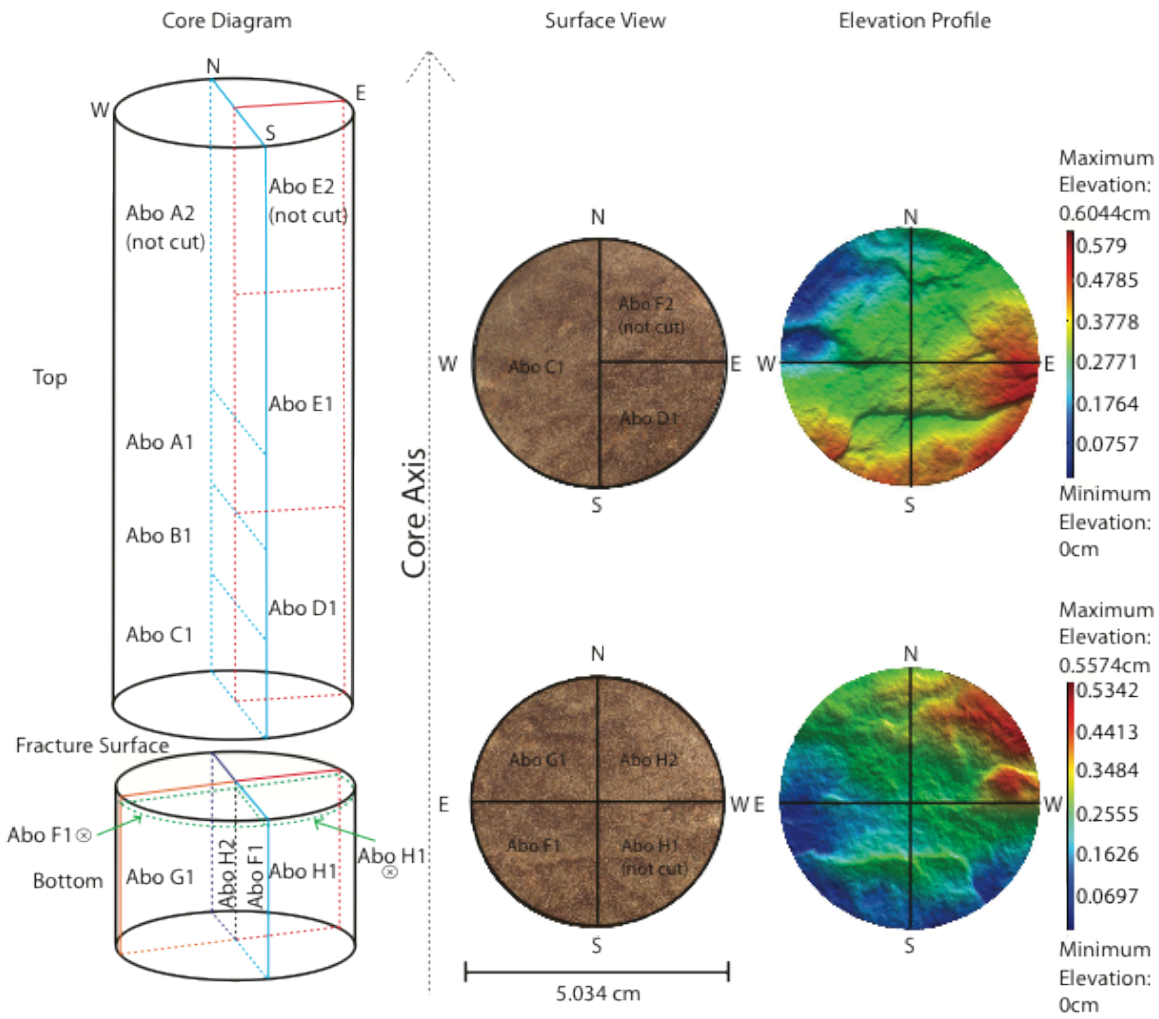

Figure 4.1. Homogeneous – Anisotropic (Abo Fm.) core diagram. Showing orientation of thin sections, fracture surface images and fracture surface elevation profiles.

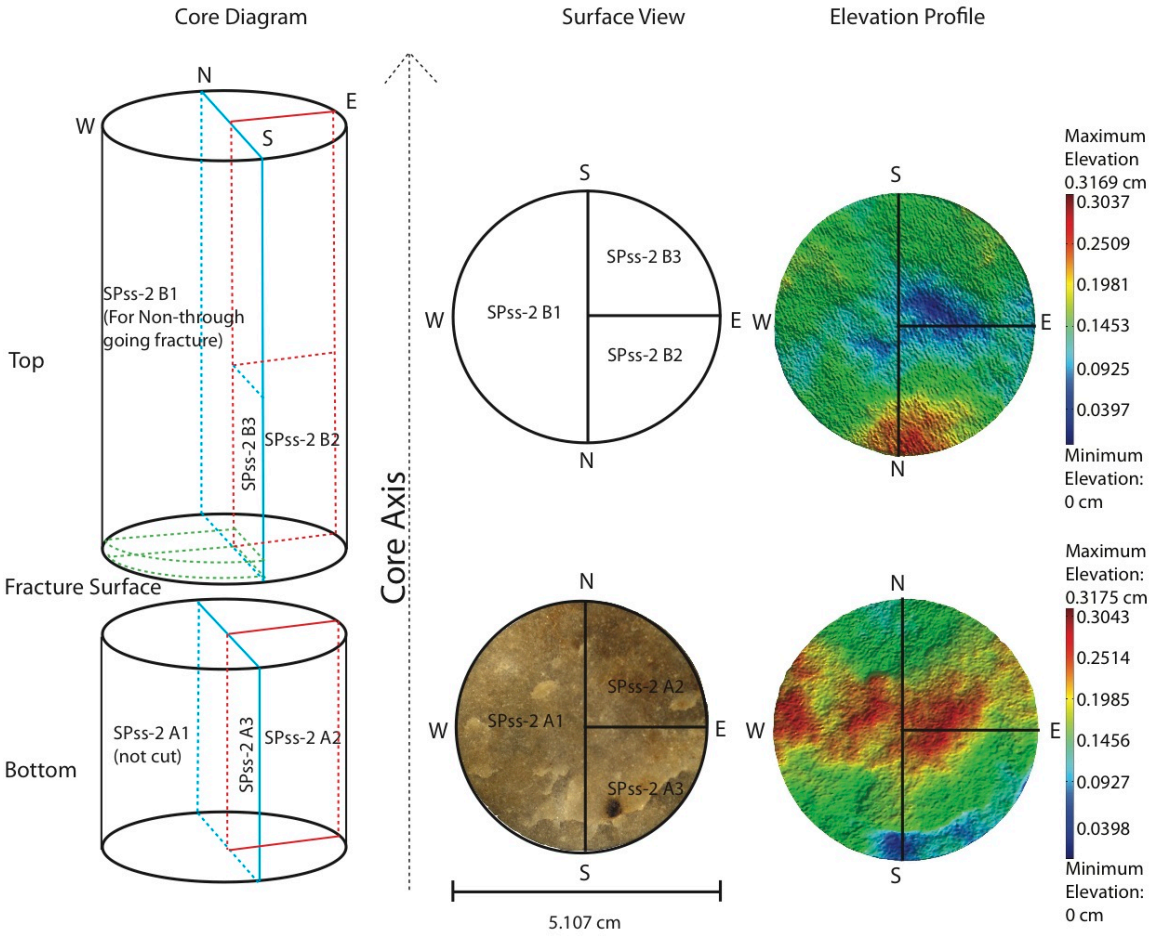

Figure 4.2. Heterogeneous – Isotropic (SPss-2) core diagram. Showing orientation of thin sections, fracture surface images and fracture surface elevation profiles.

S N

Figure 4.3. Section of SPss-2 (B1) used to create non-through going fracture thin sections. South and North line up with core diagram found in Figure 4.3.

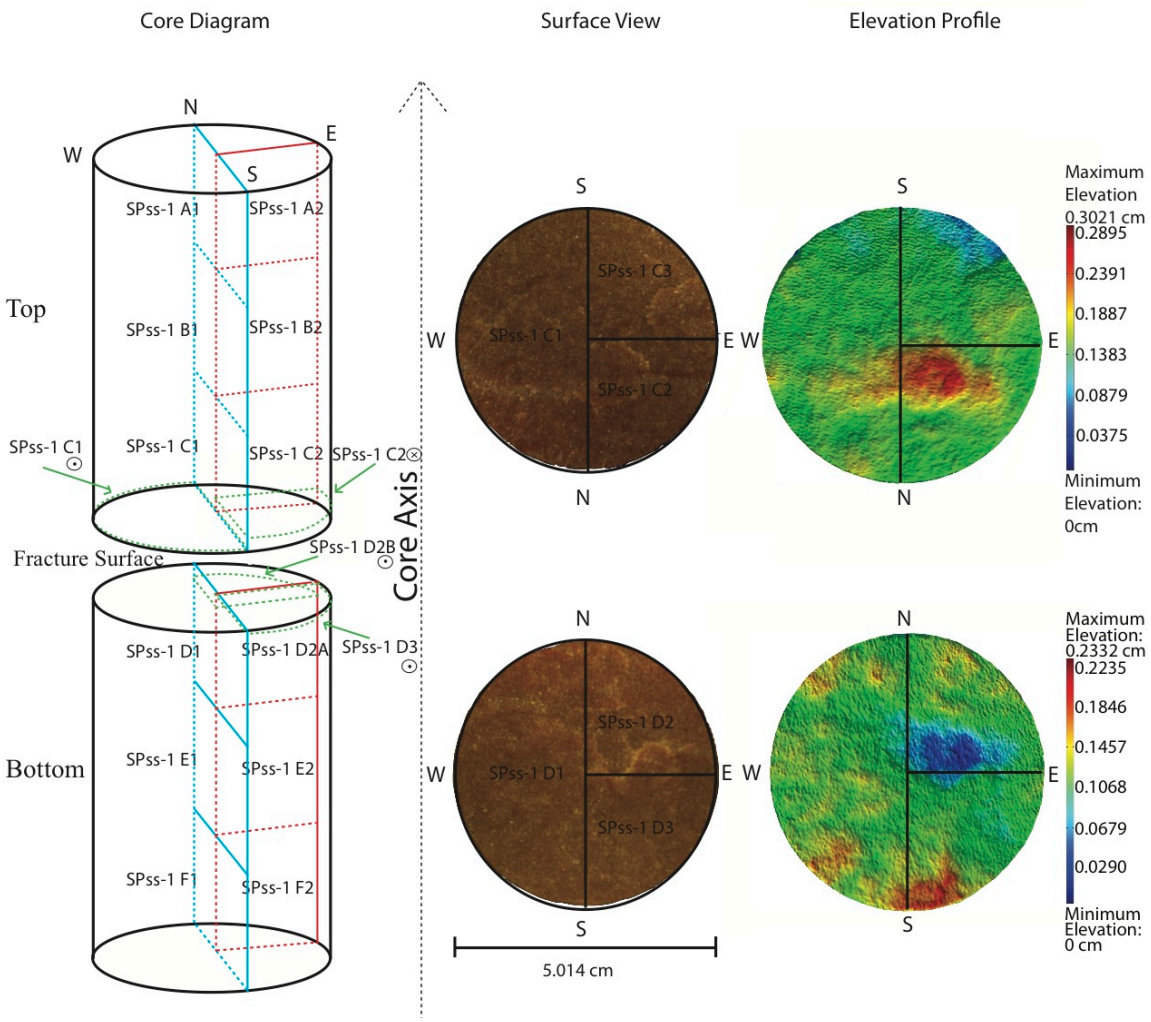

Figure 4.4. Homogeneous – Isotropic (SPss-1) core diagram. Showing orientation of thin sections, fracture surface images and fracture surface elevation profiles.

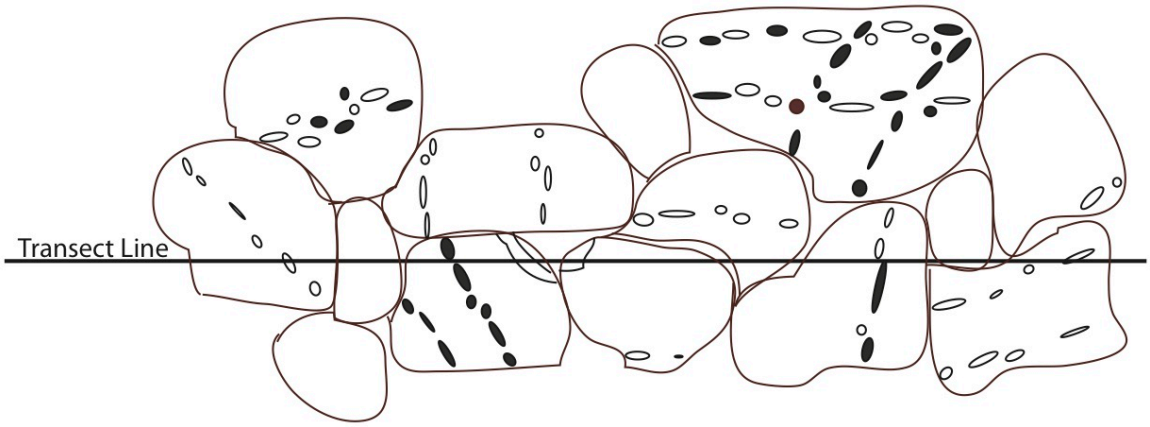

Transect Line = 1.5 X avg. grain size X # of grains [mm]
= 1.5 X 0.195 X 7
Transect Line = 2.0475

$$\text{Linear Crack Density} = \frac{\text{\# of Microfractures}}{\text{Transect Line (mm)}}$$
$$= 8/2.0457$$

Linear Crack Density = 3.907 frac/mm

Figure 4.5. Schematic demonstrating linear crack density calculation. All fractures, both open and healed, that intersect a transect line whose length is determined by the average grain size and number of grains intersected, are counted. The number of microfractures is then divided by the length of the transect line to get number of fracture per mm.

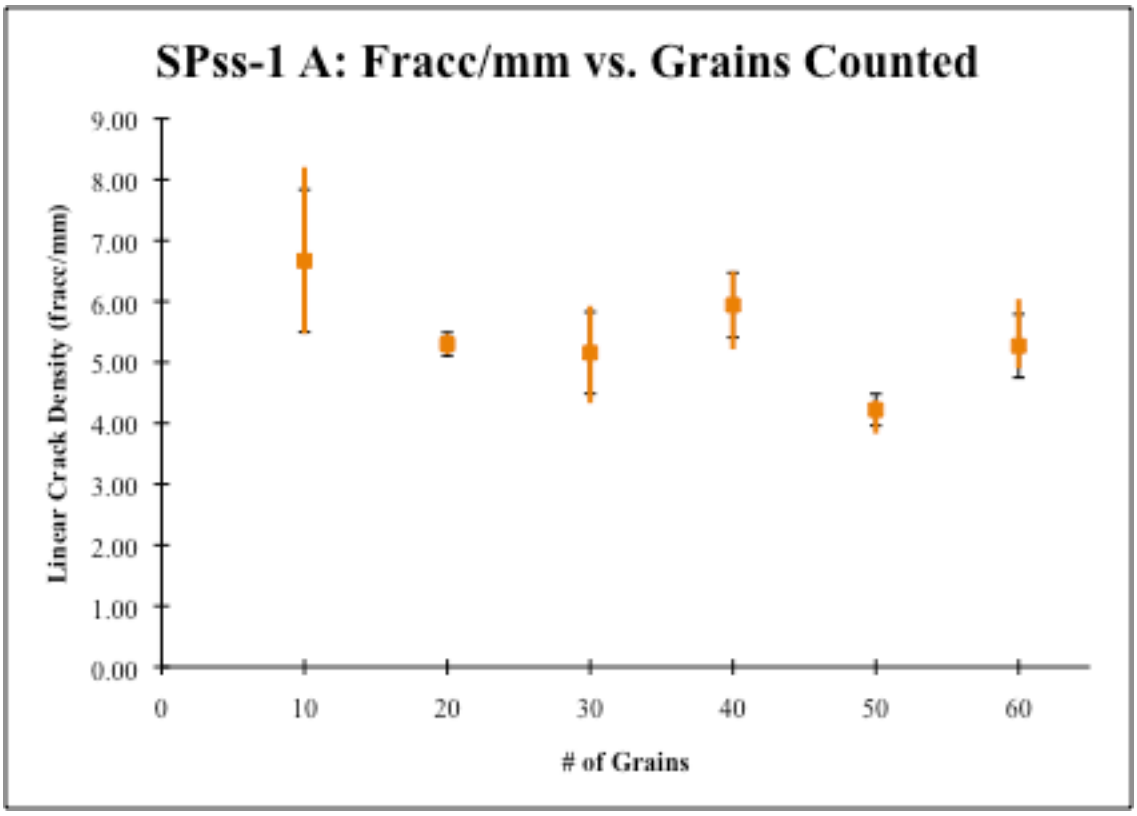

Figure 4.6. Determination of transect line length for linear crack density. Five counts were made and averaged for each transect length (# of grains). Based on reproducibility and standard deviation a 20 grain count was chosen as the transect length for all linear crack density measurements.

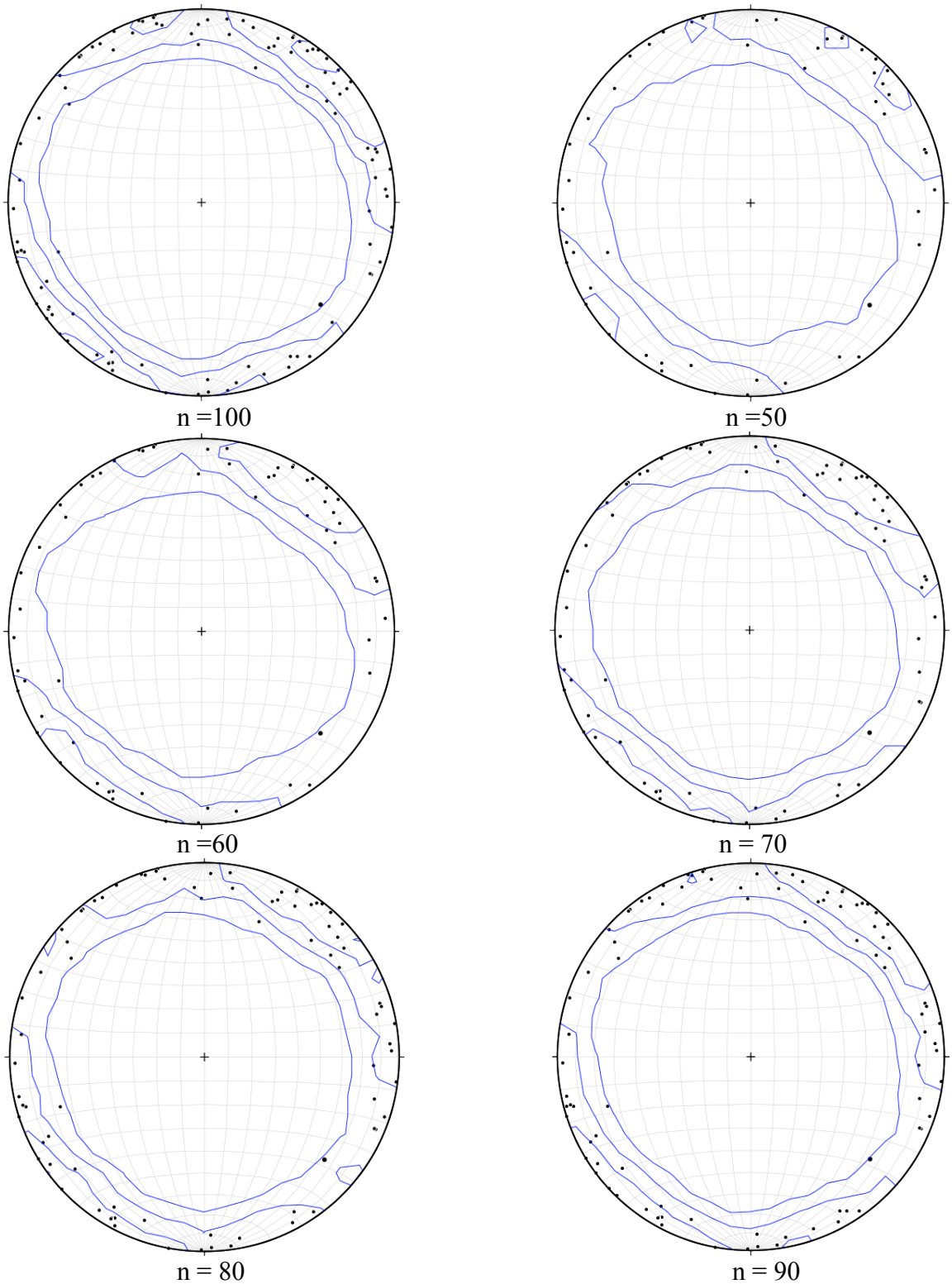

Figure 4.7. Equal area net comparison for SPss-1 C2 ||. First 100 orientations are plotted beside 50 orientations, and then orientations are increased by 10 measurements to investigate variation. The overall trend does not change very much, mainly the concentration of poles.

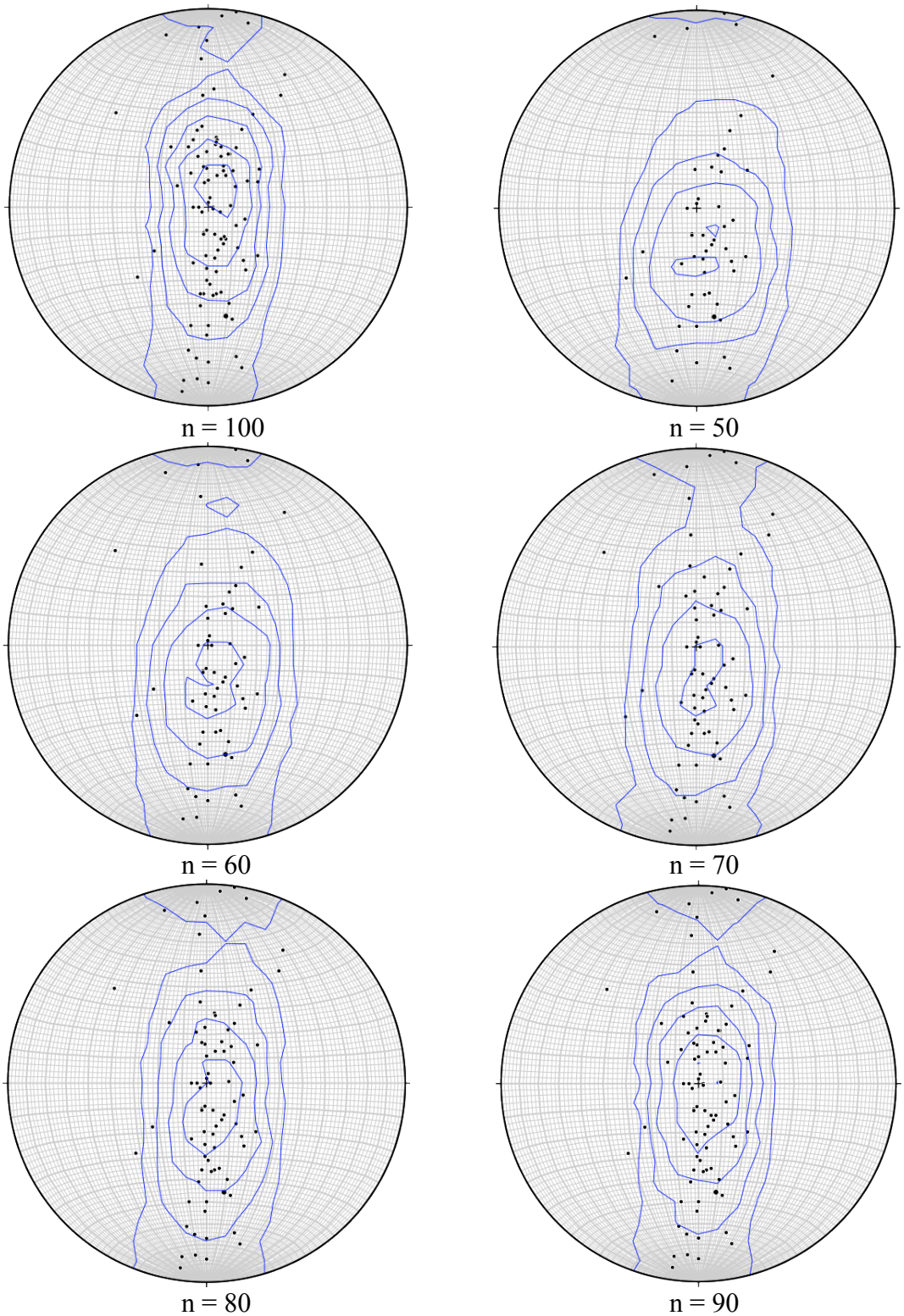

Figure 4.8. Equal area net comparison for SPss-1 C1 along NHF surface. First, 100 orientations are plotted beside 50 orientations, and then orientations are increased by 10 measurements to investigate variation. Orientations become more oblique with lower measurements.

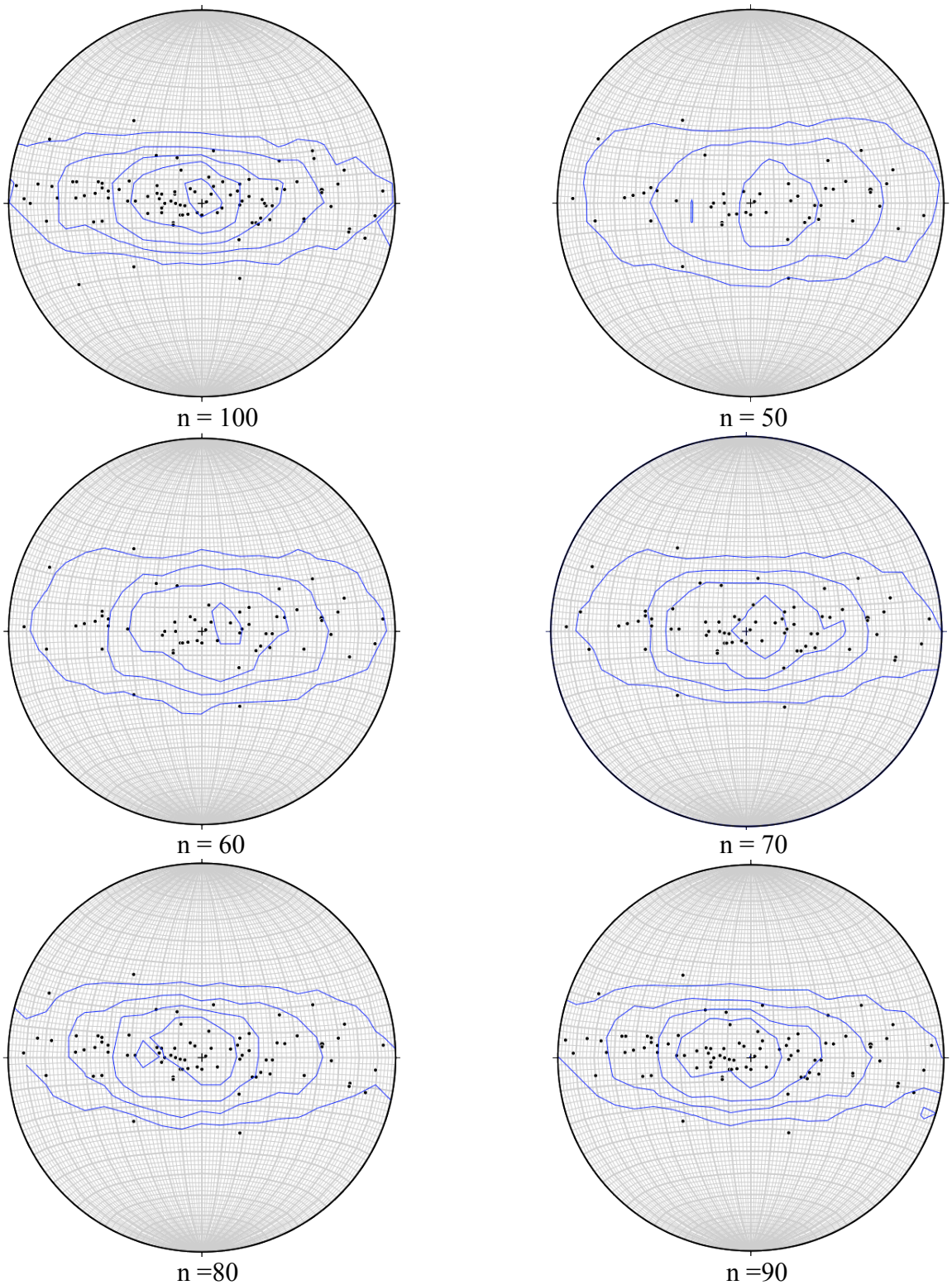

Figure 4.9. Equal area net comparison for SPss-1 C2 along NHF surface. First, 100 orientations are plotted beside 50 orientations, and then orientations are increased by 10 measurements to investigate variation. Orientations become more oblique with fewer measurements.

A.

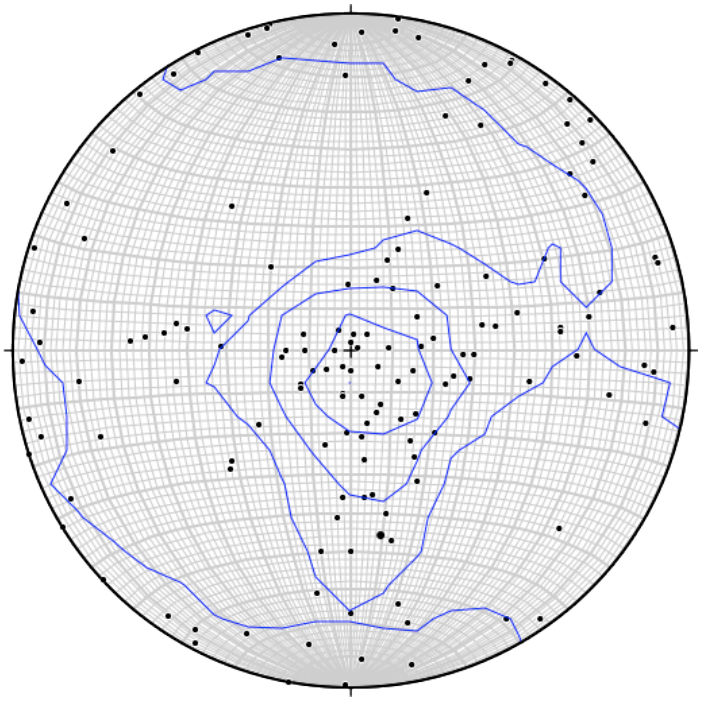

n = 150

B.

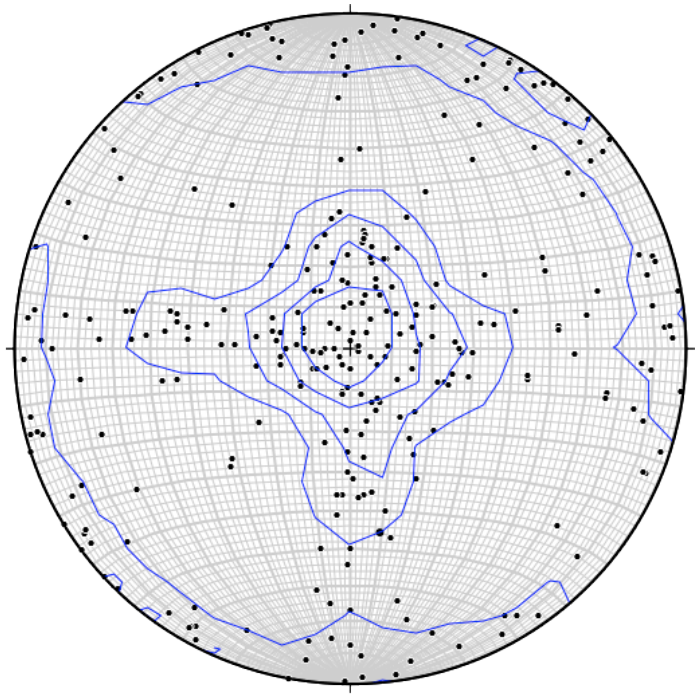

n = 301

Figure 4.10. 50 vs. 100 orientations from three mutually perpendicular thin sections. Thin sections used are SPss-1 C1 & C2 along NHF surface and SPss-1 C2 ||. A) 50 measurements. B) 100 measurements.

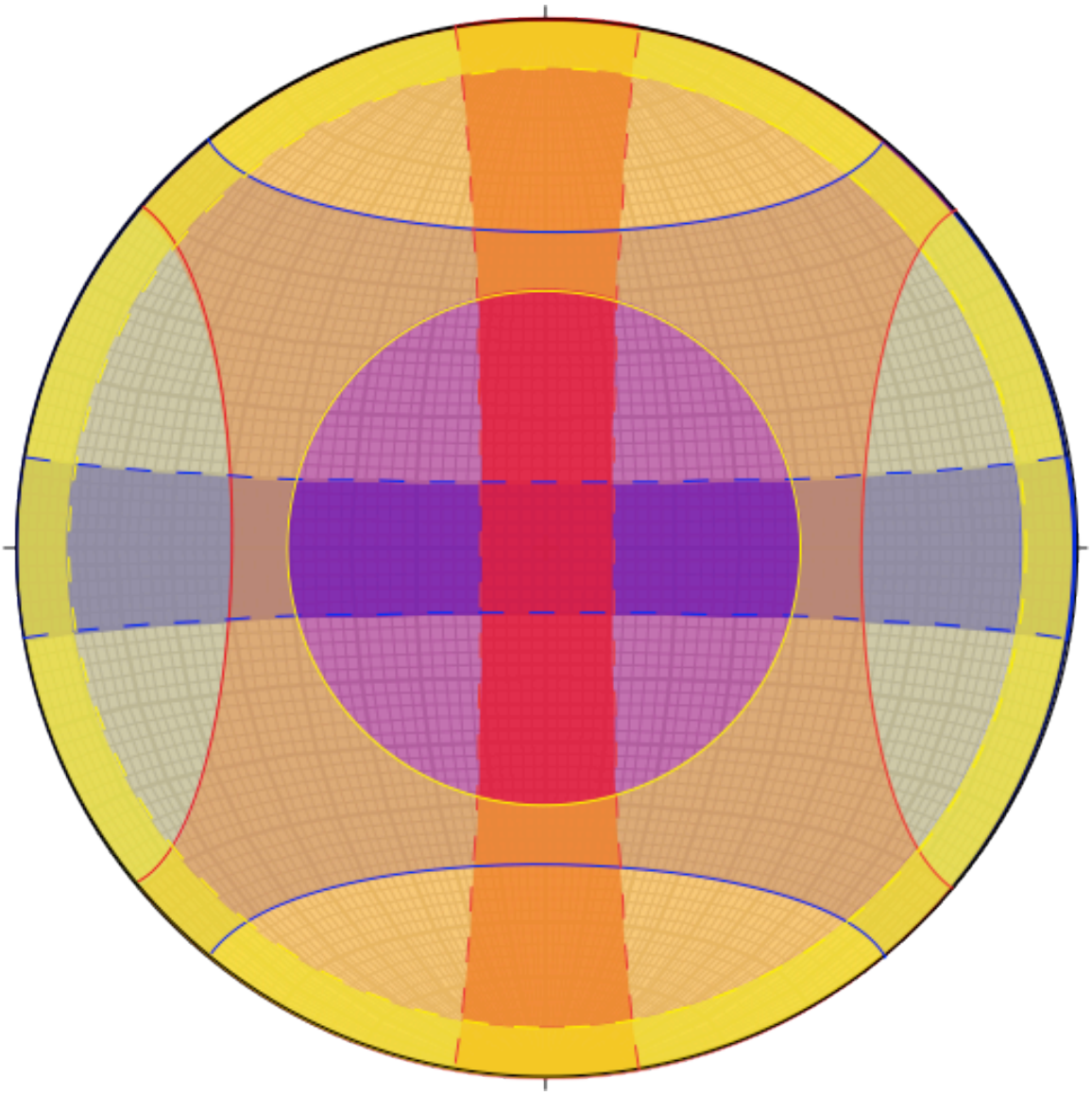

Figure 4.11. Measurable areas from three mutually perpendicular thin sections. Viewed from a Universal stage. Color show where a particular thin sections, orientation's plot: Red = N-S thin sections, Blue = E-W thin sections, Yellow = fracture plane thin sections. Solid lines are the extent of measurement for a particular thin section and dashed lines are the areas where orientations are most easily seen. The square around the center of the equal area net is where triple sampling occurs, when all three colors overlap.

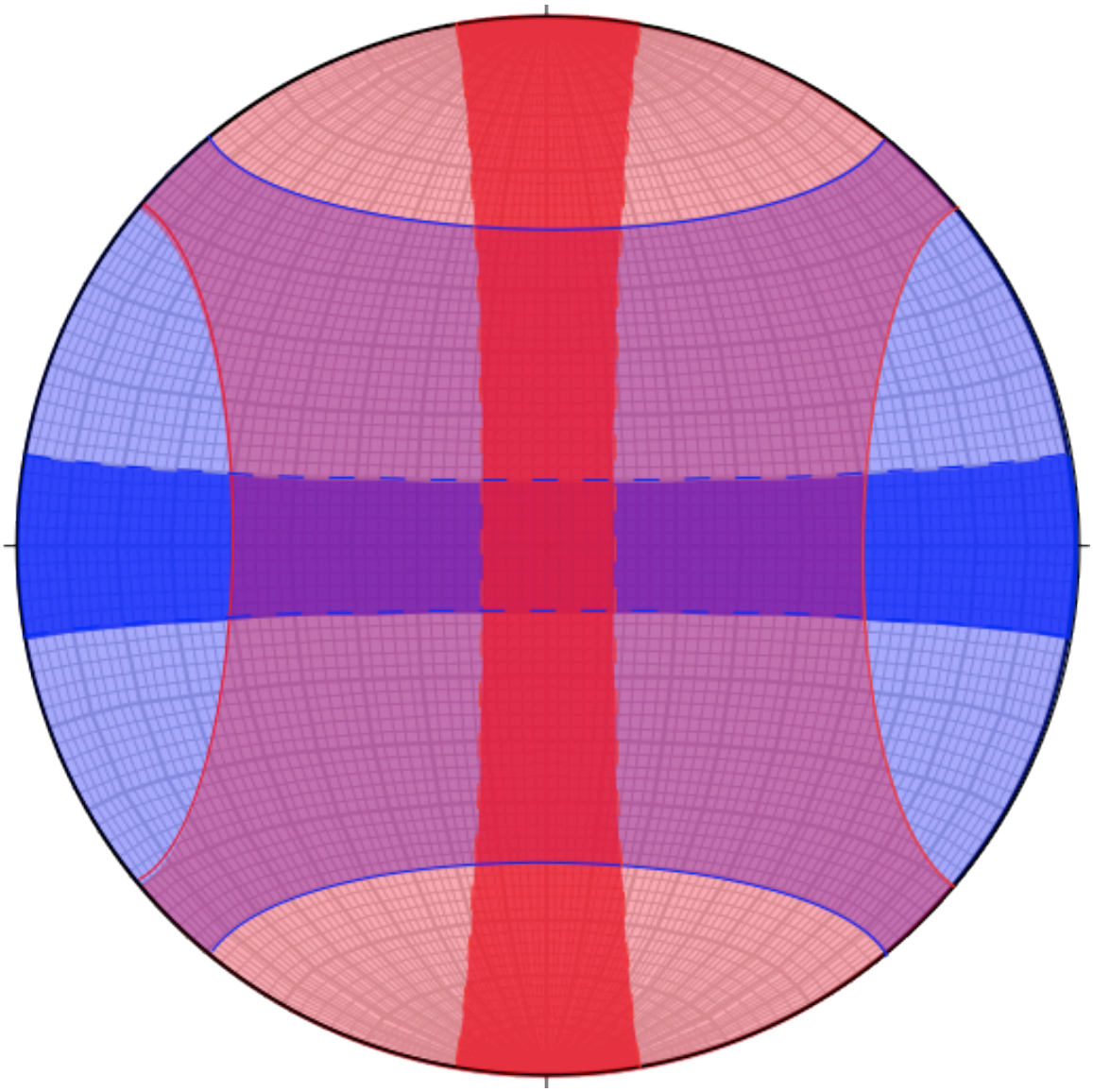

Figure 4.12. Measurable areas from two mutually perpendicular thin sections. Viewed from a Universal Stage. Color show where a particular thin sections, orientation's plot: Red = N-S thin sections, Blue = E-W thin sections. Solid lines are the extent of measurement for a particular thin section and dashed lines are the areas where orientations are most easily seen. Double sampling occurs inside the square in the middle of the equal area net.

Statistic: Sample ID:	Total Elevation (cm)	Mean Elevation (cm)	Standard Deviation (cm)	Total Data Points
Abo Fm. Top	0.6044	0.3525	0.1452	99594
Abo Fm. Bottom	0.5493	0.2344	0.1374	109732
SPss-1 Top	0.2644	0.1381	0.0418	157760
SPss-1 Bottom	0.2332	0.132	0.0388	165785
SPss-2 Top	0.3169	0.1374	0.0558	204367
SPss-2 Bottom	0.3054	0.1897	0.0641	147091

Table 5.1. NHF surface elevation statistics. Values are for each side of the fracture, showing total and mean elevations, standard deviations and total data points collected. Data obtained using 3D NextEngine Scanner.

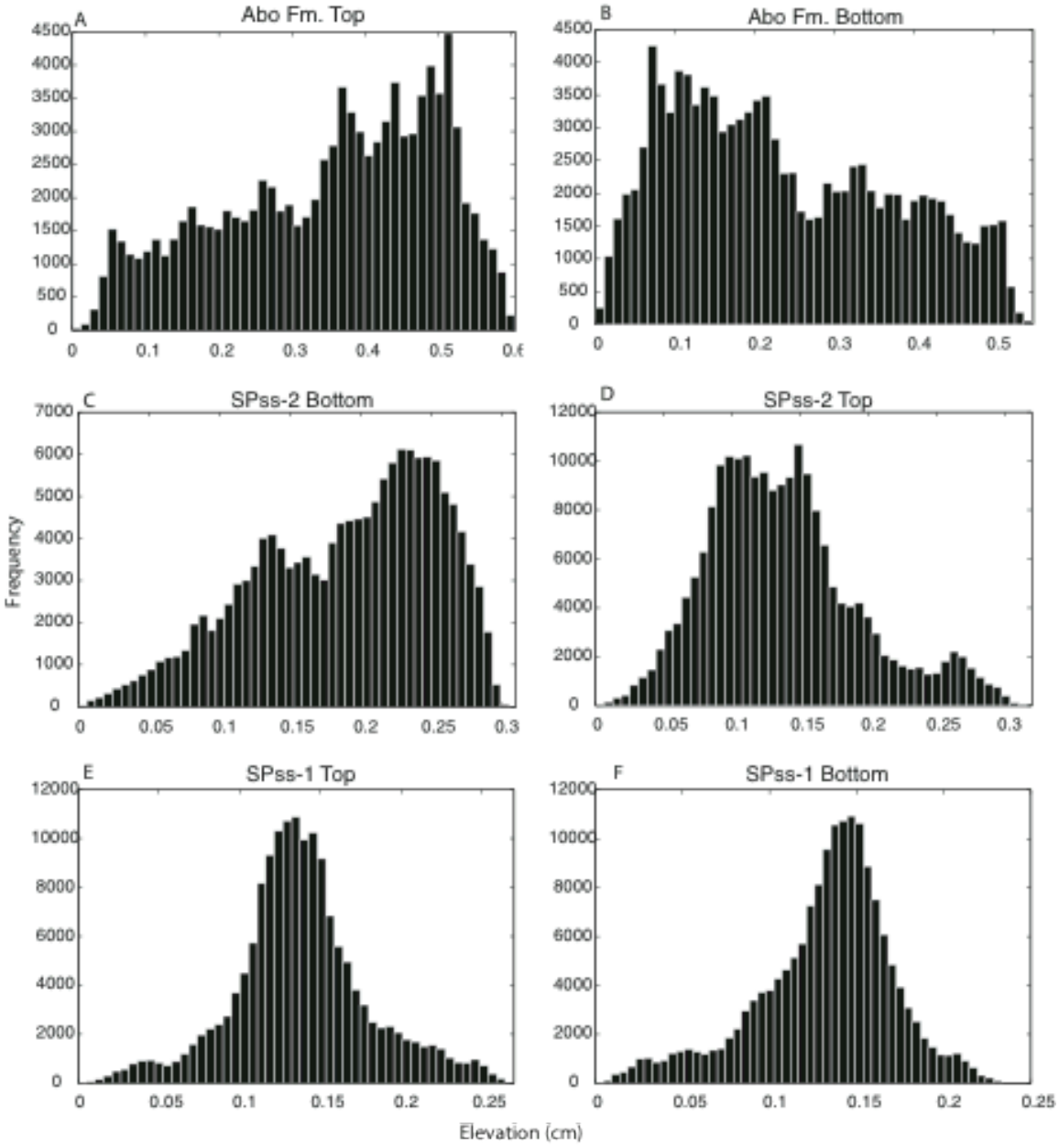

Figure 5.1. Surface elevation histograms. Both sides of all three NHFs. A) Abo top surface. B) Abo bottom surface. C) SPss-2 bottom surface. D) SPss-2 top surface. E) SPss-1 top surface. F) SPss-1 bottom surface.

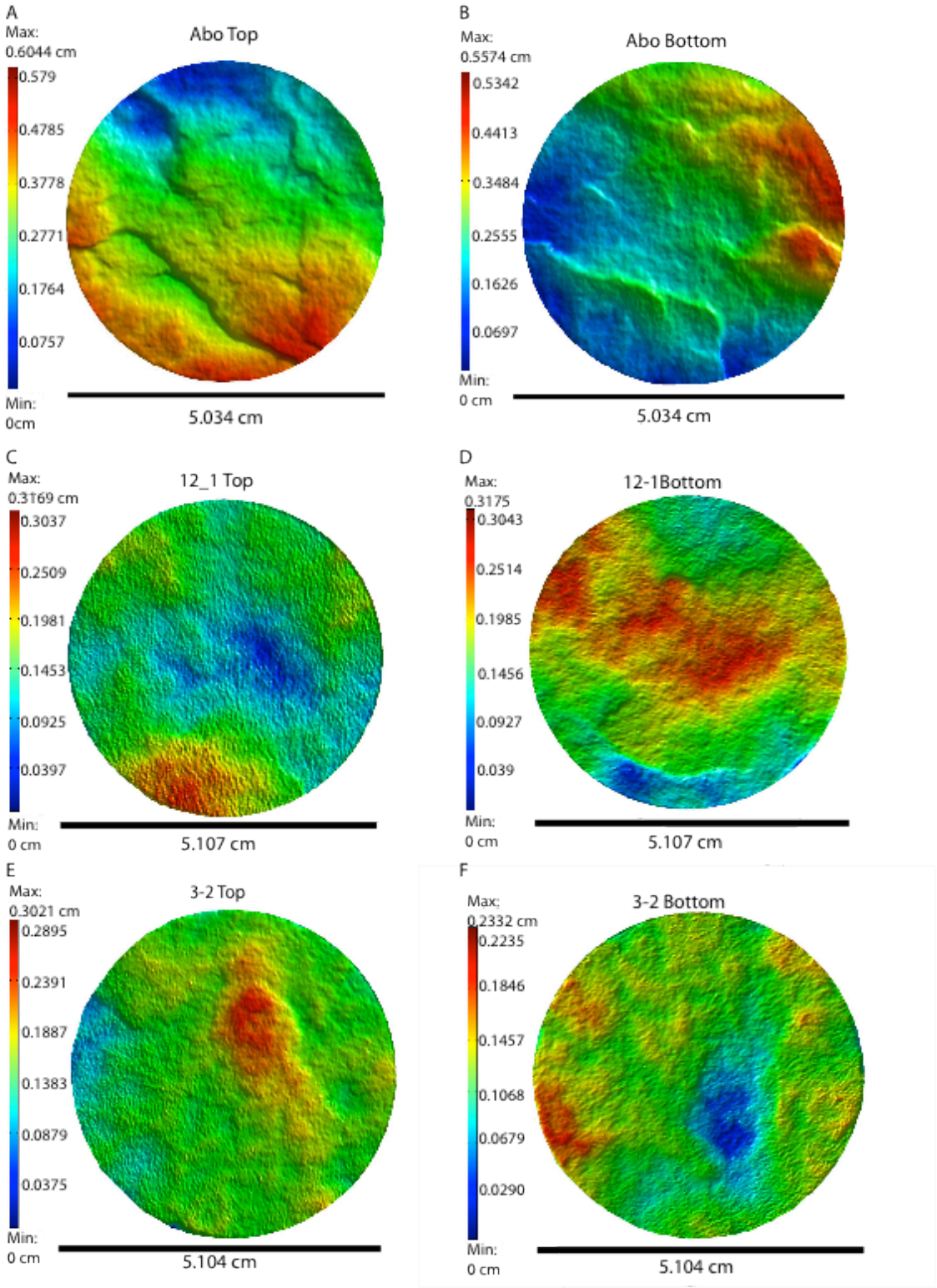

Figure 5.2. Surface elevation maps. Each fracture surface from both sides of each NHFs (also pictured in core diagrams for each corresponding rock). A) Abo top surface. B) Abo bottom surface. C) SPss-2 top surface. D) SPss-2 bottom surface. E) SPss-1 top surface. F) SPss-1 bottom surface.

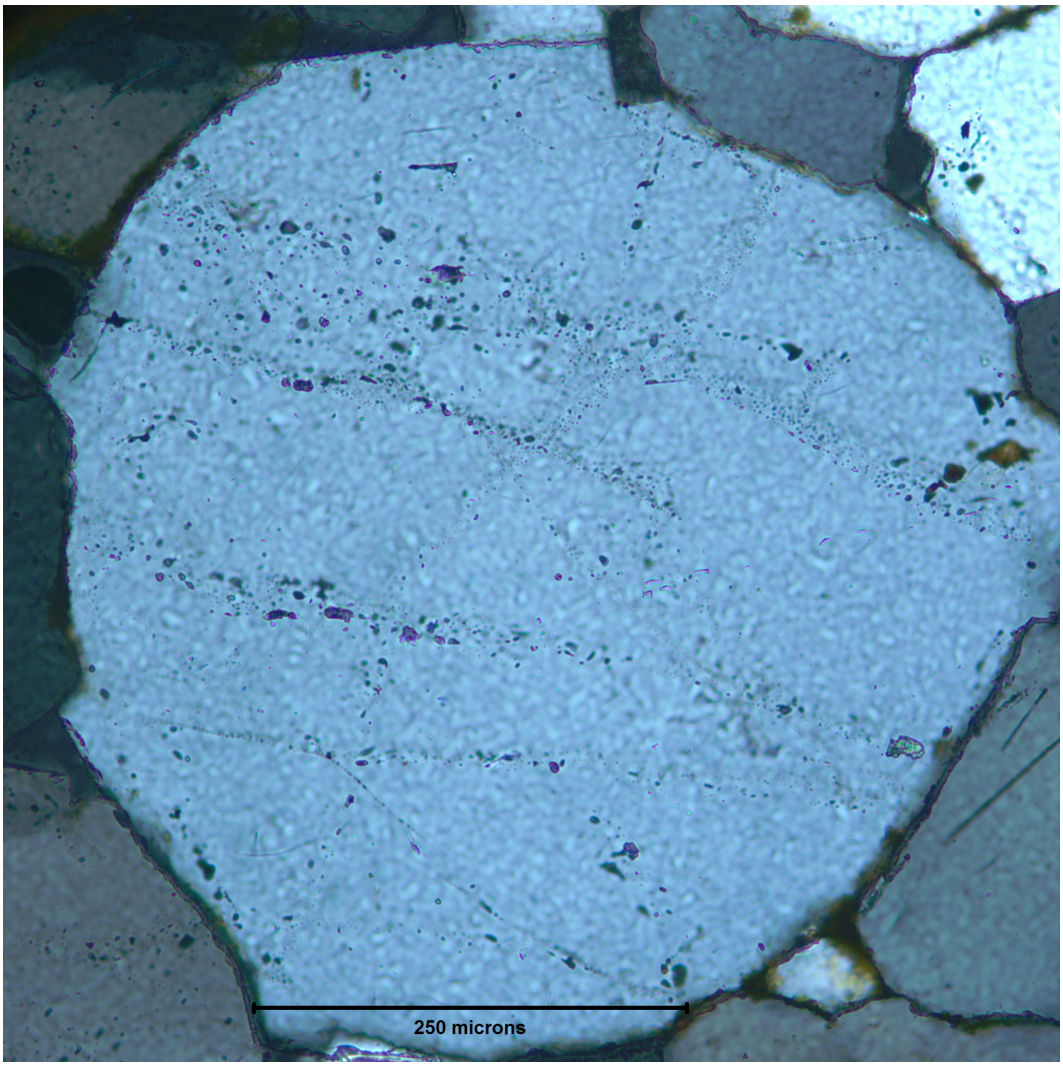

Figure 5.3. Example of fluid inclusion planes from SPss-1 A.

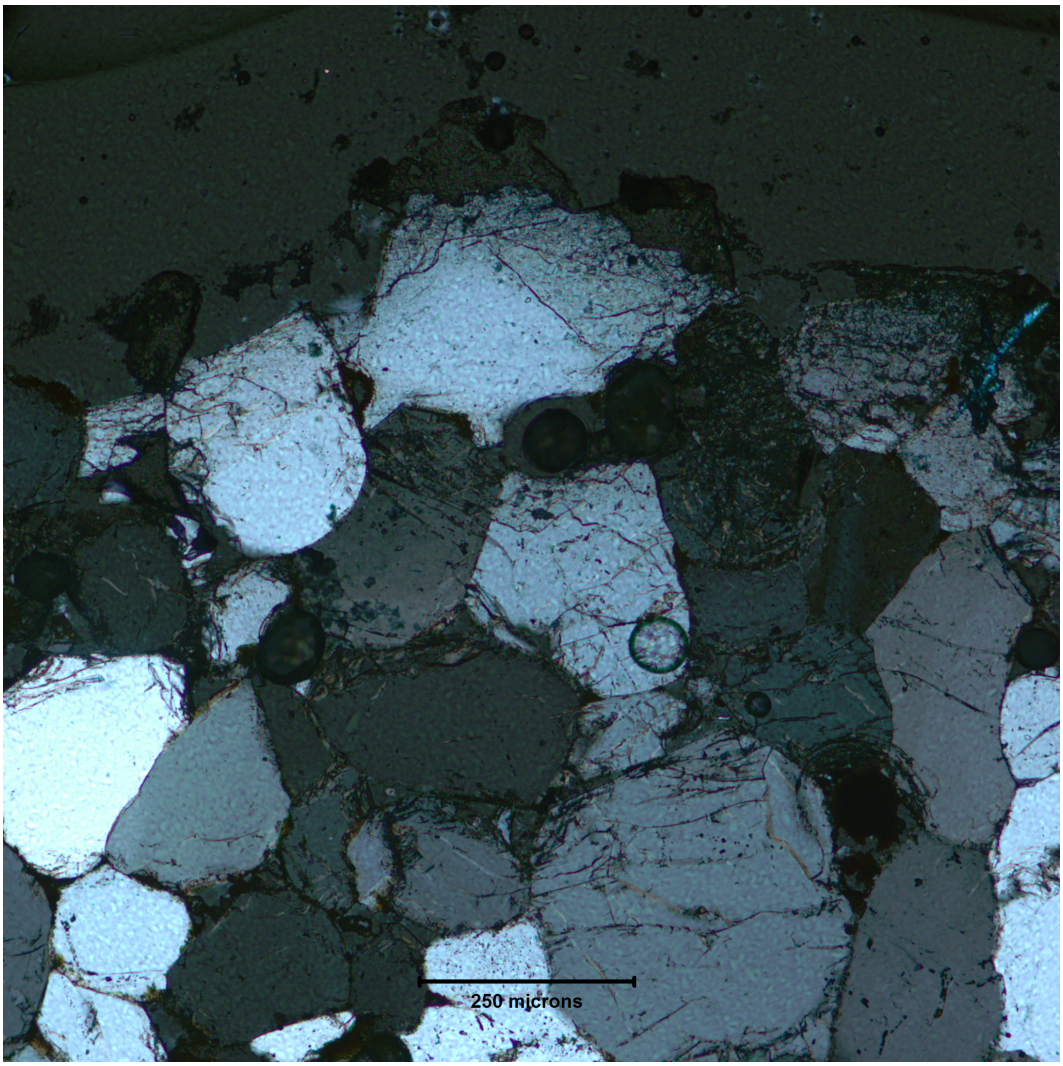

Figure 5.4. Open microfractures along NHF surface. Formed during NHF experiments in SPss-1 C1.

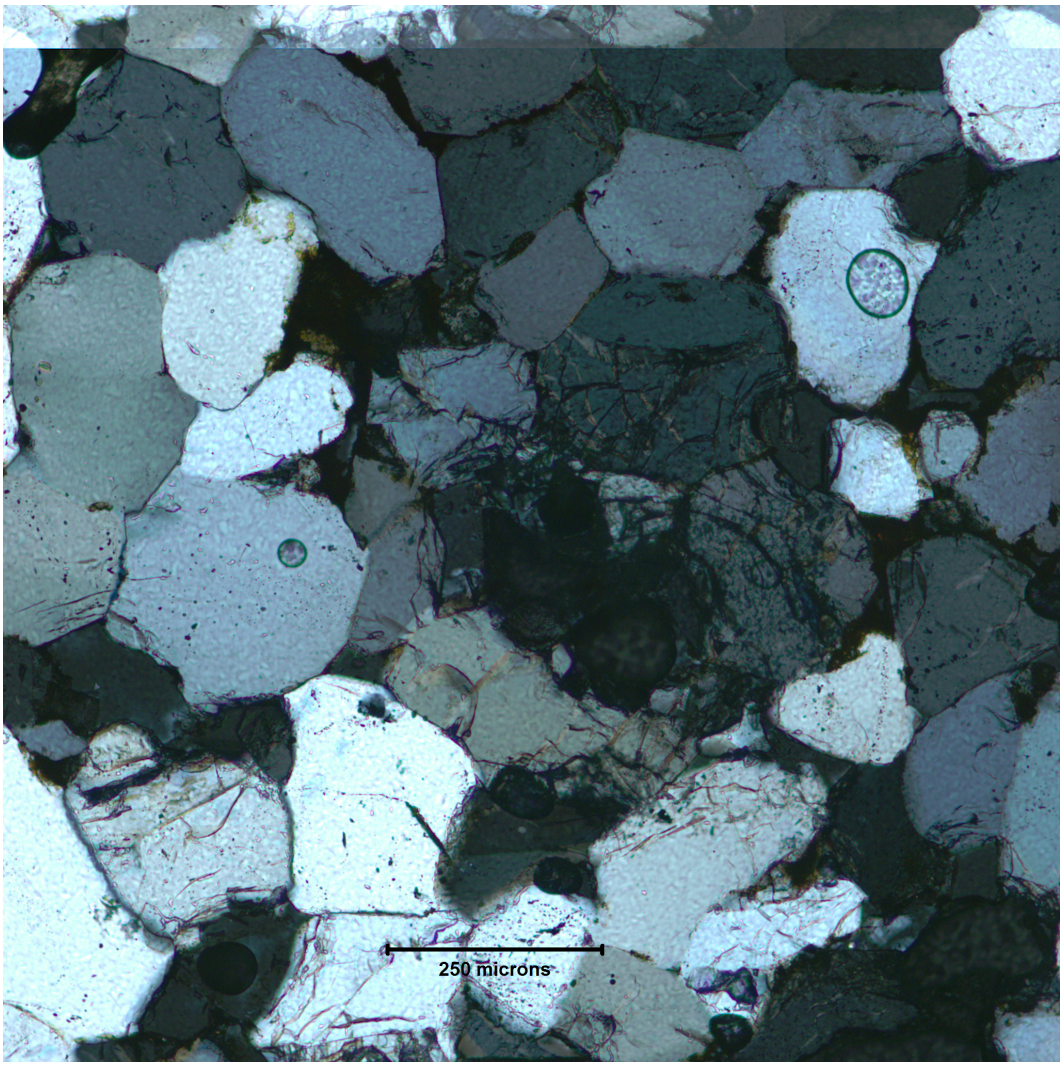

Figure 5.5 Pore space with microfractures, SPss-1 C1.

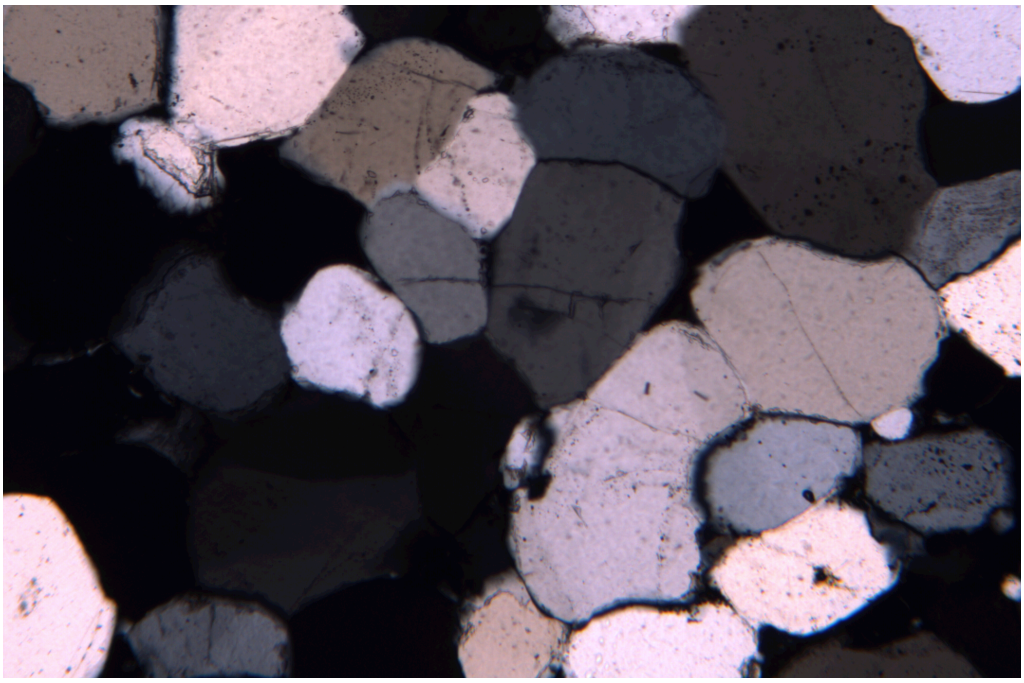

Figure 5.6. Open microfractures, SPss-2 B2. Showing grain boundary, intragranular, intergranular and transgranular cracks.

A.

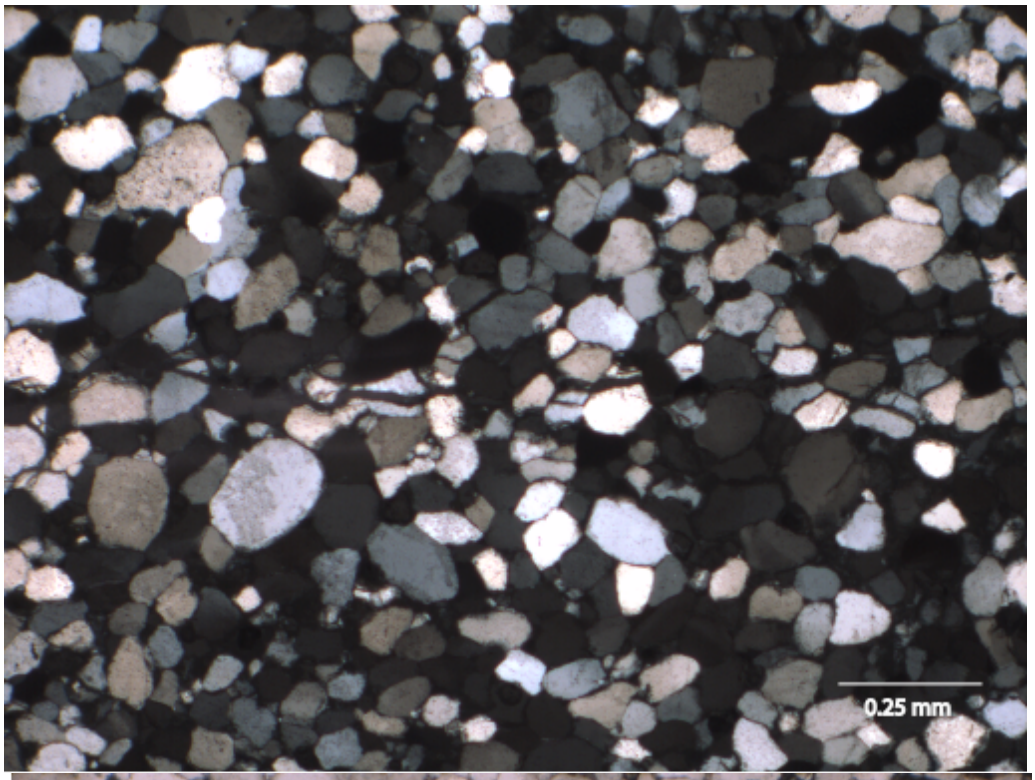

B.

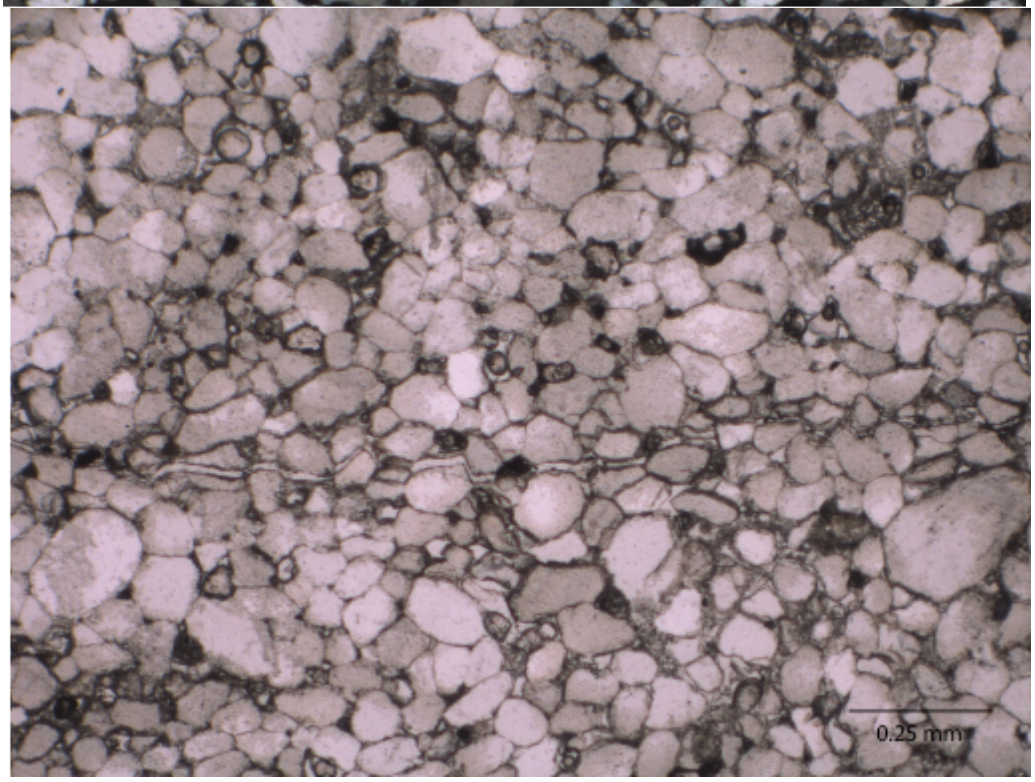

Figure 5.7. Non-through-going fracture from SPss-2 TB1. A) Fracture under polarized light. B) Fracture under plain light.

A.

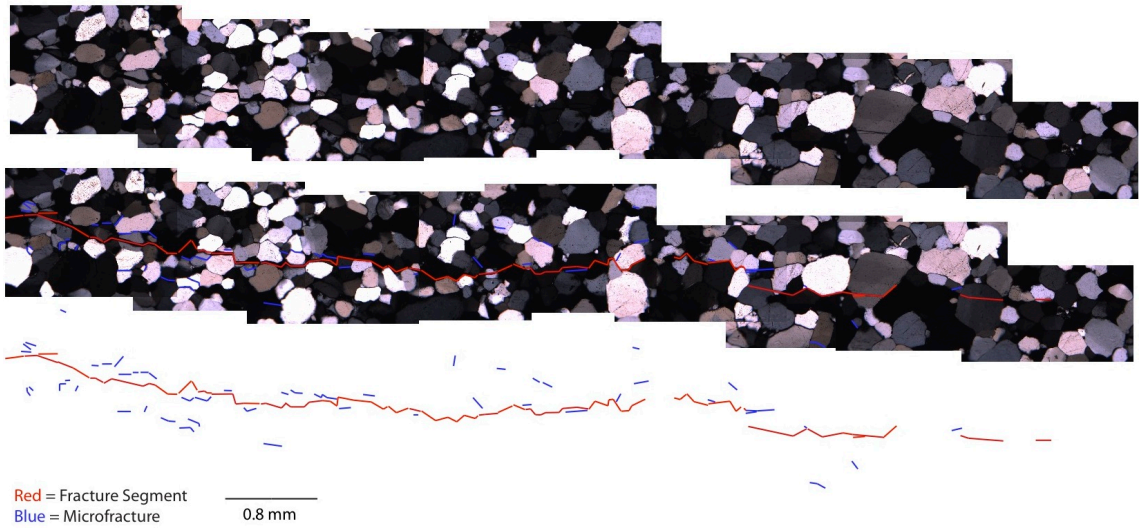

B.

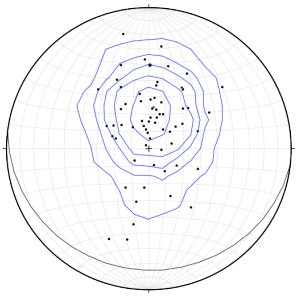

n = 67

D.

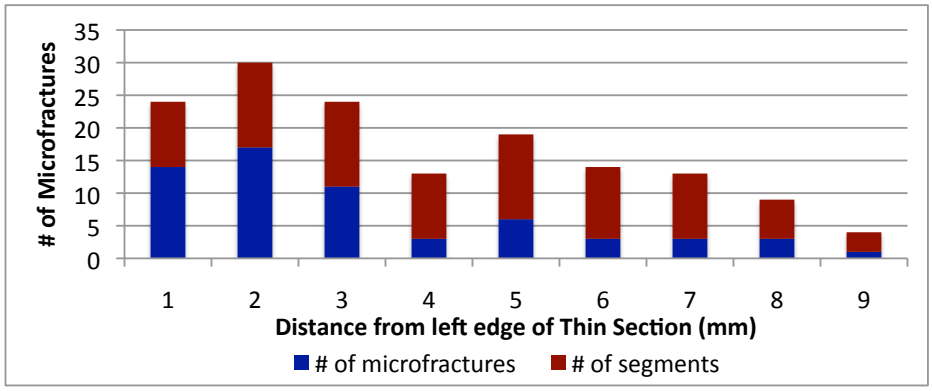

Figure 5.8. Terminating non-through going fracture, Spss-2 TB1. A) From top to bottom: polarized image of fracture, polarized image with the fracture traced in red and microfractures in blue, and map of the fracture and damage zone. B) Orientations of fracture segments shown in red on maps, as viewed parallel to core axis, plotted on lower hemisphere equal area projection, with Kamb contours at 3.0 confidence intervals. Mean orientation of segment plotted as a great circle, 97, 15° S. Note that damage zone development generally increases with degree of connection between fracture segments. There were too few damage zone microfractures to plot. D) Histogram of microfractures with distance from left edge of the thin section.

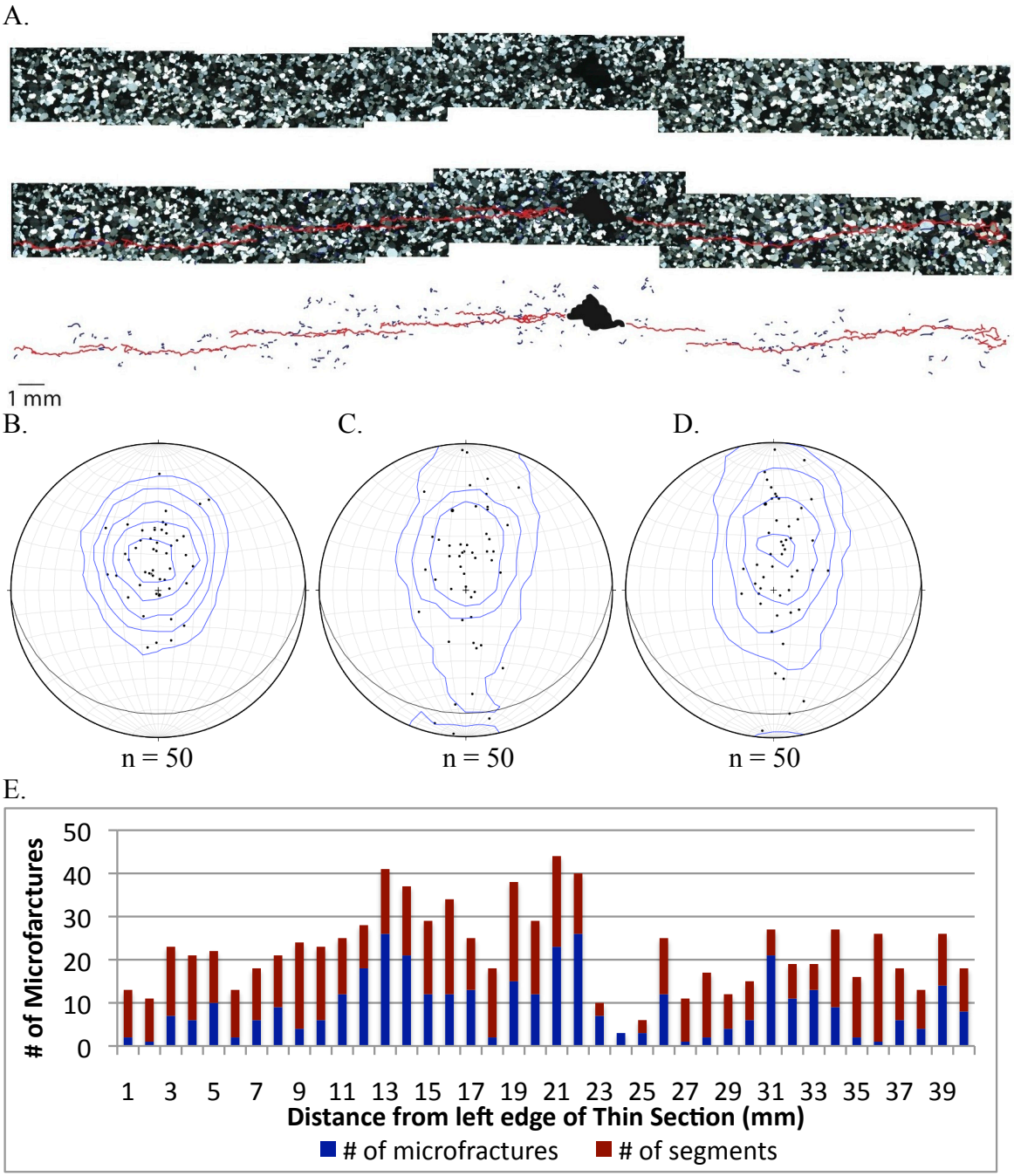

Figure 5.9. Discontinuous non-through-going fracture, Spss-2 TB1. A) From top to bottom: polarized image of fracture, polarized image with the fracture traced in red, microfractures in blue and areas of grain plucking in black and map of the fracture and damage zone. Data collected from a discontinuous non-through-going fracture trace. Note en échelon nature of disconnected fracture segments and variable development of damage zone. B-D) are lower hemisphere, equal area net projections, with Kamb contours at 3.0 confidence intervals, of the fracture segments (B) and microfractures above (C) and below (D) the fracture. Mean orientation of segment is plotted as a great circle, 87, 17° S. E) Histogram of microfractures with distance from left edge of the thin section.

A.

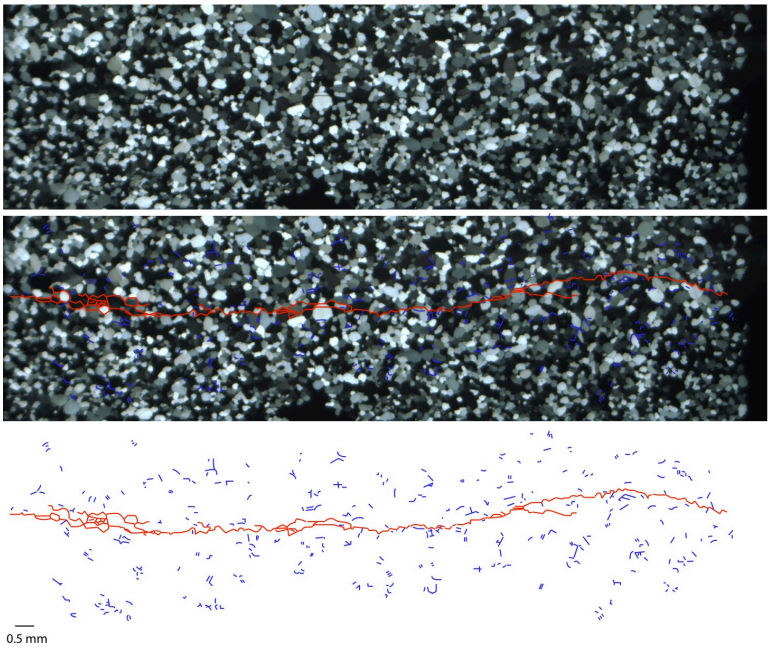

B. C. D.

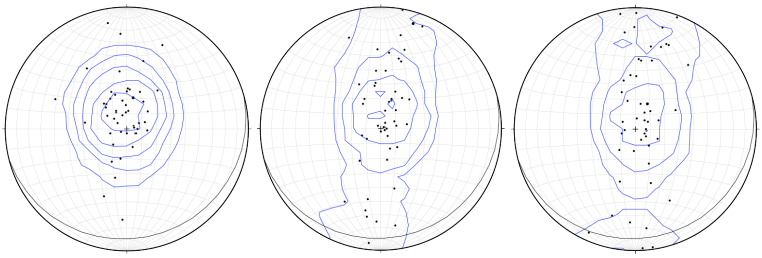

n = 50 n = 51 n = 50

E.

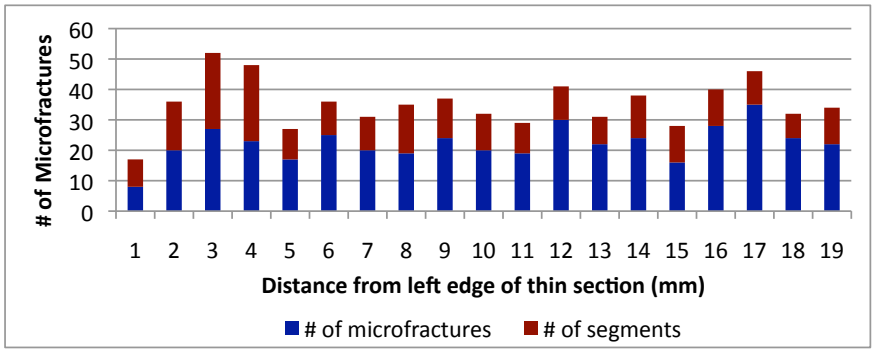

Figure 5.10. Continuous non-through-going fracture, Spss-2 TB2. A) From top to bottom: polarized image of fracture, fracture traced in red and microfractures in blue, and map of the fracture and damage zone. Note fracture roughness, local fracture-bound lenses, and well developed damage zone. B-D) Equal area net projections, with Kamb contours at 3.0 confidence intervals, of the fracture segments (B) microfractures above (C) and below (D) the fracture. Mean orientation of segment is plotted as a great circle, 75, 11° S. E) Histogram of microfractures with distance from left edge of the thin section.

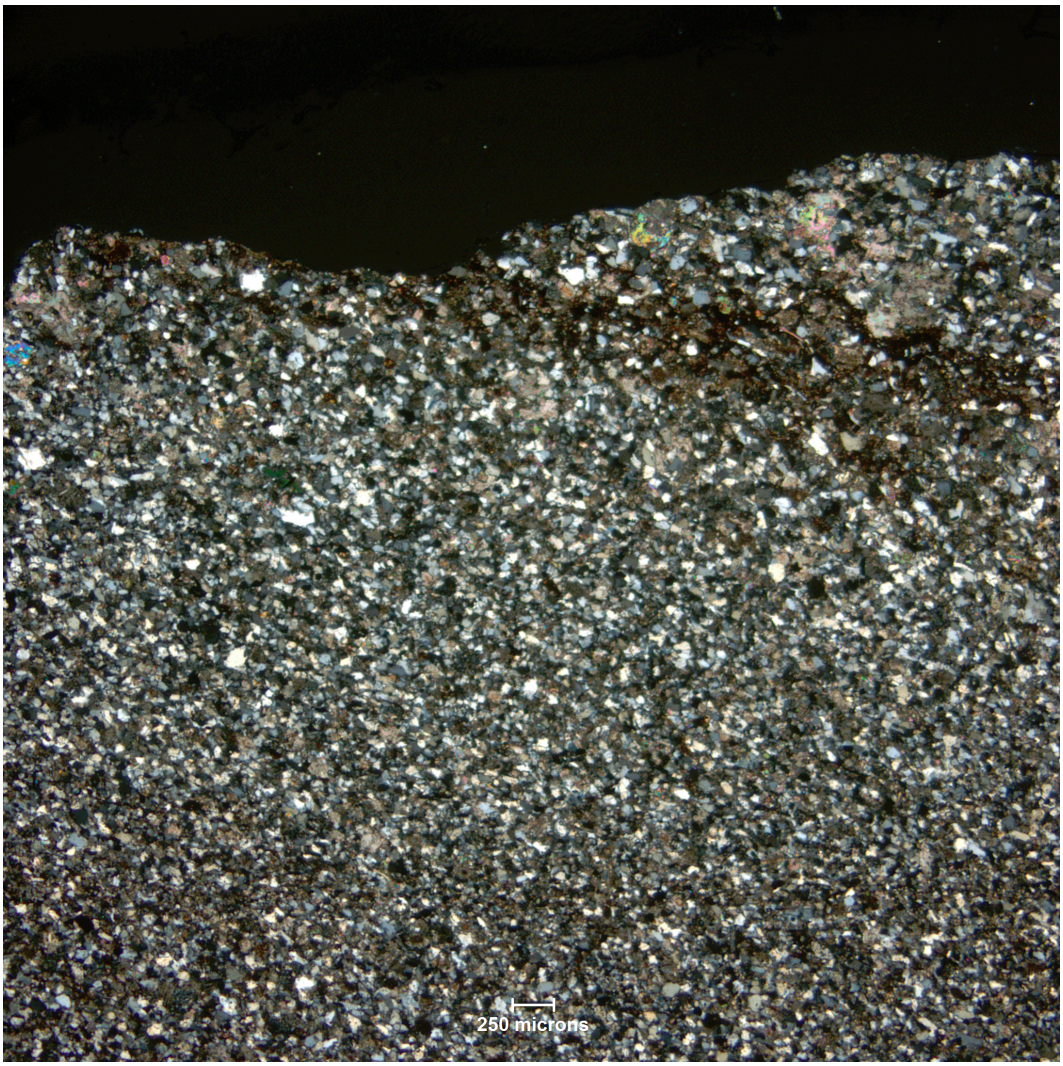

Figure 5.11. Crossbed intersecting NHF (Abo Fm. C1).

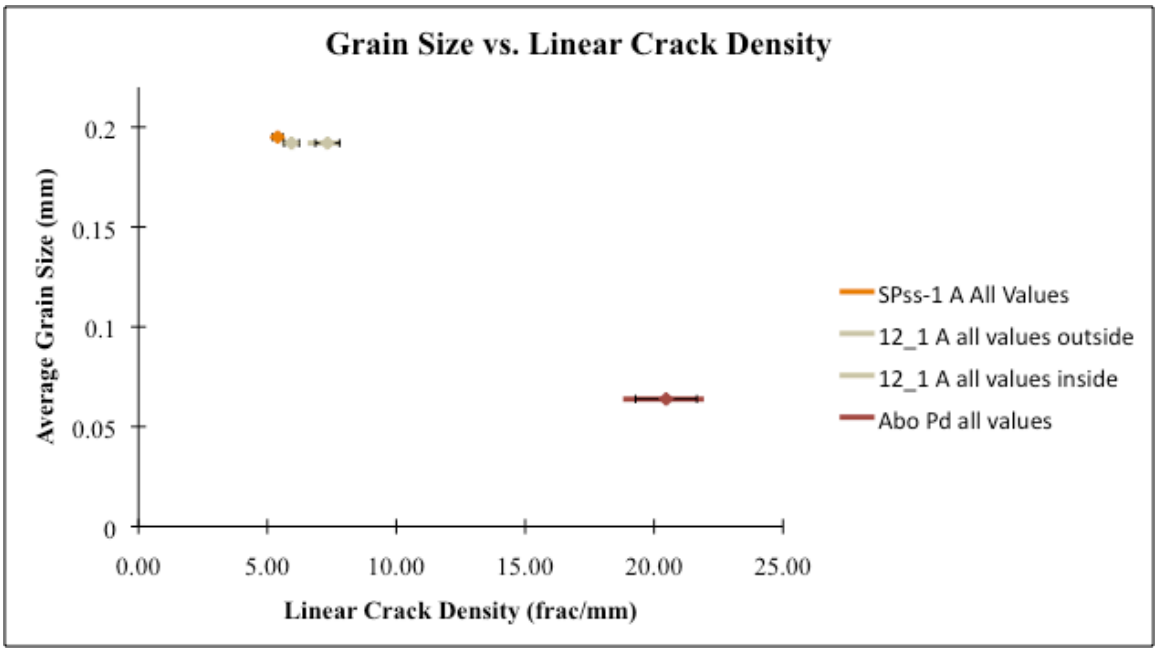

Figure 5.12. Background linear crack density. Collected from undamaged thin sections.

Thin Section ID:	SPss-1 ⇧ A	SPss-2 ⇧ A	SPss-2 ⇧ A	Abo Fm. 2 Pd
		outside concretions	in concretions	
Average Grain size (mm)	0.195	0.192	0.192	0.0564
Average Linear Crack Density (frac/mm)	5.4	5.94	7.33	23.17
Standard Deviation	0.19	0.29	0.47	1.35
Fracture Spacing (mm)	0.185	0.168	0.136	0.043
Quartz Total %	91.2	89.5	86.9	70.6
Porosity %	8.6	8.8	5	6

Table 5.2. Background linear crack density for undamaged thin sections

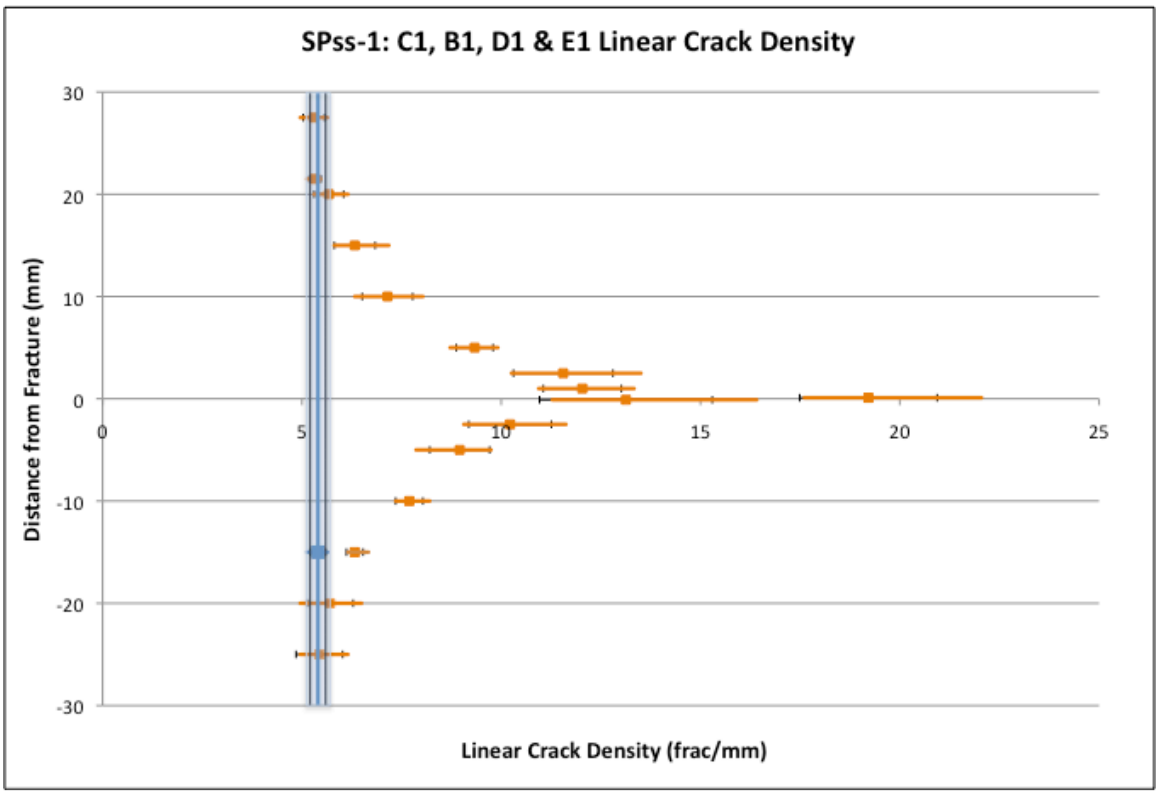

Figure 5.13. Homogenous – Isotropic Spss-1 linear crack density. NHF is at zero, blue band shows background linear crack density. Each value represents the average linear crack density at that distance and is accompanied by the span of linear crack densities and the average's error bar.

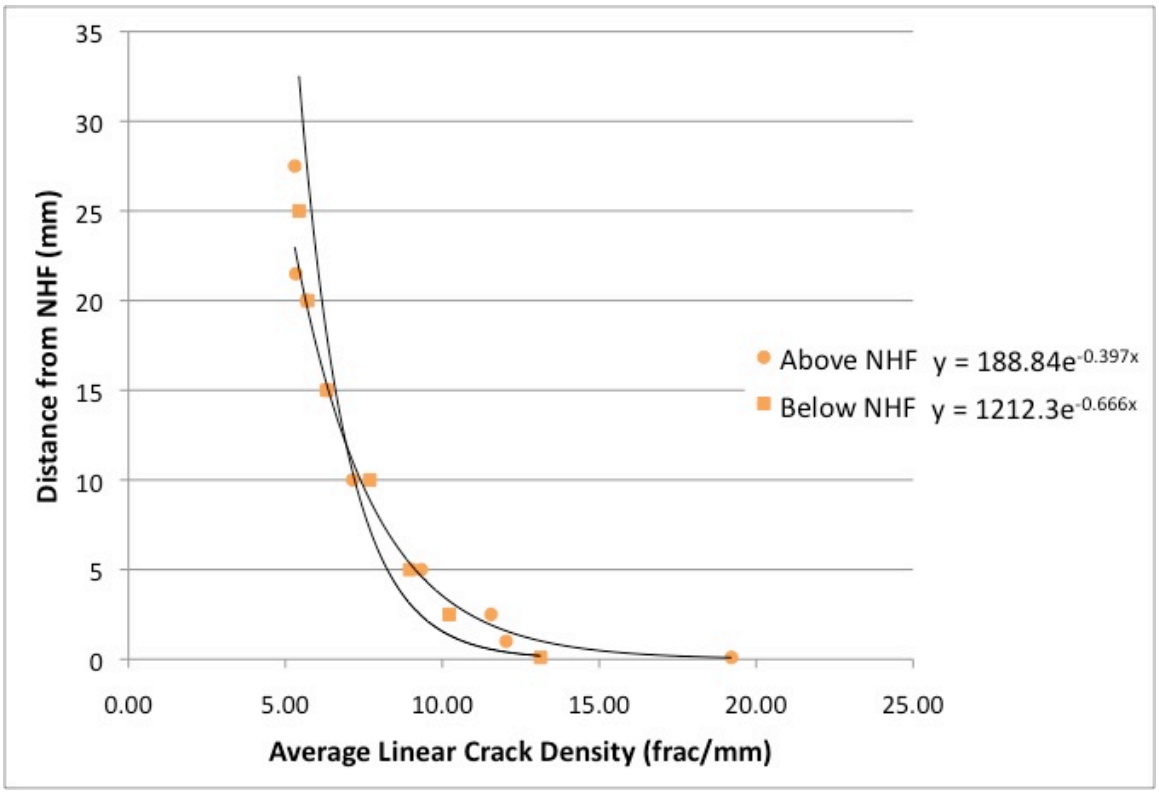

Figure 5.14. Average linear crack density for SPss-1, with exponential fit.

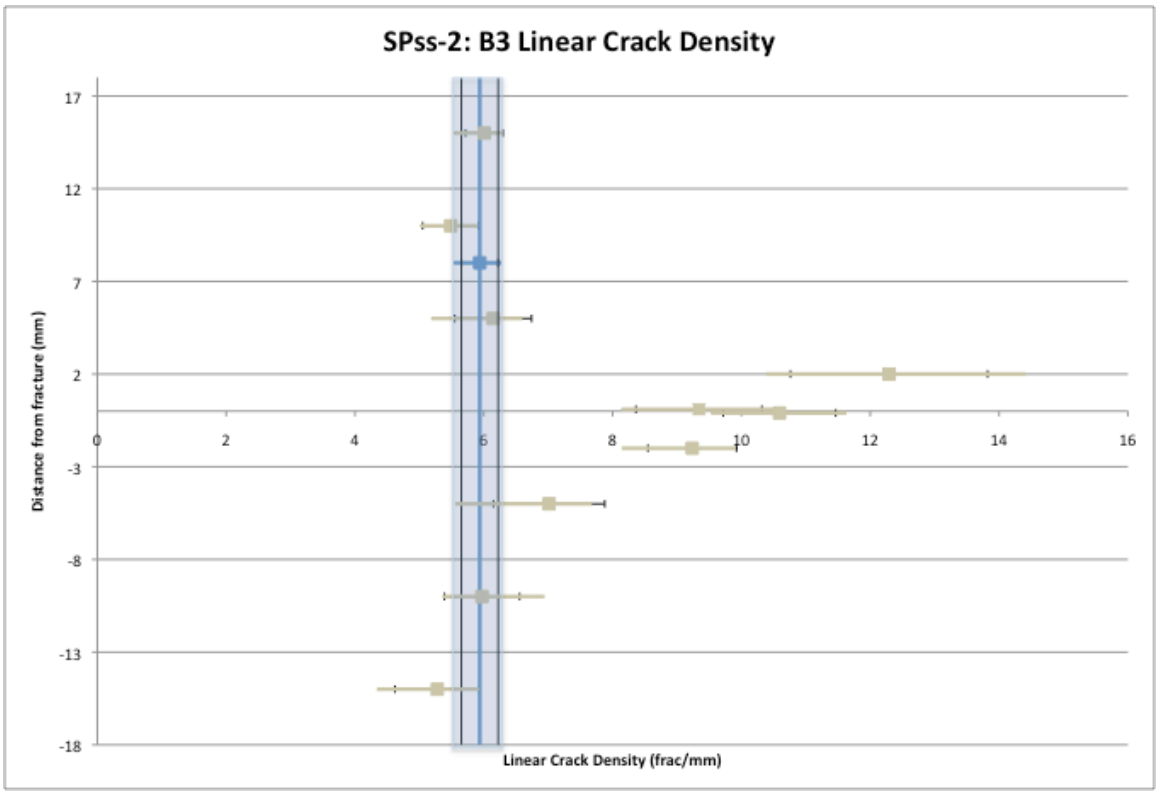

Figure 5.15. Heterogeneous – Isotropic SPss-2 linear crack density. NHF is at zero, blue band shows background linear crack density. Each value represents the average linear crack density at that distance and is accompanied by the span of linear crack densities and the average's error bar.

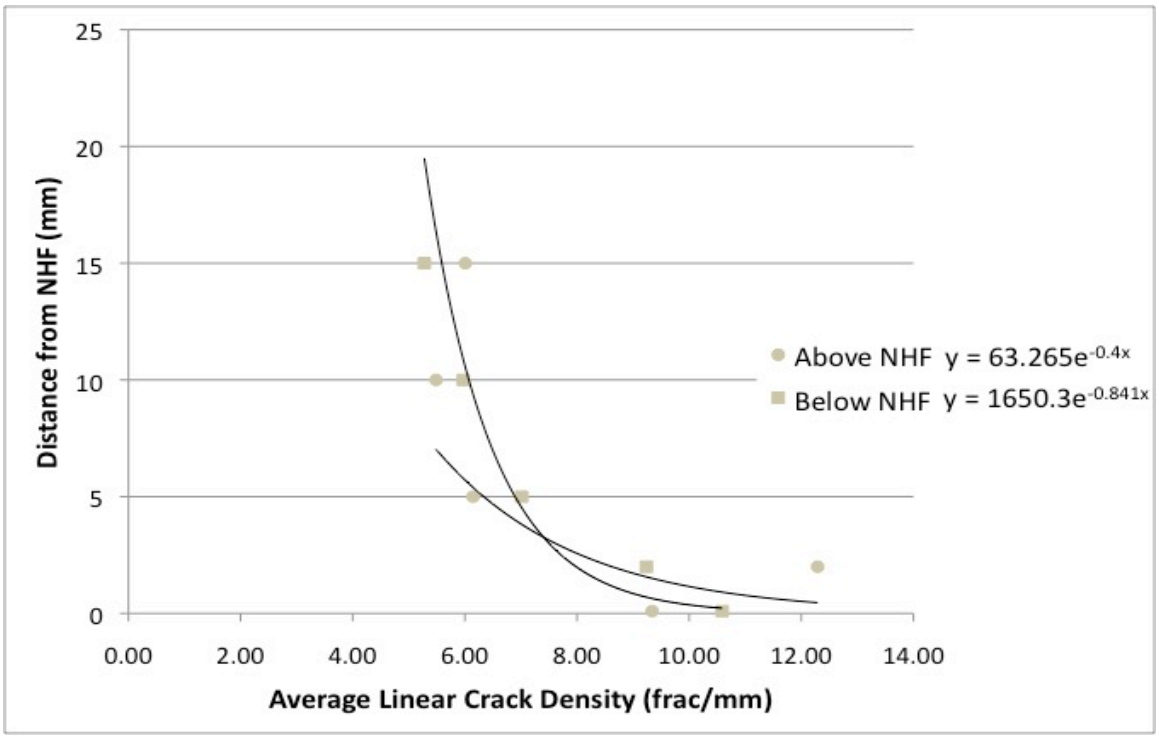

Figure 5.16. Average linear crack density for SPss-2, with exponential fit.

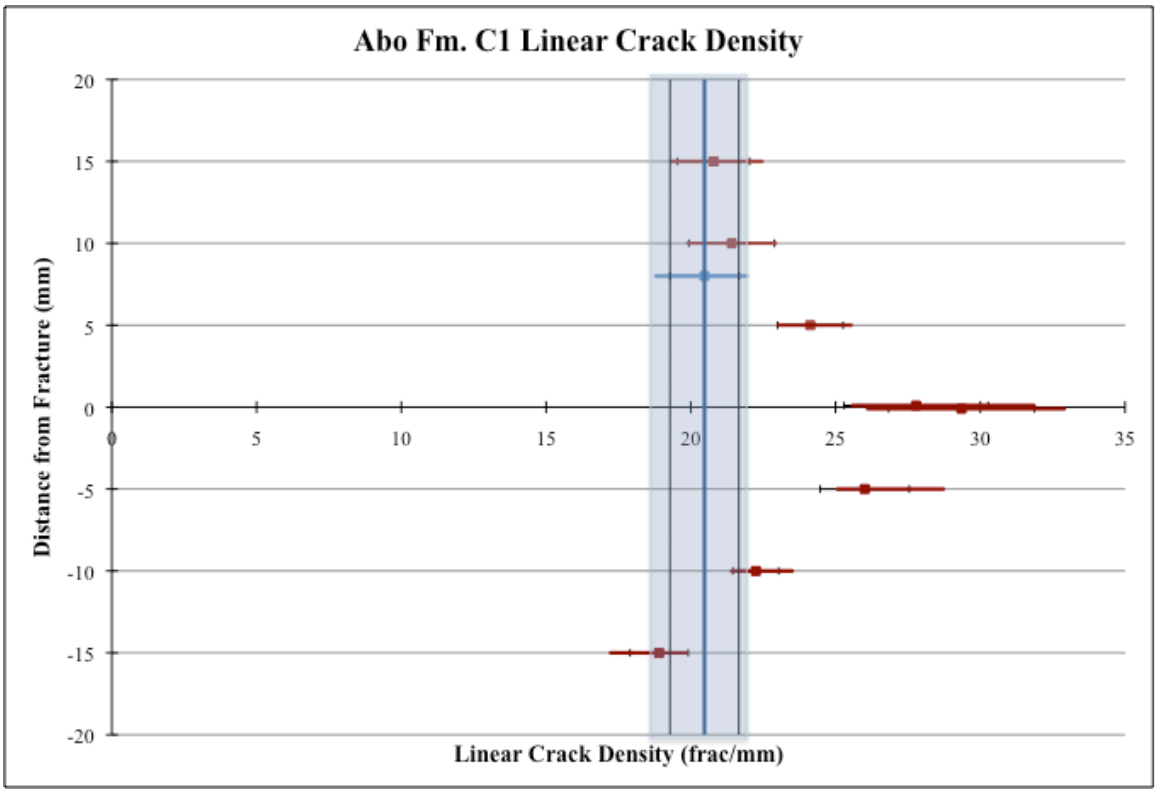

Figure 5.17. Average linear crack density for Homogeneous – Anisotropic Abo Fm. NHF is at zero, blue band shows background linear crack density. Each value represents the average linear crack density at that distance and is accompanied by the span of linear crack densities and the average's error bar.

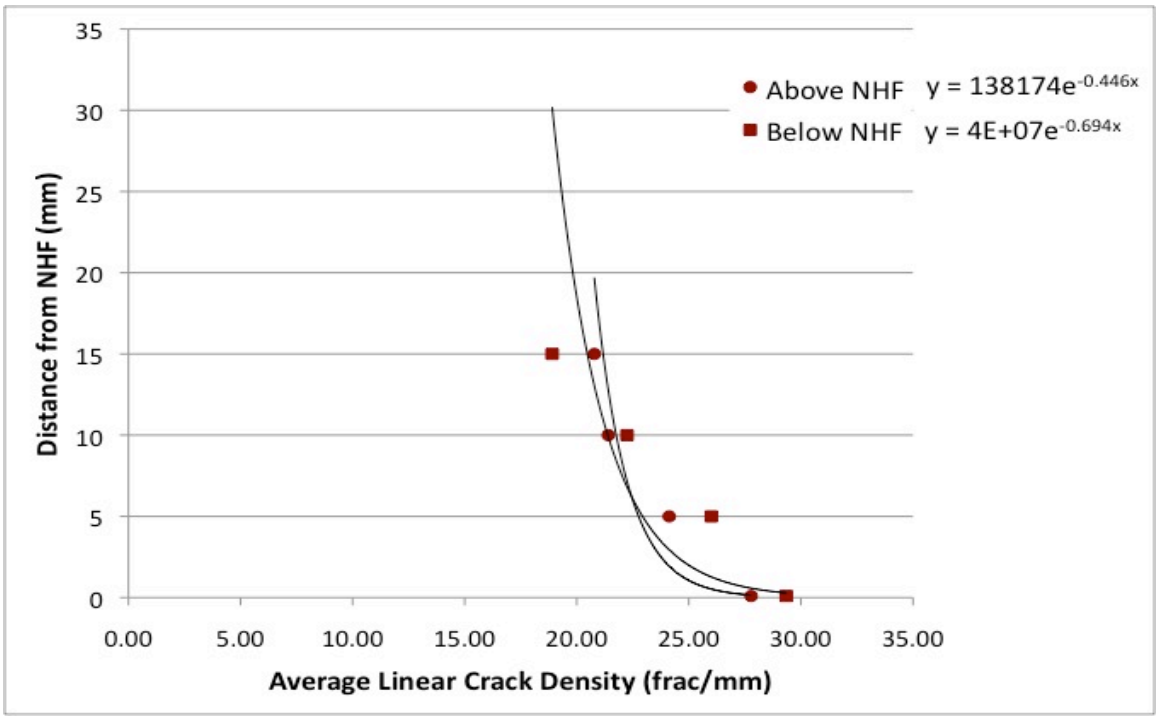

Figure 5.18. Average linear crack density for Abo Fm., with exponential fit.

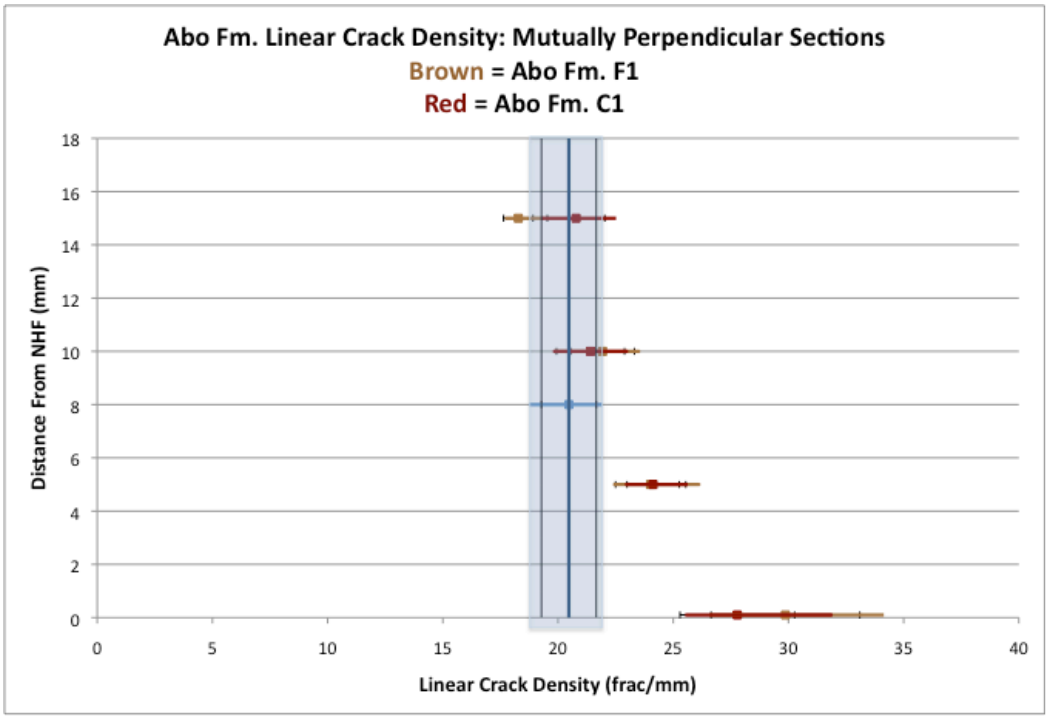

Figure 5.19. Linear crack density values for two mutually perpendicular thin sections from Abo Fm. Each value represents the average linear crack density at that distance and is accompanied by the span of linear crack densities and the average's error bar.

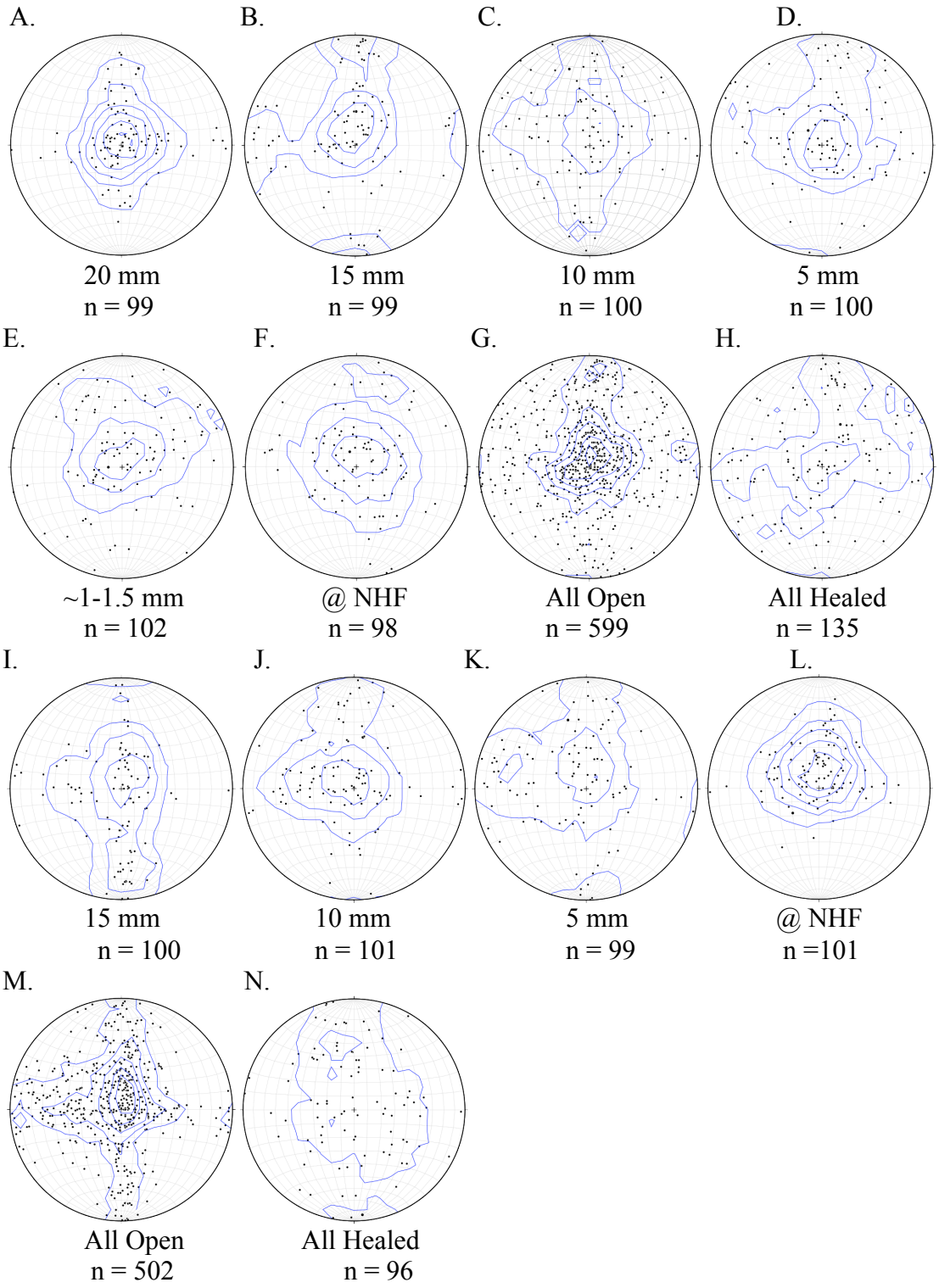

Figure 5.20. Microfracture orientations perpendicular to SPss-1's NHF. Plotted on equal area, lower hemisphere steronets, oriented looking down the core axis. A kamb contour is used to contour the data at a confidence interval of 3.0. A-H) Orientations above the NHF. I-N) Orientations below the NHF.

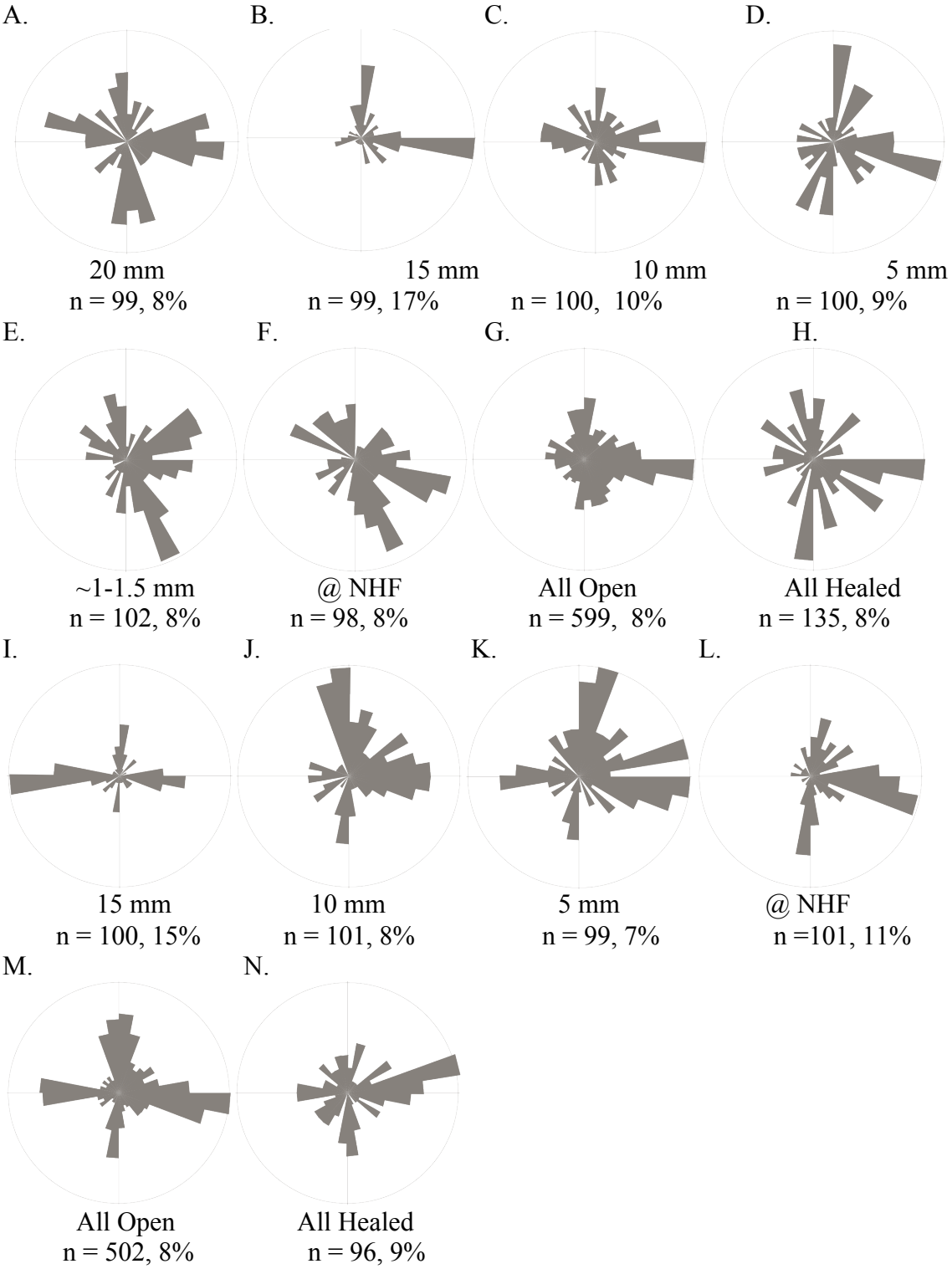

Figure 5.21. Rose diagrams of microfracture orientations perpendicular to SPss-1 NHF. Outside circles of each plot are percantages of each highest strike bar. A-H) Orientations above the NHF. I-N) Orientations below the NHF.

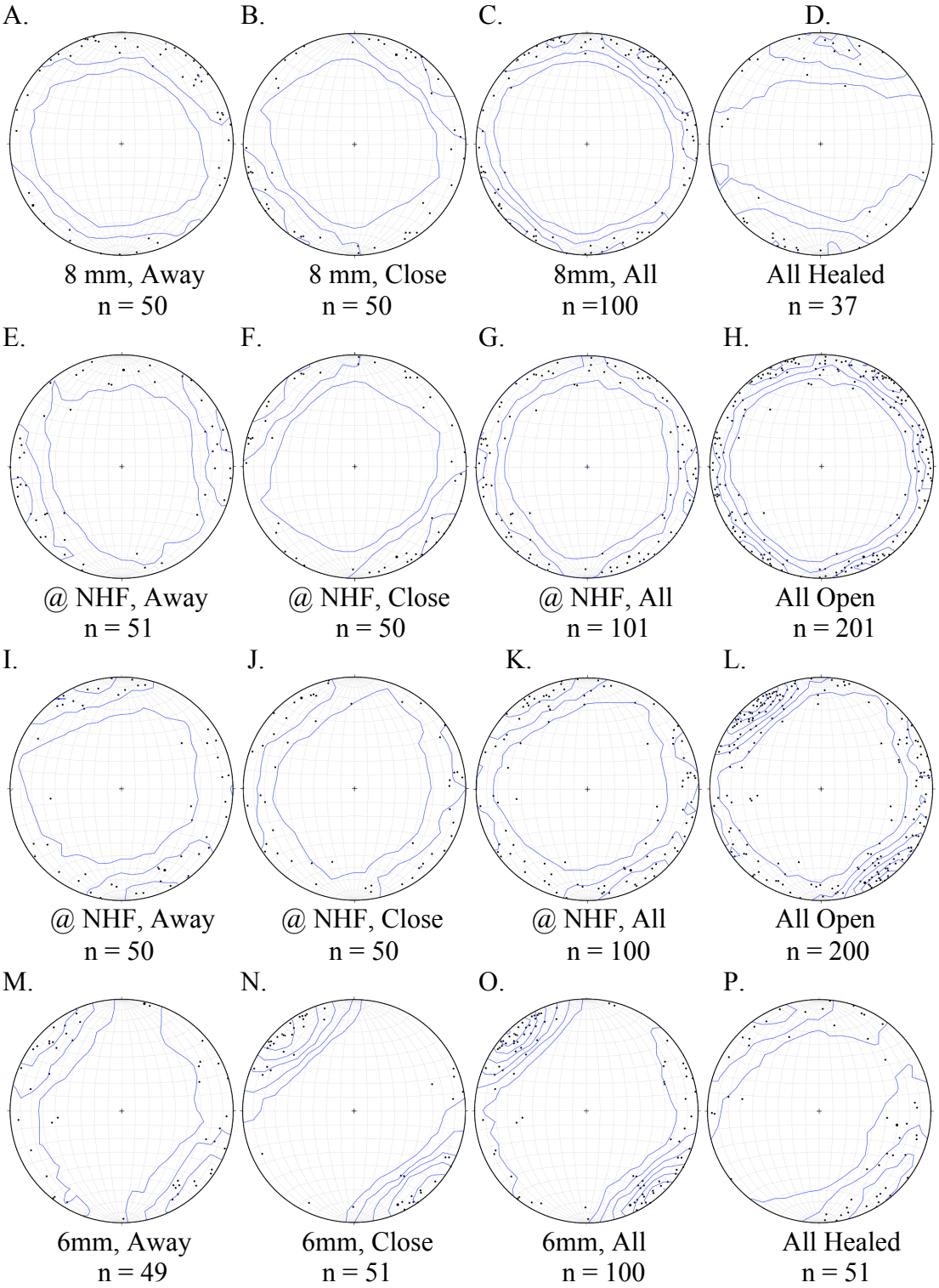

Figure 5.22. Microfracture orientations parallel to SPss-1's NHF. A-H) Above the NHF and I-P) Below the NHF

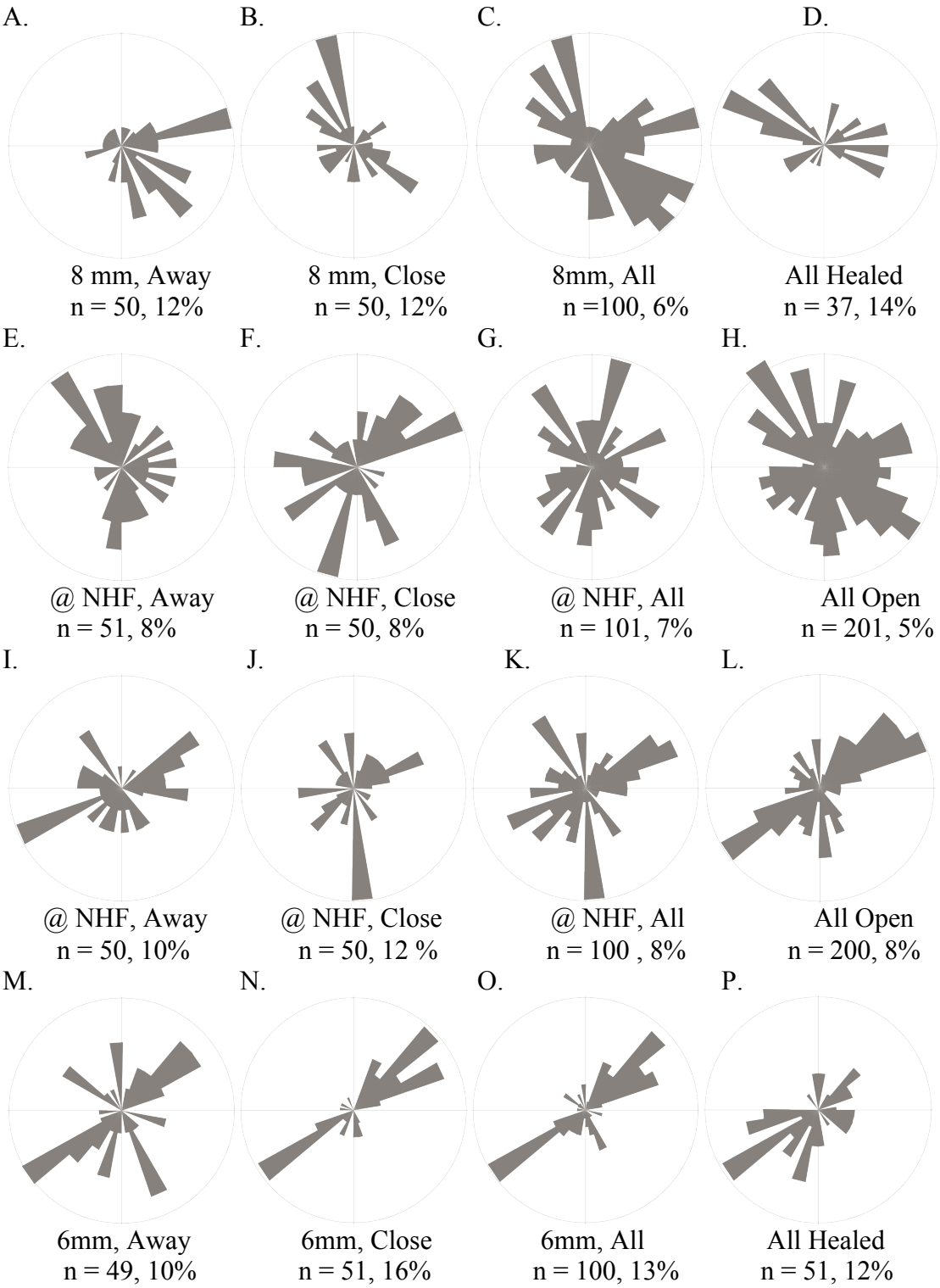

Figure 5.23. Rose diagrams of microfracture orientations parallel to SPss-1's NHF. A-H) Above the NHF and I-P) Below the NHF

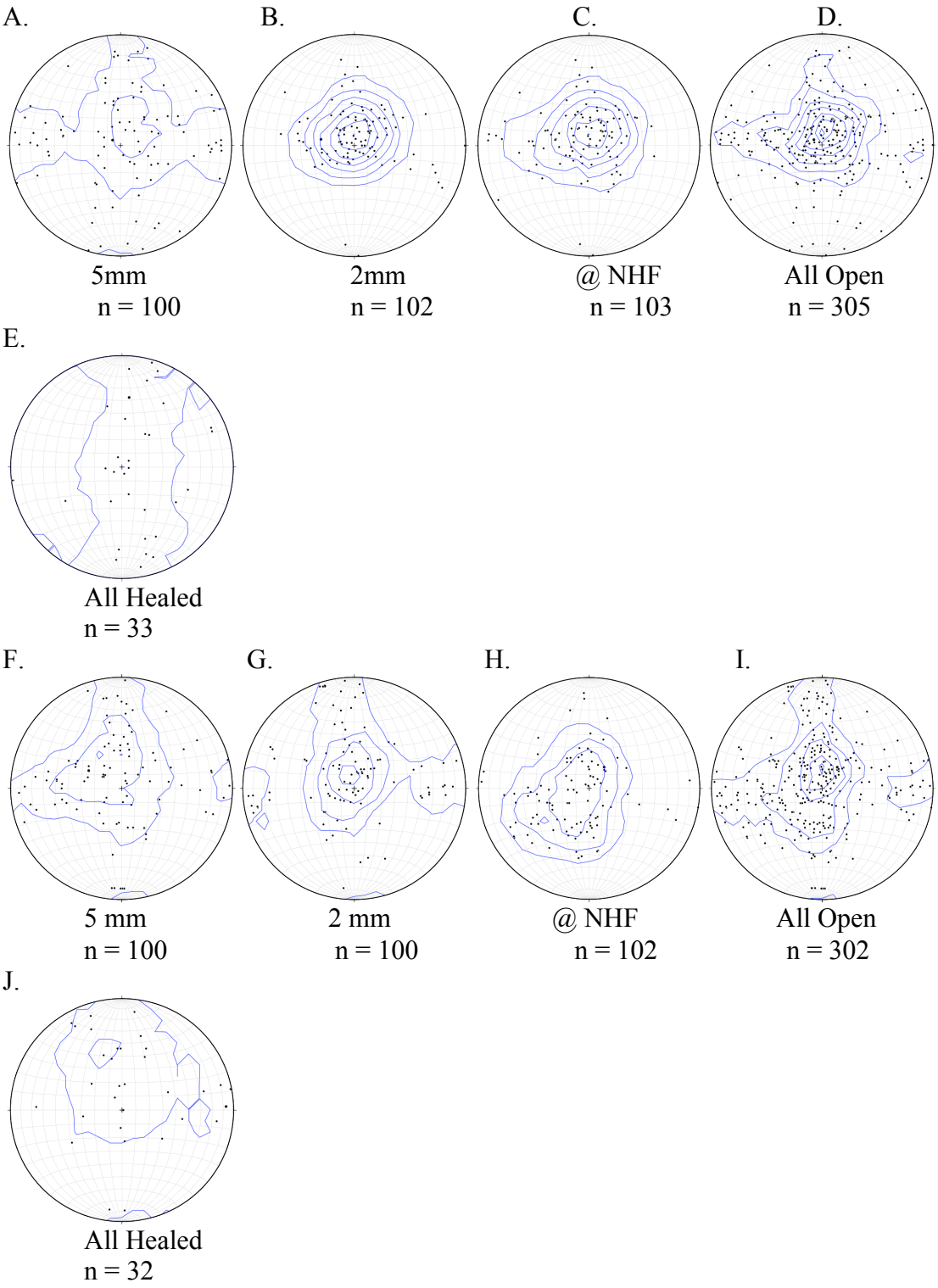

Figure 5.24. Microfracture orientations perpendicular to SPss-2's NHF. Plotted on equal area, lower hemisphere steronets, oriented looking down the core axis. A kamb contour is used to contour the data at a confidence interval of 3.0. A-E) Orientations above the NHF G-J) Orientations below the NHF

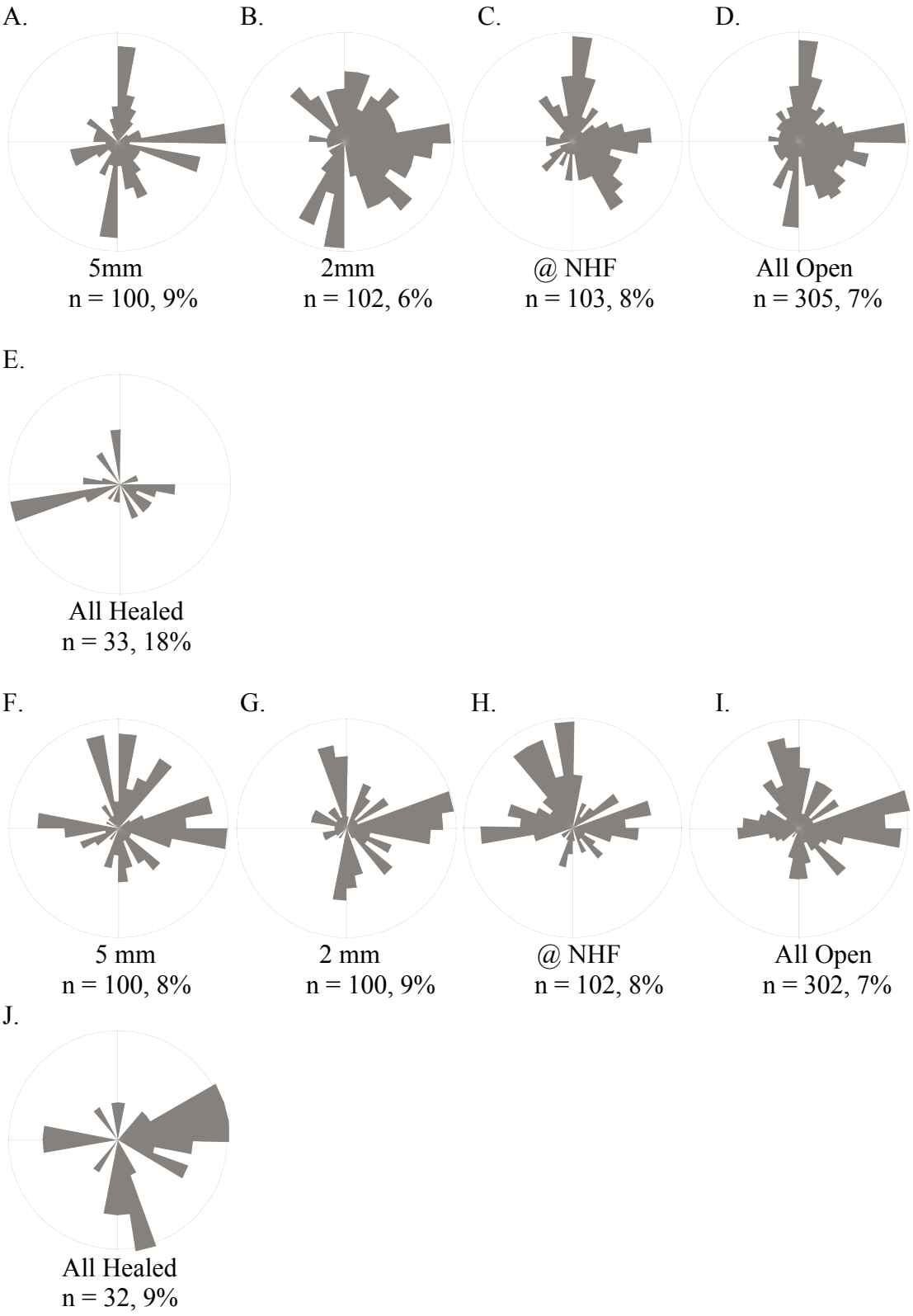

Figure 5.25. Rose diagrams of microfracture orientations perpendicular to SPss-2's NHF. A-E) Above the NHF and I-J) Below the NHF

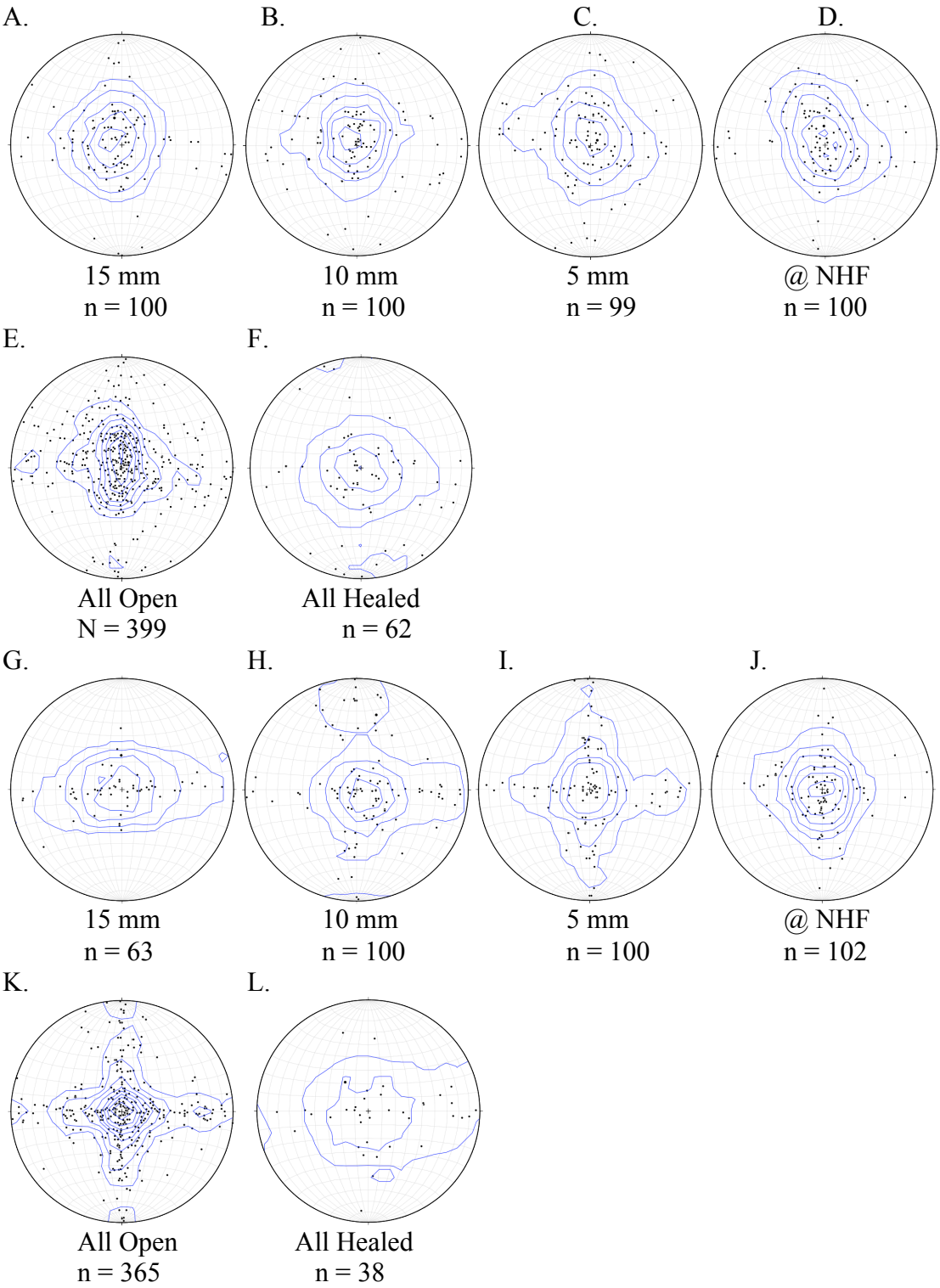

Figure 5.26. Microfracture orientations perpendicular to Abo Fm's NHF. Plotted on equal area, lower hemisphere steronets. Plots are oriented looking down the core axis. A kamb contour is used to contour the data at a confidence interval of 3.0. A-F) Orientations above the NHF G-L) Orientations below the NHF.

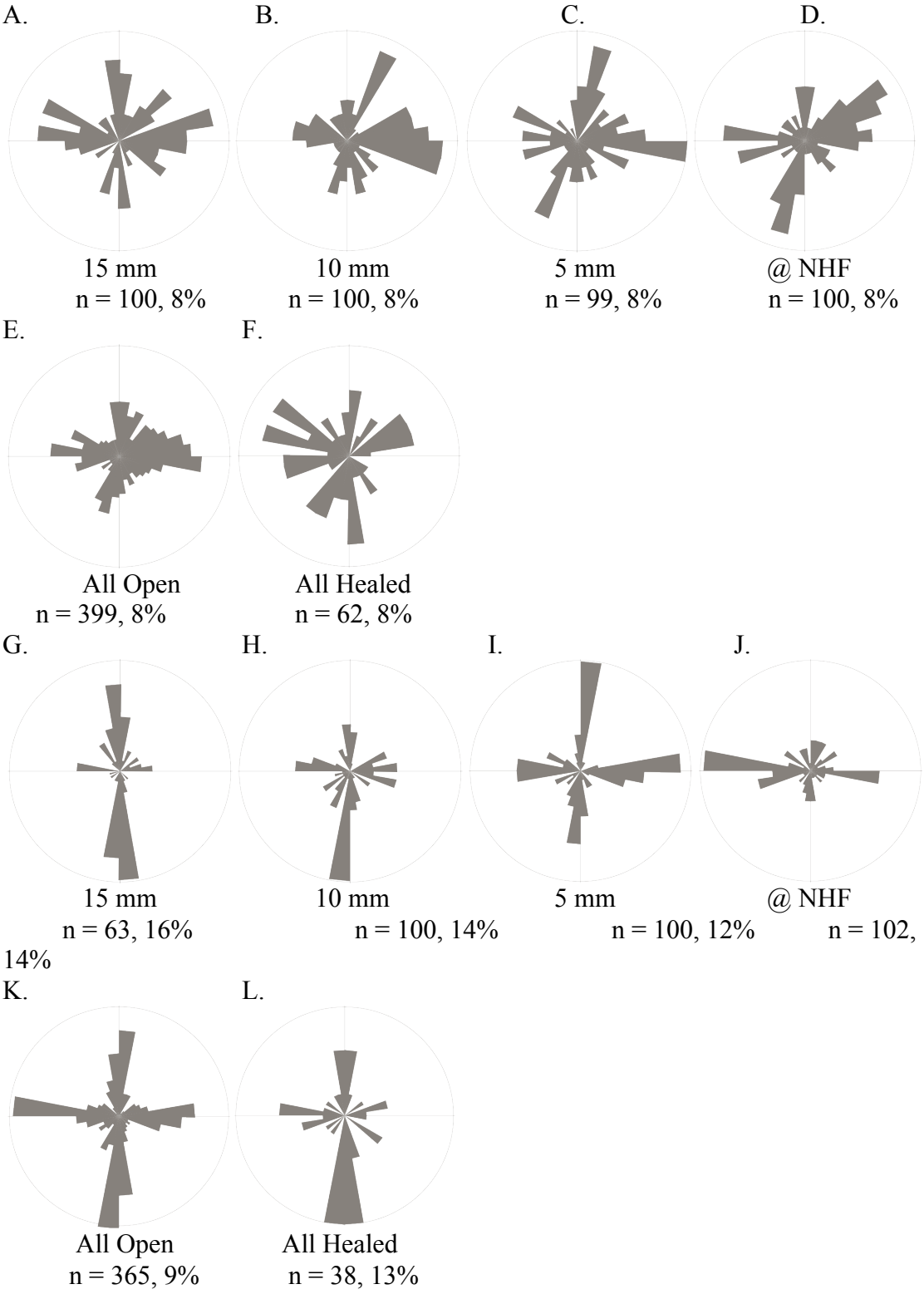

Figure 5.27. Rose diagrams of microfracture orientations perpendicular to Abo's NHF. Outside circles of each plot are percentages of each highest strike bar. A-F) Orientations above the NHF. G-L) Orientations below the NHF

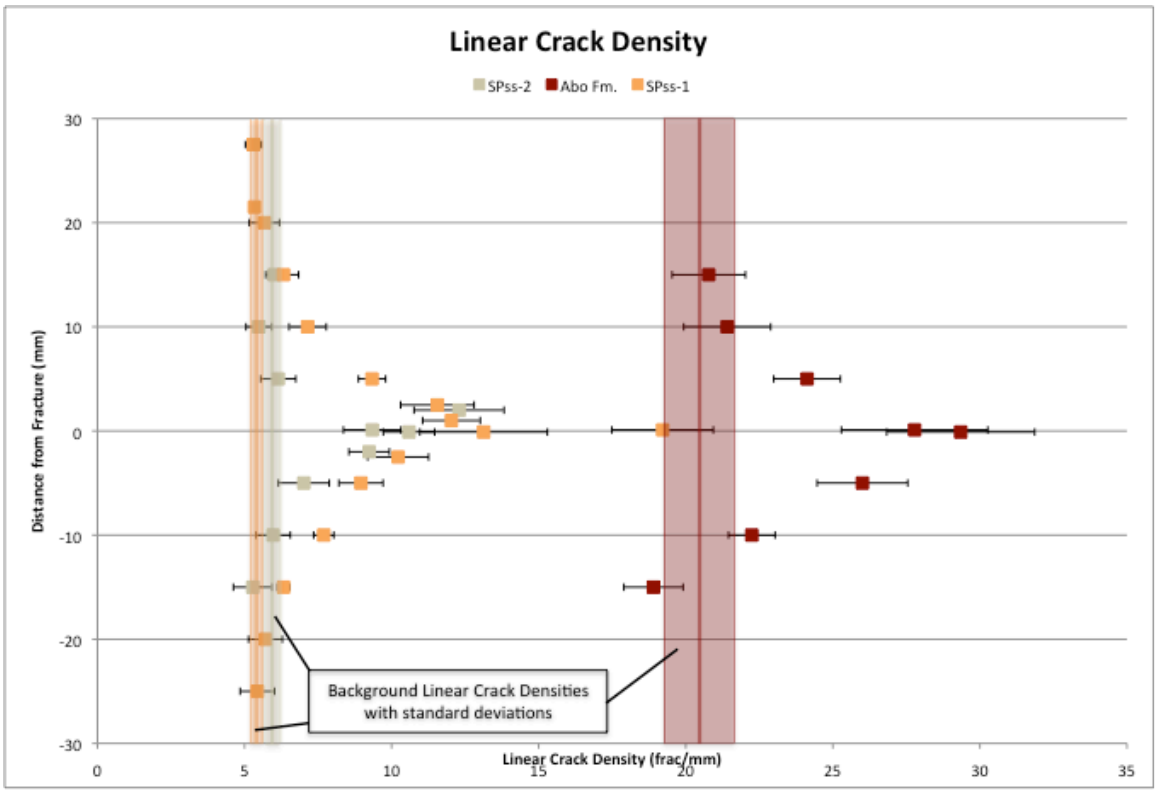

Figure 6.1. Compilation of linear crack density from each sample.

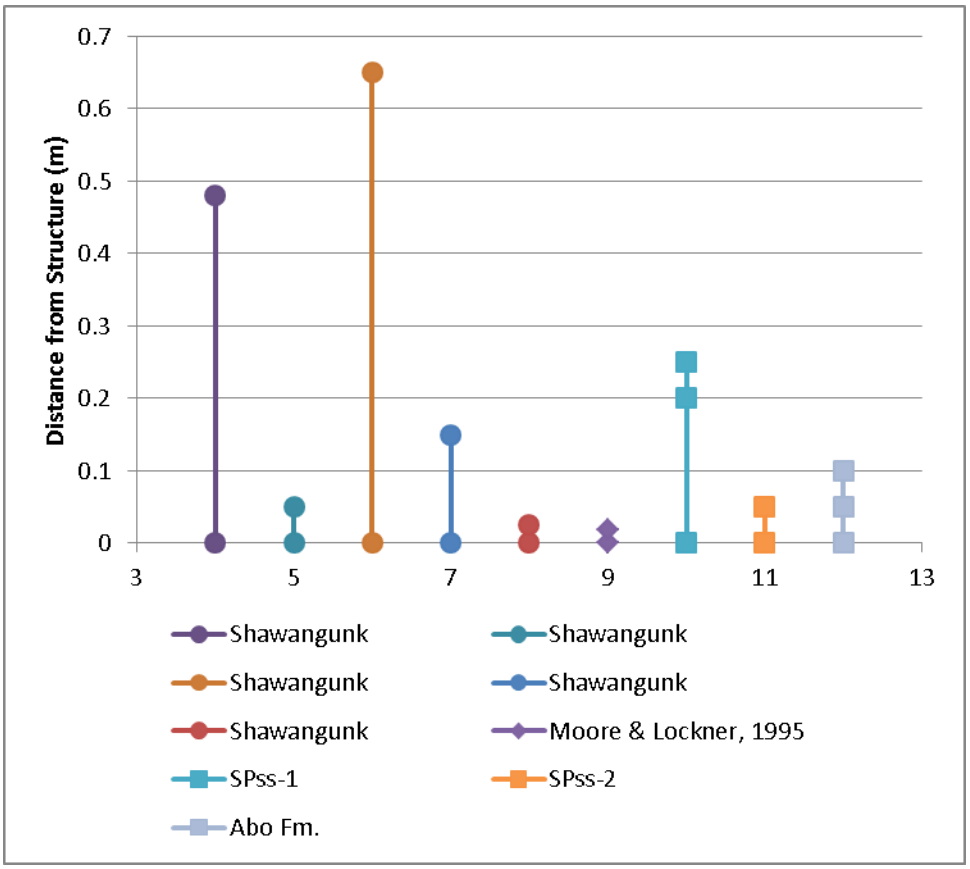

Figure 6.2 Comparison of damage zone widths. Damage zone widths from this study, the Shawangunk Mountians (Vermilye & Scholz, 1998) and a shear fracture propagated under laboratory conditions in granite (Moore & Locker, 1995).

	Damage Zone Width (m)	Rock type	Formation Name	Structure Associate With	Study/Reference
Natural					
	3-18	Sandstone	Navajo & Entrada	Arches National Park fault, normal	Anders & Wilschko 1994
	4-20	Sandstone	Aztec	Muddy Mountain Thrust fault	Brock & Engelder 1977
	30 associated with fault 100 to background, includes regional	Sandstone	Punchbowl	Punchbowl fault	Wilson et al. 2003
	0.48	Sandstone & Conglomerates	Shawangunk Formation	Alligerville fault:Strile-Slip	Vermilye & Scholz 1998
	0.05	Sandstone & Conglomerates	Shawangunk Formation	Millbrook Cliff fault: Strike-Slip	Vermilye & Scholz 1998
	0.65	Sandstone & Conglomerates	Shawangunk Formation	Mossy Maple fault: Strike-Slip	Vermilye & Scholz 1998
	0.15	Sandstone & Conglomerates	Shawangunk Formation	Millbrook Face fault: Strike-Slip	Vermilye & Scholz 1998
	0.025	Sandstone & Conglomerates	Shawangunk Formation	Gertrude's Nose fault:Reverse	Vermilye & Scholz 1998
	150	Granodioritic composition		Caleta Coloso fault: Strike-Slip	Faulkner et al. 2006
Experimental					
	0.018	Granite	Westerly	Shear Fracture	Moore & Lockner 1995
	Process Zone width (mm): 2.0mm to 5.6mm	Granite		Shear Fracture	Janssen et al. 2001
	0.2 - 0.25	Sandstone	St. Peters (3_2)	Natual Hydraulic Fracture	this study
	0.05	Sandstone	St. Peters (12_1)	Natual Hydraulic Fracture	this study
	0.05-0.1	Siltstone	Abo	Natual Hydraulic Fracture	this study

Table 6.1. Damage zone compilation. That are associated with natural faults, shear fractures, experimentally produced fractures and models, including those from this thesis.

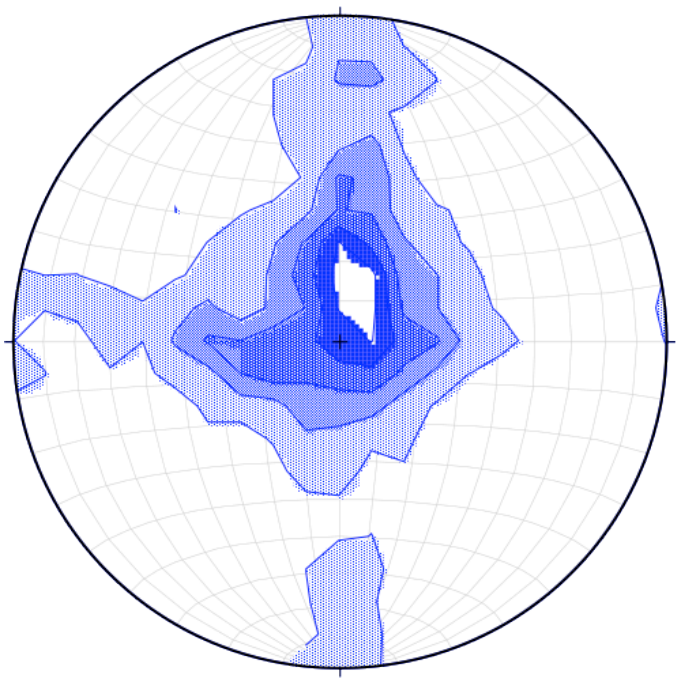

n = 1002

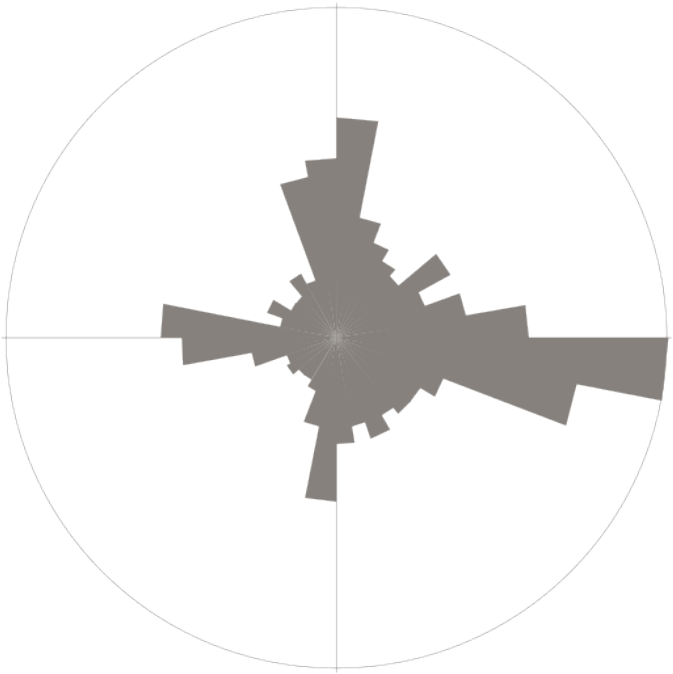

n = 1002, 8%

Figure 6.3. Composite equal area net of SPss-1. Showing all microfracture orientations collected from perpendicular thin sections.

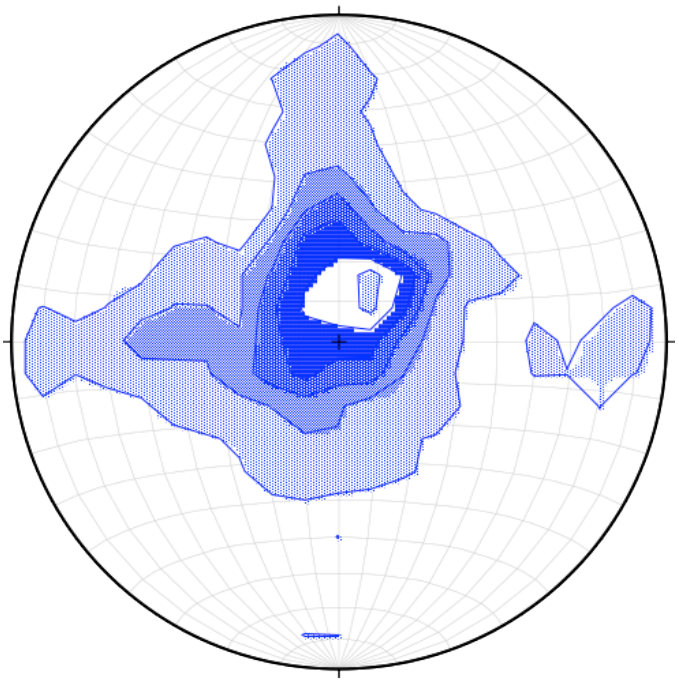

n = 607

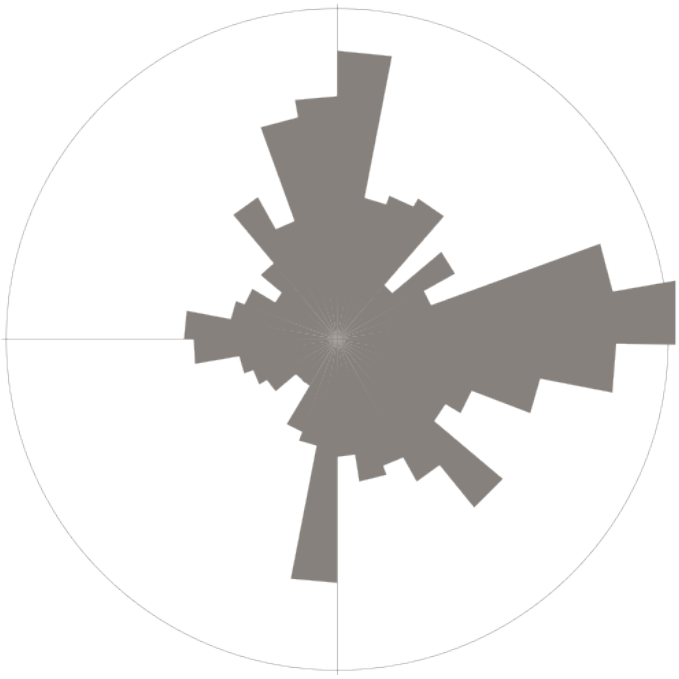

n= 607, 6%

Figure 6.4. Composite equal area net of SPss-2. Showing all microfracture orientations collected from perpendicular thin sections.

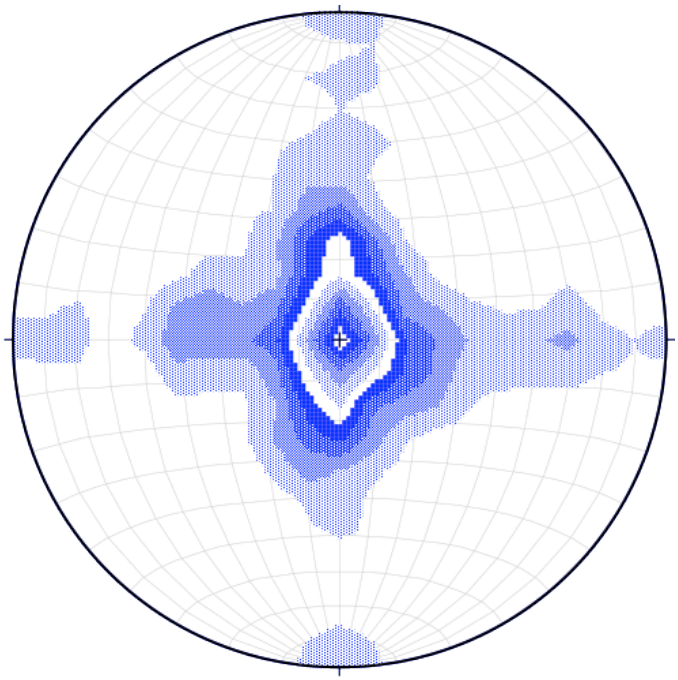

n = 764

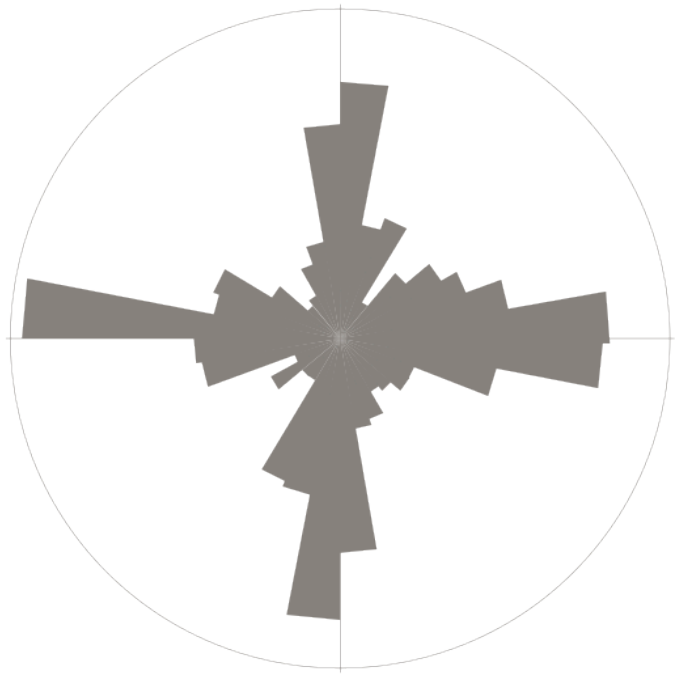

n = 764, 7%

Figure 6.5. Composite equal area net of Abo Fm. Showing all microfracture orientations collected from perpendicular thin sections.

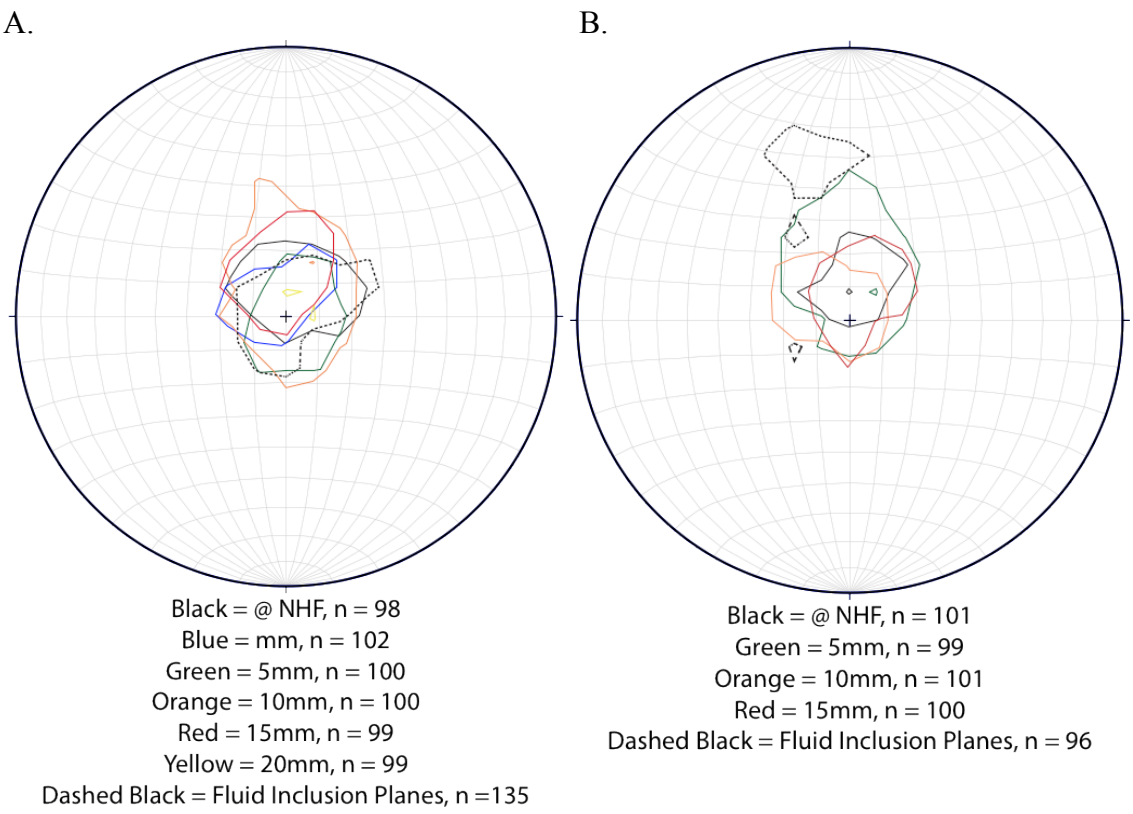

Figure 6.6. Composite highest Kamb contour plot of SPss-1. A) Top. B) Bottom.

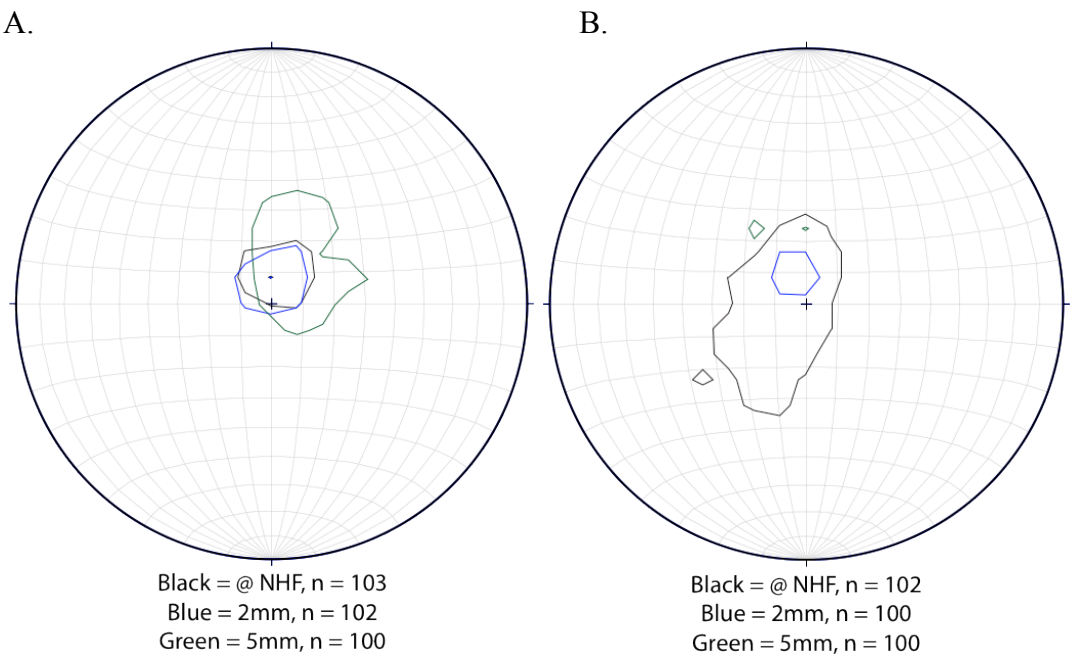

Figure 6.7. Composite highest Kamb contour plot of SPss-2 A) Top. B) Bottom.

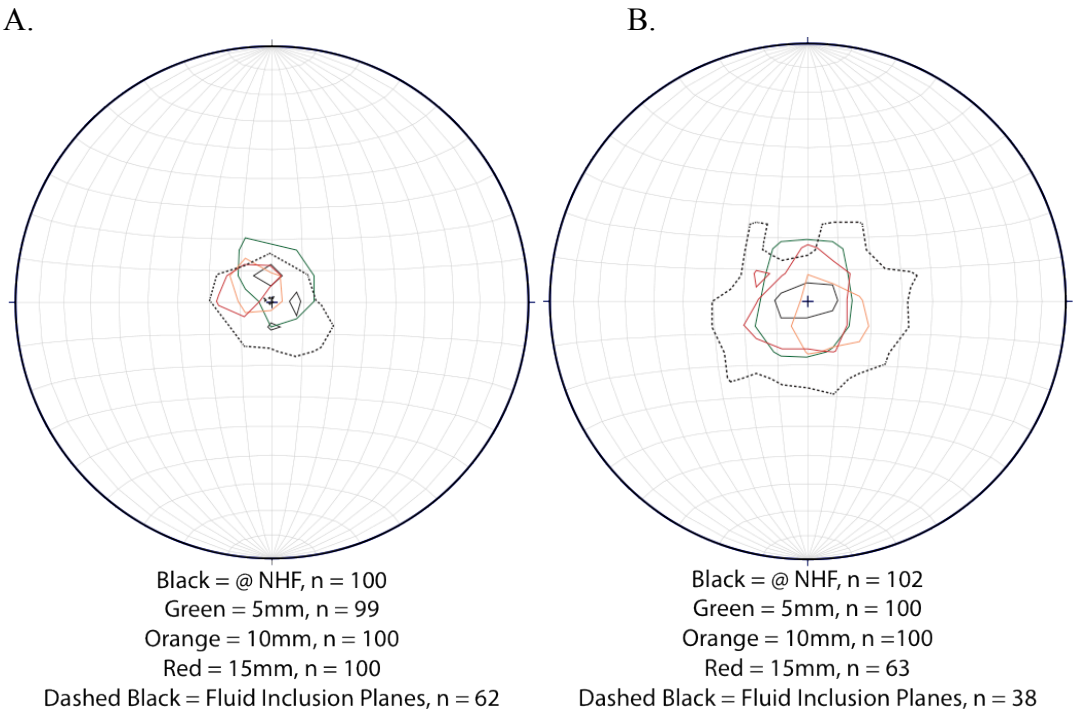

Figure 6.8. Composite highest Kamb contour plot of Abo Fm. A) Top. B) Bottom.

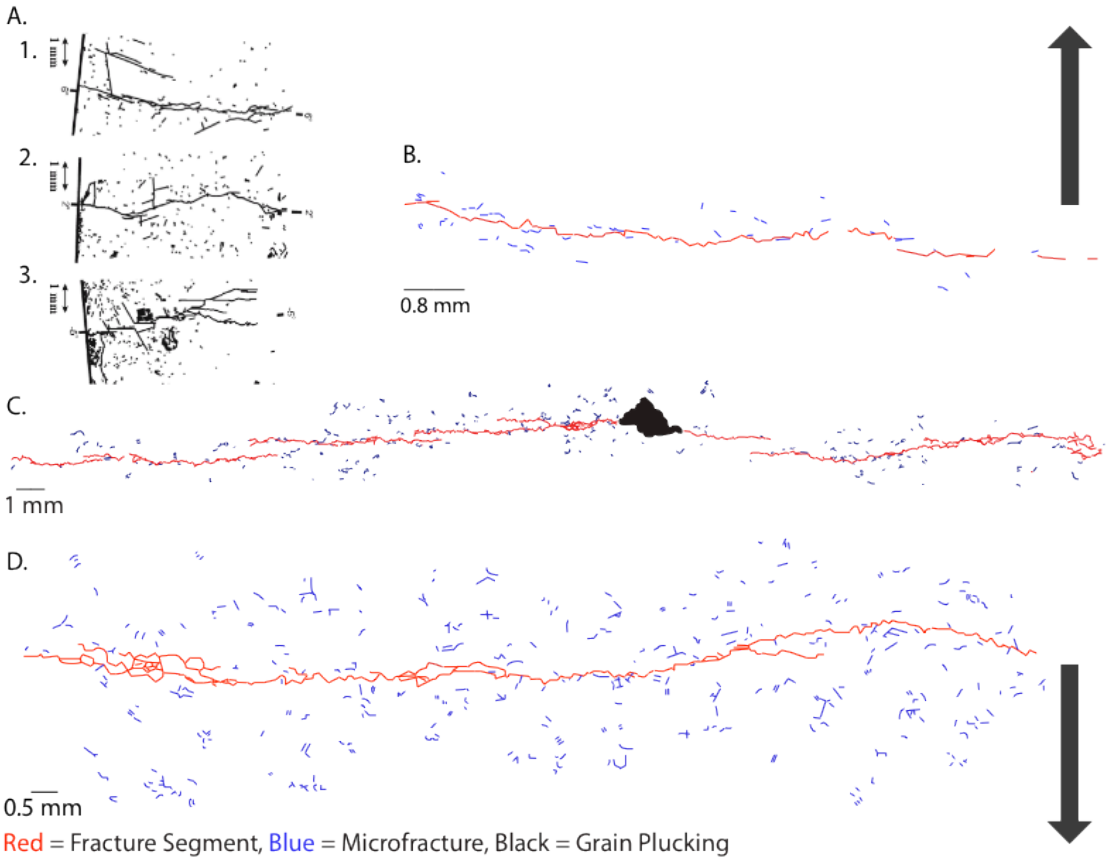

E.

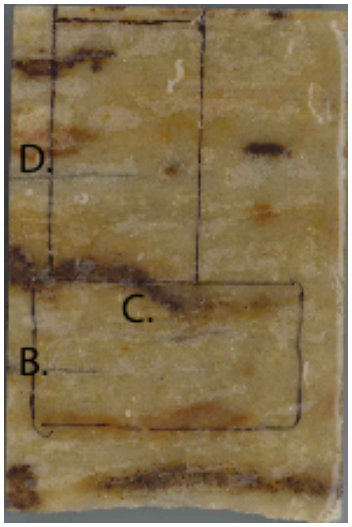

Figure 6.9. Comparison of non-through-going fracture traces to uniaxial experiments. Black arrows show maximum tension direction for all fractures. A) Fracture traces from uniaxial experiments: A-1) Sample loaded solely in tension, A-2) Sample loaded in compression followed by tension, A-3) Sample loaded in tension followed by compression (adapted from Ganne & Vervoort, 2007). B-D) Non-through going fractures from SPss-2. E) Section of SPss-2 core (SPss-2 B1) used to create thin sections of non-through-going fractures B, C and D correspond to the fracture traces above.

Distance from fracture (mm)	SPss-1		SPss-2		Abo Fm.	
	Average LCD (frac/mm)	Avg - Background (frac/mm)	Average LCD (frac/mm)	Avg - Background (frac/mm)	Average LCD (frac/mm)	Avg - Background (frac/mm)
27.5	5.30	-0.10				
21.5	5.33	-0.07				
20	5.68	0.27				
15	6.32	0.92	6.01	0.07	20.78	0.31
10	7.15	1.74	5.49	-0.45	21.41	0.94
5	9.33	3.93	6.15	0.21	24.13	3.66
2.5	11.56	6.15				
2			12.29	6.35		
1	12.03	6.63				
0.1	19.21	13.81	9.34	3.40	27.78	7.31
0.1	13.13	7.73	10.59	4.65	29.35	8.88
2			9.24	3.30		
2.5	10.22	4.82				
5	8.96	3.56	7.01	1.08	26.01	5.54
10	7.69	2.29	5.97	0.03	22.25	1.78
15	6.32	0.92	5.28	-0.66	18.90	-1.57
20	5.71	0.31				
25	5.44	0.03				

Table 6.2. Percent Increase in linear crack density from background levels.

Distance from fracture (mm)	en echelon		short		connected	
	Average LCD (frac/mm)	Avg - Background (frac/mm)	Average LCD (frac/mm)	Avg - Background (frac/mm)	Average LCD (frac/mm)	Avg - Background (frac/mm)
0.1	8.82	2.88	9.55	3.61	8.54	2.60
0.1	8.92	2.98	9.2	3.26	8.51	2.57

Table 6.3. Percent Increase in linear crack density along non-through-going fractures.

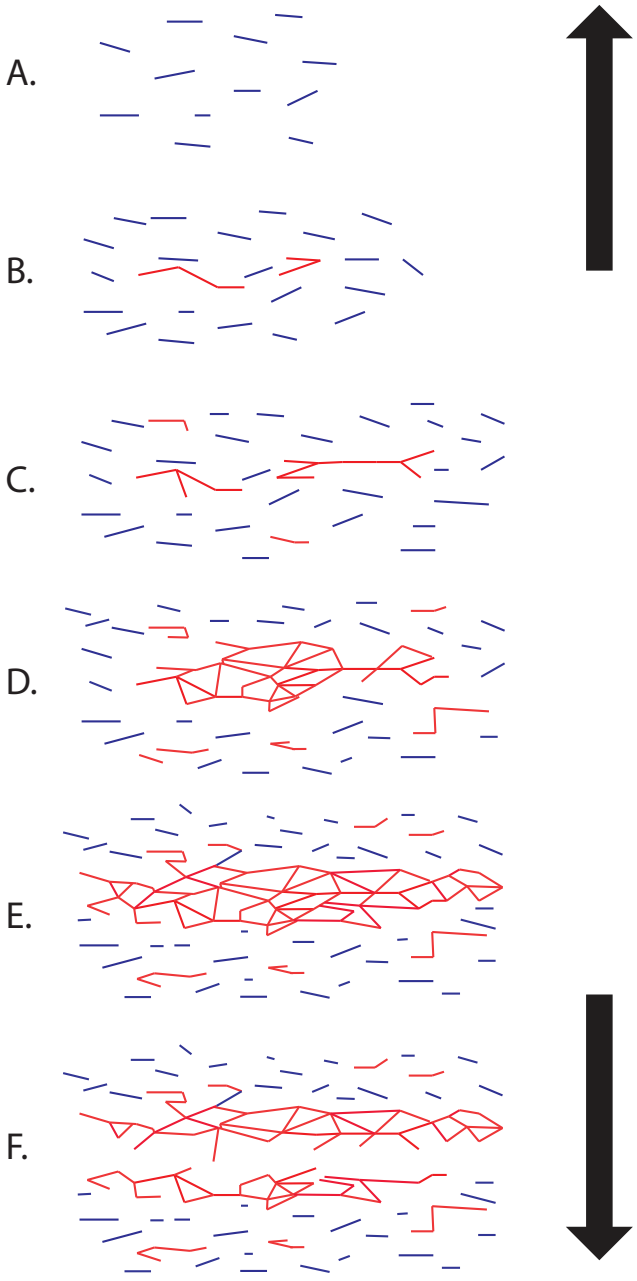

Figure 6.10. Conceptualization of initiation, propagation and formation of a NHF. Blue = microfractures, Red = connected microfractures, Black arrows = direction of maximum tension. A) Formation and calescence of microfractures B) linkage of microfractures C) Continuing linkage and formation of microfractures D) Formation of fracture bound lenses and more microfracture formation. E) Fracture bound lenses continue to develop and increase in damage zone microfractures. F) The second the fracture bound lenses form a continuous path from one side of the rock to the other separation occurs forming a fully though going NHF.

APPENDIX A

MICROFRACTURE ORIENATION CORRECTION

The Universal Stage used did not have the zero/180 strike lined up at horizontal to the eyepieces, it was 25° off. Therefore a 25° correction has to be used for each strike obtained. After strikes were corrected for the 25° discrepancy, orientations from thin sections are corrected to represent their true orientations in the core so that steronets could be used for analysis. If the stage is rotated clockwise than true strike = 90 – 25° correction, if rotated counter clockwise than true strike = 90 + (360 – 25° correction). All dips are corrected so that true dip = | 90 – measurement |. True orientations are then entered into Stereonet and plotted as poles to microfractures.

Because orientations are collected on mutually perpendicular thin sections, data sets have to be rotated so they are all viewed on the same plane. Three designations are given to the thin sections based on their orientations in the core; these do not correspond to true orientations. There is a North-South (N-S) thin section, an East-West (E-W) thin section and a Fracture Plane thin section. Rotations for each orientation are shown in Figure A.1. These will cause all steronets to be oriented looking down on the NHF. Therefore, the fracture plane thin sections are already in the correct orientation and only need to be rotated 180° if the thin section is oriented looking up the plunge of the core instead of down the plunge. Thin sections in the N-S plane are rotated twice. They are rotated 90° about the core axis, joining E-W thin sections on the same plane. Then they are rotated -90° about the azimuth 90°, as are E-W thin sections. This puts all orientations in the same plane.

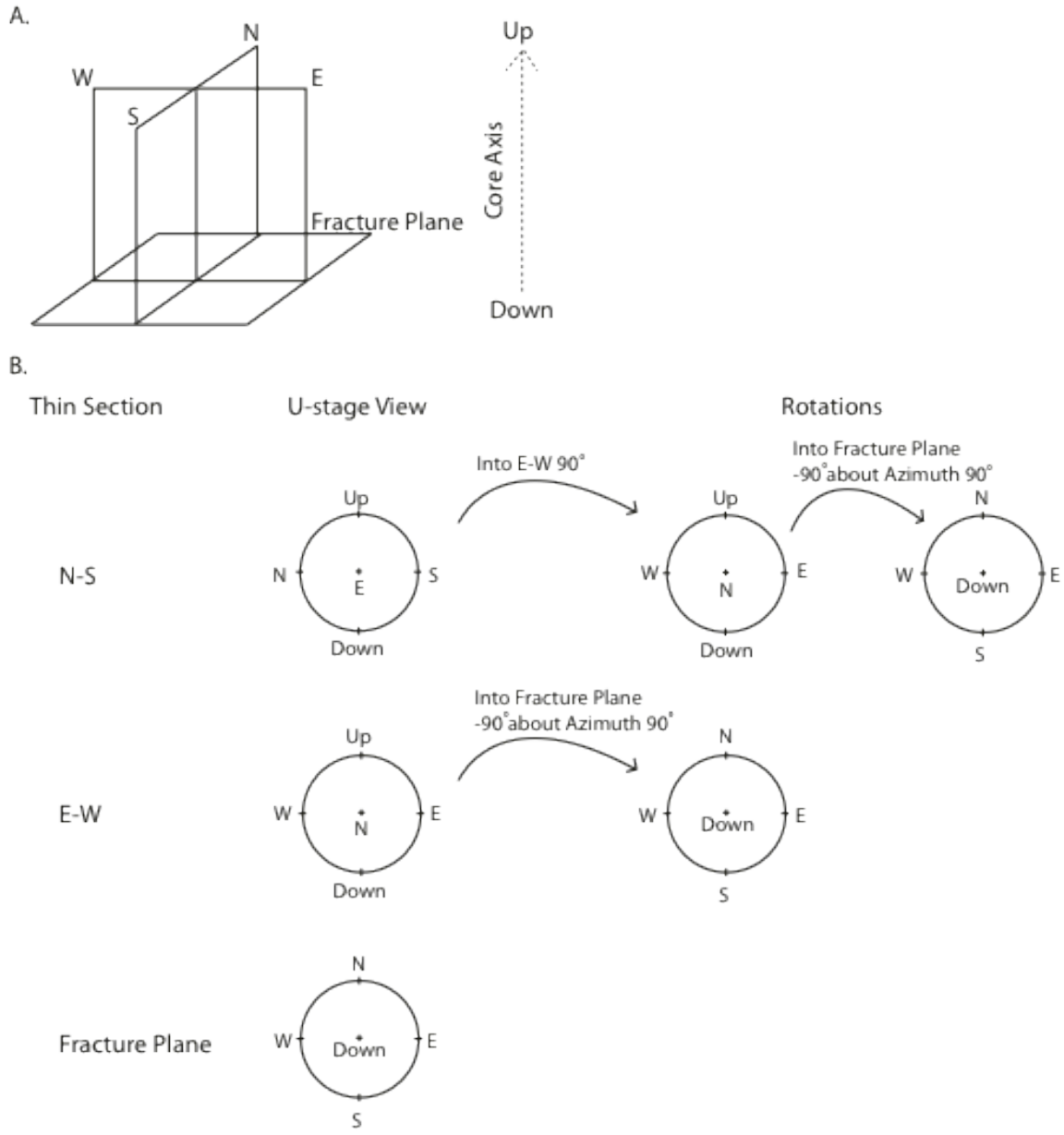

Figure A.1. Thin section rotations. Three mutually perpendicular thin sections rotated into one common plane. A) Orientation of thin sections in relation to each other and core axis. B) Rotations of each different thin section orientation, so each steronet is viewed as if looking down on the NHF surface with the core axis in the center.

APPENDIX B

WEIGHTING OF EQUAL AREA NETS

In order to best analyze orientation data from a U-stage, which may oversample certain areas (Figure 4.11) a weighting scheme is investigated. First dip histograms plots showing raw dips from all orientations collected are investigated (Figure B.1). Dip histograms show that there isn't a bias for dip direction between different thin sections. The majority of microfractures being collected fall within 15° of the thin section plane. This means that a weighting scheme, which would make all dips have the same frequency, is not possible. It would extremely eschew the data.

Next a pole count is conducted to discover if certain areas of an equal area net are being oversampled and if a correction could fix this. For each thin section orientation a set of 100 microfracture orientations are plotted on a measurable areas steronet (Figures B.2). Separate pole counts that count the number of orientations in each 10° window of overlapping thin section orientations are done for the entire extent of the equal area plot, windows are formed by overlapping degree orientations from each thin section. For example orientations in Figure B.2 are from a north – south oriented thin section. All the poles that lie between the 0-10° lines for a N-S (shaded red) thin section and between the 0-10° E-W (shaded blue) are counted. Table A.1 and A.2 show an example of a finished pole count for the equal area net in Figure B.2.

The pole count for all three equal area nets in Figure B.2 shows that a real bi-modal distribution of fractures is present. Either fractures are steeply dipping or shallowly dipping with respect to the NHF. Based on this outcome a weighting scheme cannot be developed.

A.

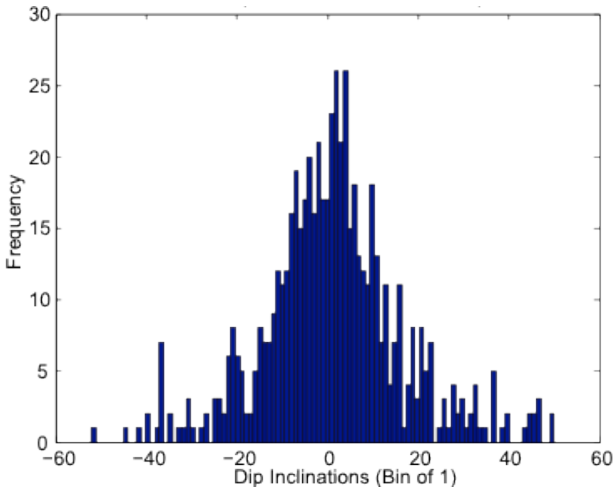

B.

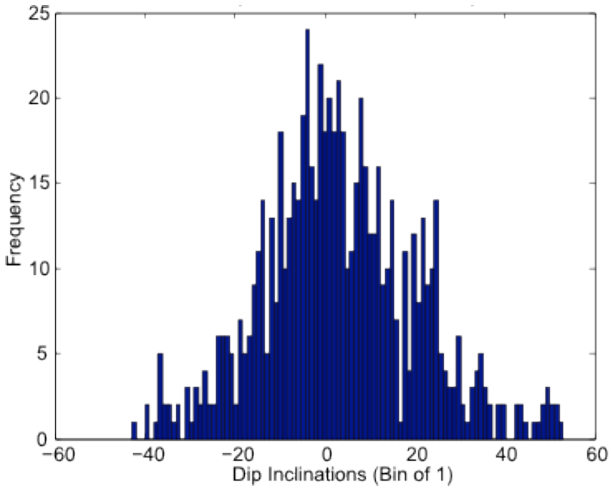

C.

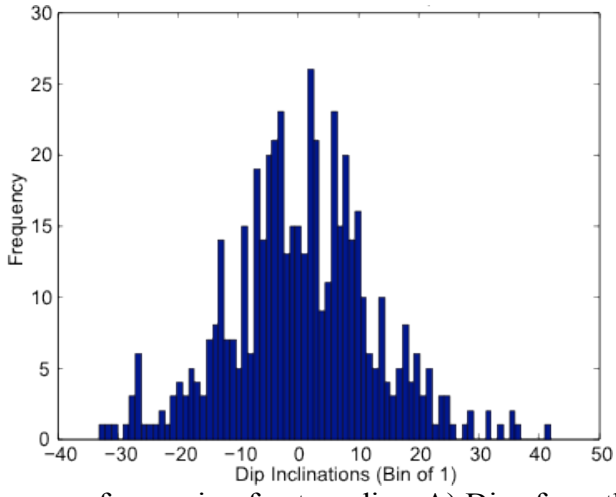

Figure B.1 Dip histograms of raw microfracture dips. A) Dips from thin sections oriented N-S. B) Dips from thin sections oriented E-W. C) Dips from thin sections oriented parallel.

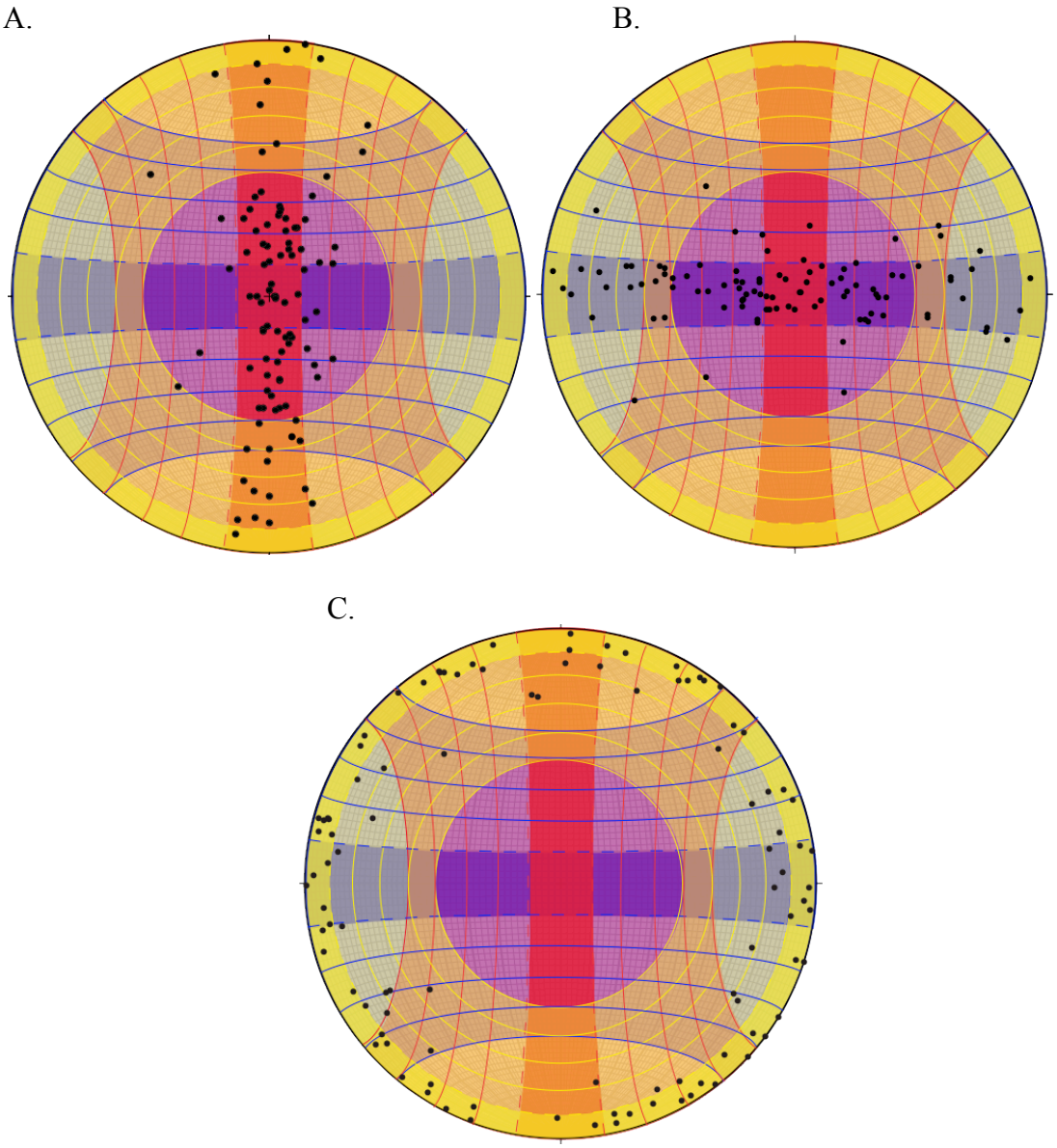

Figure B.2 100 orientations from each thin section orientation on measurable area plots. Blue = area measurable in an east – west oriented thin section, Red = area measurable in a north – south oriented thin section, Yellow = area measurable in a parallel oriented thin section. A) Microfracture orientations from a north – south oriented thin section. B) Microfracture orientations from an east – west oriented thin section. C) Microfracture orientations from a parallel oriented thin section.

N-S Degree Windows	0-10	10-20	20-30	30-40	40-50
Parallel Degree Windows					
0-10	4	1	0	0	0
10-20	4	2	0	0	0
20-30	5	0	1	0	0
30-40	4	0	1	1	0
40-50	5	1	1	0	0

Table B.1 Pole counts in N-S and parallel degree windows. These are from equal area net A in Figure B.2. All orientations falling in windows formed by N-S thin section degree lines and Parallel thin section degree lines.

N-S Degree Windows	0-10	10-20	20-30	30-40	40-50
E-W Degree Windows		Pole Count			
0-10	11	4	0	0	0
10-20	15	2	4	0	0
20-30	18	4	1	0	0
30-40	11	2	0	1	0
40-50	6	0	1	0	0

Table B.2 Pole counts in N-S and E-W degree windows. These are from equal area net A in Figure B.2. All orientations falling in windows formed by N-S thin section degree lines and E-W thin section degree lines.

APPENDIX C

SHAPE PREFFERED ORIENTATION

C.1 Methods

Images were taken of the Abo formation and the St. Peter Sandstone SPss-2 for shape preferred orientation analysis. Two images were taken per sample from mutually perpendicular thin sections that are parallel to the NHF. Grain maps were created with Image SXM, Adobe Illustrator and Adobe Photoshop. Then the images were imported into the program SPO2003 for analysis. SPO2003 uses the intercept method to determine if there is a grain shape preferred orientation by analyzing boundaries of objects as a population of lines (Launeau & Robin, 1996). This method has been proven useful for magmatic fabric measurement (Launeau & Robin, 1996), shape fabric analysis/SPO (Launeau, 1980; Panoozo, 1983), strain analysis (Panozzo, 1987; Launeau & Robin, 1996) and lineament analysis (Launeau & Robin, 1996) with a 2-dimensional image. The number of intercepted boundaries of a set of grains by parallel scan lines quantifies the fabric, its symmetry, direction(s) and intensity (Launeau&Robin, 1996) Quantifications are represented by rose diagrams showing the intercept counts, mean intercept lengths (traverse), grain directions and characteristic shape. Intercept counts shows the number of times a scan line intercepts an object in every direction. Objects preferred elongation is parallel to the shortest diameter of this rose. Rose of traverse is the reciprocal of the rose of intercept counts. The long axis here represents objects preferred elongation. Rose of directions shows the direction of objects boundaries and is used to characterize fabric symmetry. Characteristic shape is the common shape arising in a set of objects that has one set of identical, convex and centrosysmmetric objects with the same rose of intercept,

mean intercept length (traverse) and direction (Launeau&Robin, 1996). This rose does not represent an average shape. Together these four quantifications are used to analyze one 2-dimensional image.

C.2 Results

Shape preferred orientations were determined for both non homogenous-isotropic rocks. Figures C.1 and C.2 show perpendicular shape preferred orientations for SPss-2 and Figures C.3 and C.4 for Abo. Grains in SPss-2 have the same preferred elongation with an angles of 93.36° and 91.28°. They have the opposite fabric symmetry demonstrated by the rose of directions in Figure C.1-C and Figure C.2-C, but their characteristic shapes are the same. Grains in Abo also have similar preferred elongation directions with angles of 113.72° and 119.98°. Fabric symmetry is oriented the same in mutually perpendicular thin sections but has different widths, while the characteristic objects are similar with one more elliptical than the other.

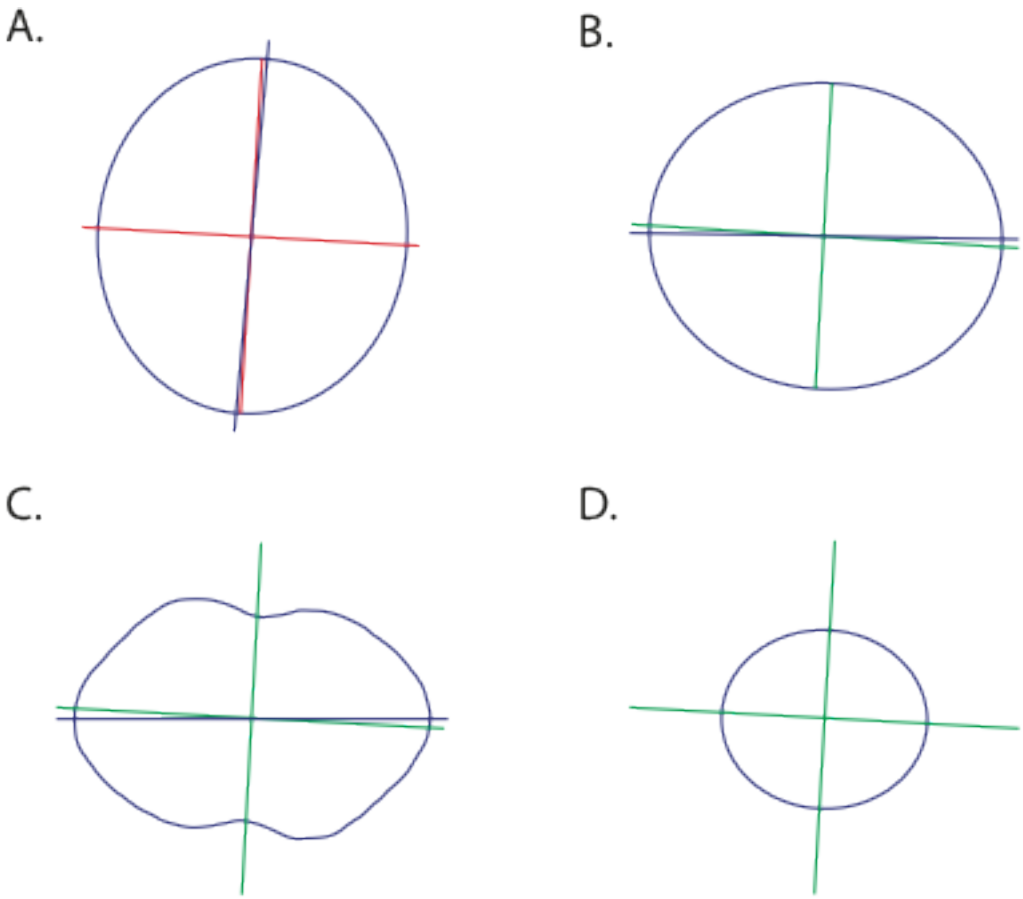

Figure C.1. Shape preferred orientation of SPss-2 A2. See Figure 4.2 for location within core. A) Rose of Intercepts. B) Rose of Traverses. C) Rose of Direction. D) Characteristic object. For all roses the ratio of the axis, R = 1.164 and the preferred angle of the grains is 93.36.

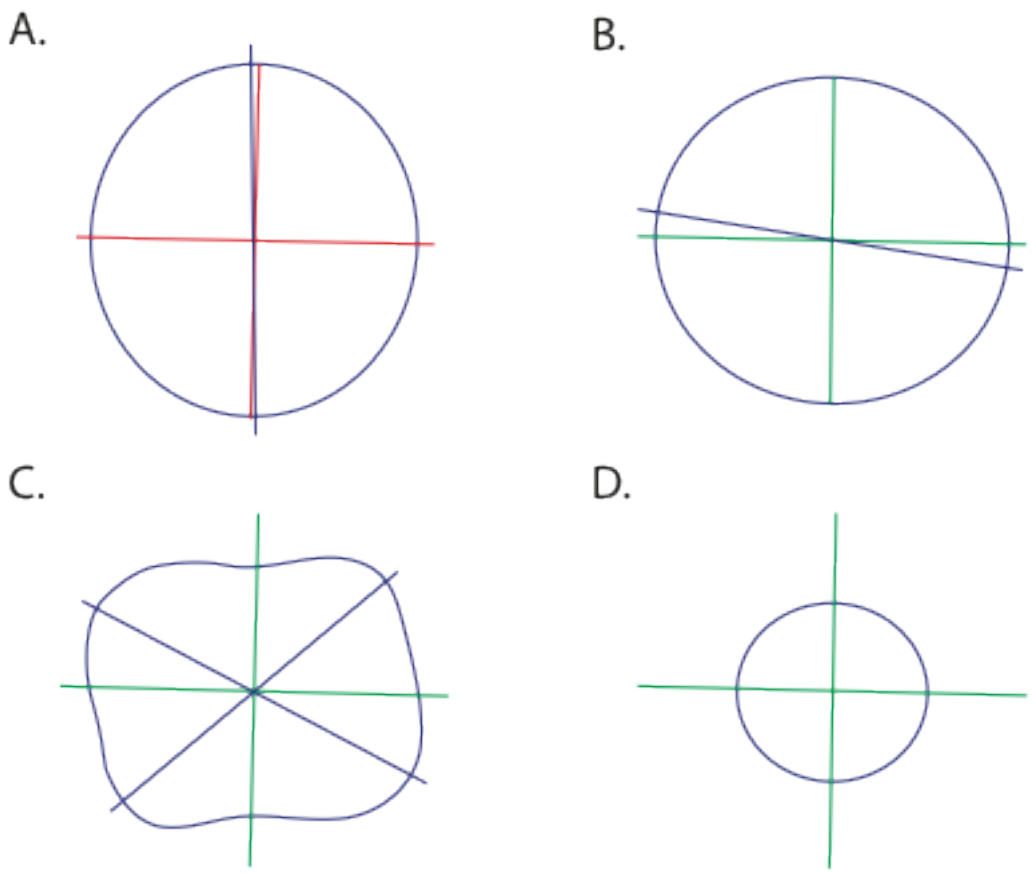

Figure C.2. Shape preferred orientation of SPss-2 A3. See Figure 4.2 for location within core A) Rose of Intercepts. B) Rose of Traverses. C) Rose of Direction. D) Characteristic object. For all roses the ratio of the axis, R = 1.087 and the preferred angle of the grains is 91.28.

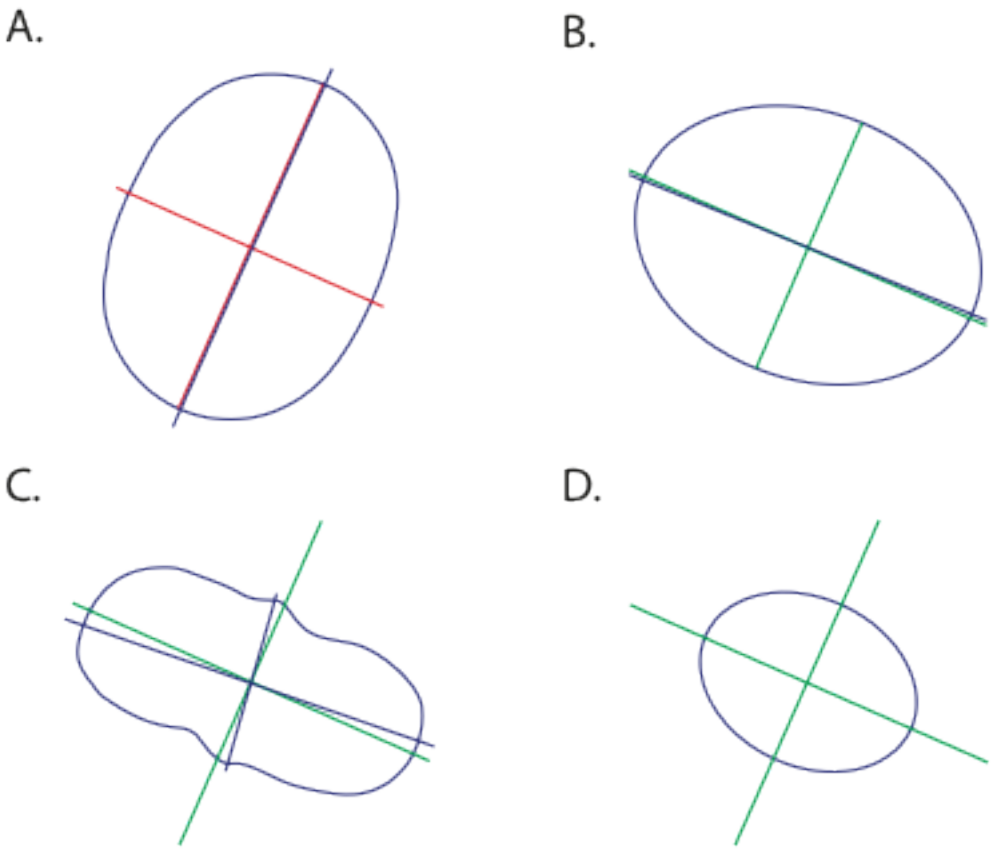

Figure C.3. Shape preferred orientation of Abo C1. See Figure 4.1 for location within core A) Rose of Intercepts. B) Rose of Traverses. C) Rose of Direction. D) Characteristic object. For all roses the ratio of the axis, R = 1.335 and the preferred angle of the grains is 113.72.

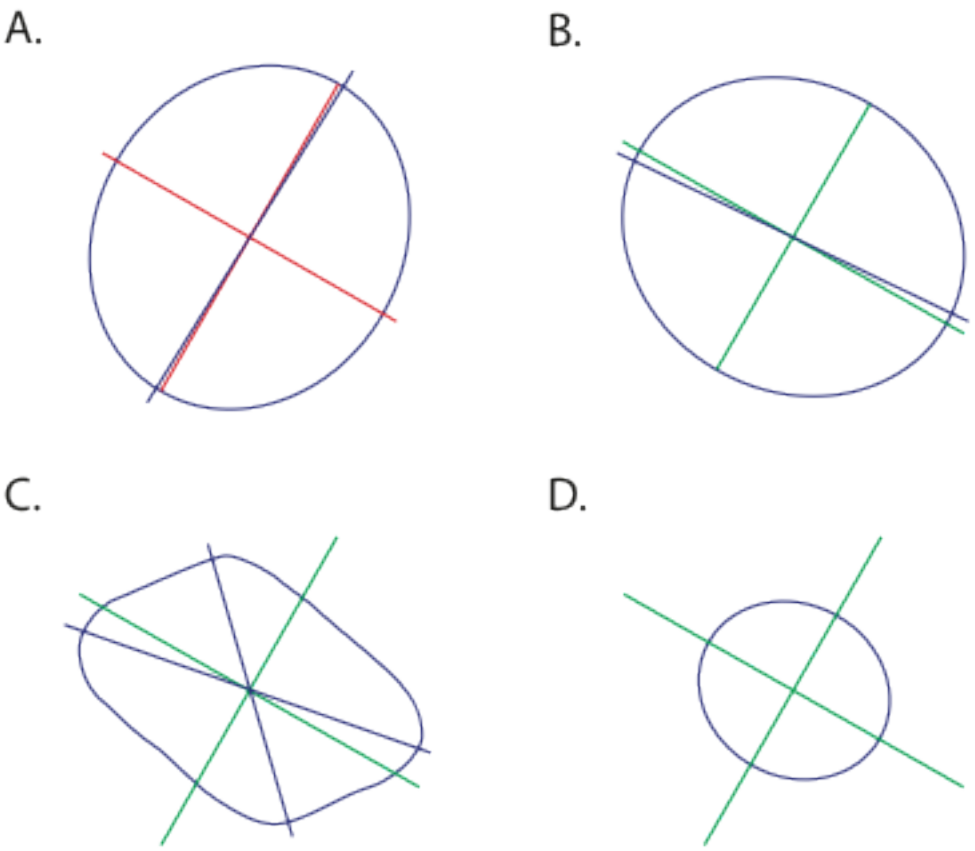

Figure C.4. Shape preferred orientation of Abo H1. See Figure 4.1 for location within core A) Rose of Intercepts. B) Rose of Traverses. C) Rose of Direction. D) Characteristic object. For all roses the ratio of the axis, R = 1.159 and the preferred angle of the grains is 119.98.

REFERENCES

Anders, M. H., & Wiltschko, D. V. (1994). Microfracturing, paleostress and the growth of faults. *Journal of Structural Geology, 16*(6), 795-815.

Atkinson, B. (1987). Introduction to fracture mechanics and its geophysical applications. In B. Atkinson (Ed.), *Fracture mechanics of rock* (1991st ed., pp. 1-23). San Diego, CA: Academic Press Inc.

Basson, I. J. (2004). Passive kimberlite intrusion into actively dilating dyke–fracture arrays: Evidence from fibrous calcite veins and extensional fracture cleavage. *Lithos, 76*(1-4), 283.

Berchenko, I., Detournay, E., & Chandler, N. (1997). Propagation of natural hydraulic fractures. *International Journal of Rock Mechanics and Mining Sciences, 34*(3-4), 63.e1-63.e11.

Billings, M. P. (1972). *Structural geology*. Englewood Cliffs, N.J.: Prentice-Hall.

Borg, I., Friedman, M., Handin, J., & Higgs, D. V. (1960). Experimental deformation of st. peter sand: A study of cataclastic flow. In D. Griggs, & J. Handin (Eds.), *Rock deformation* (pp. 133-192). New York: Geolgoical Society America Memoir.

Boutt, D. F., Goodwin, L., & McPherson, B. J. O. L. (2009). Role of permeability and storage in the initiation and propagation of natural hydraulic fractures. *Water Resources Research, 45*, W00C13.

Brock, W., & Engelder, T. (1977). Deformation associated with movement of Muddy Mountain overthrust in Buffington Window, Southeastern Nevada. *Geological Society of America Bulletin, 88*(11), 1667-1677.

Burger, H. (1976). Comparison of sieve and thin-section technique by a monte-carlo model. *Computers Geosciences, 2*(2), 123-139.

Cook, J. E. (2011). Systematic diagenetic changes in the grain-scale morphology and permeability of a quartz-cemented quartz arenite. *AAPG Bulletin, 95*(6), 1067.

Dalguer, L. A., K. Irikura, and J. D. Riera (2003). Simulation of tensile crack generation by three-dimensional dynamic shear rupture propagation during an earthquake, *Journal of Geophysical Research, 108*(B3), 2144.

Delaney, P., Pollard, D., Ziony, J., & Mckee, E. (1986). Field relations between dikes and joints – emplacement processes and paleostress analysis. *Journal of Geophysical Research, 91*(B5), 4920-4938.

Engelder, J. (1974). Cataclasis and generation of fault gouge. *Geological Society of America Bulletin, 85*(10), 1515-1522.

Engelder, & Lacazette, A. (1990). Natural hydraulic fracturing. In N. Barton, & O. Stephansson (Eds.), *Rock joints: Proceedings of the international symposium on rock joints* (pp. 35-43). Netherlands: A.A. Balkema, Rotterdam.

Faulkner, D. R., Mitchell, T. M., Healy, D. & Heap, M. J. (2006). Slip on 'weak' faults by the rotation of regional stress in the fracture damage zone. *Nature, 444*(7121), 922-925.

French, M. E., Boutt, D. F., & Goodwin, L. B. (2012). Sample dilation and fracture in response to high pore fluid pressure and strain rate in quartz-rich sandstone and siltstone. *J.Geophys.Res., 117*, B03215.

Friedman, M. (1969). Structural analysis of fractures in cores from saticoy field, ventura county california. *The American Association of Petroleum Geologists Bulletin, 53*(2), 367-389.

Ganne, P., & Vervort, A. (2007). Effect of stress path on pre-peak damage in rock induced by macro-compressive and-tensile stress fields. *International Journal of Fracture, 144*(2), 77.

Gundersen, E., Flekkoy, E. G., Bjorlykke, K., Feder, J., & Jamtveit, B. (2011). Fracture spacing during hydro-fracturing of cap-rocks. *Geofluids, 11*(3), 280-293.

Hadley, K. (1976). Comparison of calculated and observed crack densities and seismic velocity in Westerly granite. *Journal of Geophysical Research, 81*(20), 3484-3494.

Hoxha, D., & HOXHA. (2005). A microstructural study of natural and experimentally induced cracks in a granodiorite. *Tectonophysics, 395*(1-2), 99-112.

Janssen, C., Wagner, F., Zang, A., & Dresen, G. (2001). Fracture process zone in granite: A microstructural analysis. *International Journal of Earth Sciences, 90*(1), 46-59.

Johnson, M. R. (1994). Thin section grain size analysis revisited. *Sedimentology, 41*(5)

Katz, O., & Reches, Z. (2004). Microfracturing, damage, and failure of brittle granites. *Journal of Geophysical Research, 109*(B1)

Kelly, J., Fu, B., Kita, N., & Valley, J. (2007). Optically continuous silcrete quartz cements of the st. peter sandstone: High precision oxygen isotope analysis by ion microprobe. *Geochimica Et Cosmochimica Acta, 71*(15), 3812-3832.

Kranz, R. L. (1983). Microcracks in rocks - a review. *Tectonophysics, 100*(1-3), 449-480.

Launeau, P., Bouchez, J., & Benn K. (1990). Shape preferred orientation of object populations automatic analysis of digitized images. *Tectonophysics, 180*(2-4), 201-211.

Launeau, P., & Robin, P. (1996). Fabric analysis using the intercept method. *Tectonophysics, 267*(1-4), 91-119.

Lespinasse, M. (1999). Are fluid inclusion planes useful in structural geology? *Journal of Structural Geology, 21*(8-9), 1237.

L'Heureux, I., & Fowler, A. D. (2000). A simple model of flow patterns in overpressured sedimentary basins with heat transport and fracturing. *Journal of Geophysical Research, 105*(B10), 741-752.

McGrath, A., & Davison I. (1995). Damage zone geometry around fault tips. *Journal of Structural Geology, 17*(7), 1011-1024.

Menendez, B., Zhu, W., & Wong, T. (1996). Micromechanics of brittle faulting and cataclastic flow in berea sandstone. *Journal of Structural Geology, 18*(1), 1-16.

Moore, D., & Lockner, D. (1995). The role of microcracking in shear-fracture propagation in granite. *Journal of Structural Geology, 17*(1), 95-114.

Motoki, A., & Sichel, S. E. (2008). Hydraulic fracturing as a possible mechanism of dyke-sill transitions and horizontal discordant intrusions in trachytic tabular bodies of arraial do cabo, state of rio de janeiro, brazil. *Geofísica Internacional, 47*(1), 13-25.

Neuzil, C. E. (1995). Abnormal pressures as hydrodynamic phenomena. *American Journal of Science, 295*(6), 742.

Panozzo, R. (1987). Two-dimensional strain determination by the inverse surfor wheel. *Journal of Structural Geology, 9*(1), 115-119.

PANOZZO, R. (1983). Two-dimensional analysis of shape-frabric using projections of digitized lines in a plane. *Tectonophysics, 95*(3-4), 279-294.

Pitman, J. K. (1997). *Regional diagenetic patterns in the st. peter sandstone: Implications for brine migration in the illinois basin*

Pollard, D., & Aydin, A. (1988). Progress in understanding jointing over the past century. *Geological Society of America Bulletin, 100*(8), 1181-1204.

Rawling, G., Baud, P., & Wong, T. (2002). Dilatancy, brittle strength, and anisotropy of foliated rocks: Experimental deformation and micromechanical modeling. *Journal of Geophysical Research, 107*(B10)

Reches, Z., & Lockner, D. (1994). Nucleation and growth of faults in brittle rocks. *Journal of Geophysical Research, 99*(B9), 18159-18173.

Rigopoulos, I., Tsikouras, B., Pomonis, P., & Hatzipanagiotou, K. (2011). Microcracks in ultrabasic rocks under uniaxial compressive stress. *Engineering Geology, 117*(1-2), 104-113.

Scholz, C., Dawers, N., YU, J., & Anders, M. (1993). Fault growth and fault scaling always: preliminary results. *Journal of Geophysical Research, 98*(B12), 21951-21961.

Secor, D. T. (1965). Role of fluid pressure in jointing. *American Journal of Science, 263*(8), 633.

Sibson, R. H. (1992). Implications of fault-valve behavior for rupture nucleation and recurrence. *Techtonophysics,* 211(1-4), 283-293.

Simmons, G., & and Richter, D. (1976). Microcracks in rock. In R. G. J. Strens (Ed.), *The physics and chemistry of minerals and rocks* (pp. 105-137). New York, NY: Wiley.

Takemura, T., & Oda, M. (2004). Stereology-based fabric analysis of microcracks in damaged granite. *Tectonophysics, 387*(1-4), 131-150.

Tapponnier, P., & Brace, W. (1976). Development of stress-induced microcracks in westerly granite. *International Journal of Rock Mechanics and Mining Sciences Geomechanics Abstracts, 13*(4), 103-112.

Vermilye, J., & Scholz, C. (1998). The process zone: A microstructural view of fault growth. *Journal of Geophysical Research, 103*(B6), 12223-12237.

Wang, H. (2000). *Theory of linear poroelasticity with applications to geomechanics and hydrogeology*. Princeton, N.J.: Princeton University Press.

Wilson, J. E., Chester, J. S., & Chester, F. M. (2003). Microfracture analysis of fault growth and wear processes, punchbowl fault, san andreas system, california. *Journal of Structural Geology, 25*(11), 1855-1873.